UNIVERSIDAD NACIONAL AUTÓNOMA DE MÉXICO
Doctorado en Ciencia e Ingeniería de Materiales
Instituto de Investigaciones en Materiales

One-dimensional ZnO nanostructures for photocatalytic and sensing applications

Tesis
QUE PARA OPTAR POR EL GRADO DE:
Doctor en Ciencia e Ingeniería de Materiales

PRESENTA:
Andrés Galdámez Martínez

Dr. Ateet Dutt
Instituto de Investigaciones en Materiales (IIM-UNAM)

Dr. Guillermo Santana Rodríguez
Instituto de Investigaciones en Materiales (IIM-UNAM)

Dra. Citlali Sánchez Aké
Instituto de Ciencias Aplicadas y Tecnología (ICAT-UNAM)

Ciudad Universitaria, CDMX, agosto 2023

UNIVERSIDAD NACIONAL AUTÓNOMA
DE MÉXICO

Posgrado en Ciencia e Ingeniería de Materiales
Instituto de Investigaciones en Materiales

One-dimensional ZnO nanostructures for photocatalytic and sensing applications

Thesis

Prepared for the Degree of:

Ph.D. in Materials Science and Engineering

PRESENTS:

M.C.I.M. ANDRÉS GALDÁMEZ MARTÍNEZ

ADVISORY COMMITTEE
Ph.D. Ateet Dutt
Instituto de Investigaciones en Materiales (IIM-UNAM)
Ph. D. Guillermo Santana Rodríguez
Instituto de Investigaciones en Materiales (IIM-UNAM)
Ph. D. Citlali Sánchez Aké
Instituto de Ciencias Aplicadas y Tecnología (ICAT-UNAM)

Ciudad Universitaria, CDMX, agosto 2023

Para Erika

Content

Acknowledgments

People who have been close to me over the last 4 years have surely noticed the hair loss and weight gain, the persistent dark circles under my eyes, the rush and anxiety that surround me. No project of mine has been as absorbing as my doctoral studies. With all this it is clear to me that I would have collapsed somewhere along the way had it not been for the many people who have been by my side supporting me and to whom I wish to say a big thank you.

First, to my wife Erika who more than anyone else was by my side throughout this project. Those long hours of work would have been unbearable without having you around to remind me that we are human before academics. In addition, your observations, comments, and suggestions regarding my work have always provided the enriching perspective that nurtures a large part of these results.

As always, my excellent tutors (Ateet Dutt, Guillermo Santana, and Citlali Sanchez) worked very hard reviewing and improving my manuscripts, presentations, proposals, and experimental procedures. Ateet, especially, taught me the team building, communication and proactivity skills needed to develop multidisciplinary research.

Thanks also to the technical staff of characterization teams, students, and researchers in charge of laboratories in which I perform experimental procedures. Its members are academics from universities and institutes such as UNAM, UAEH, IPN, CIBA, BUAP, UTec Tulancingo, University of Strathclyde, Universitat de Barcelona, University of Liverpool. In no particular order are: Marisol Gonzales, Carlos Ramos, Lourdes Bazán, Omar Novelo, Yang Bai, Sebastian Sprick, Frank Güell, Selene Islas, Abdu Orduña, Claudia Garduño, Manmohan Jain, Antonio Méndez, Osvaldo de Melo, Amauri Serrano, Karina Portillo, Francisco Malagón, Rafael Salinas, Shirley Tolibia, Lazaro Huerta, Adriana Tejeda, Airam Brito, Josué Romero, Agileo Hernández.

Diana Arias, Esther Carrillo, Isabel Gómez and Luisa Reséndiz always made an incredible effort to keep us students up to date with our paperwork and to help us take advantage of the support programs. Thanks to all of them.

Finally, special thanks to the Consejo Nacional de Humanidades Ciencias y Tecnologías (CONAHCYT) for the doctoral grant CVU 860916. Thankfully acknowledge to PAPIIT projects IA101321 and IA100123 for funding this research project.

Abstract

In the present work, one-dimensional zinc oxide nanostructures (1DZnO) were obtained using pressure-modulated metal-assisted vapor transport. Using electron and X-ray diffraction, scanning/transmission electron and atomic force microscopies, UV-visible, photoluminescence, X-ray photoelectron, and Fourier Transformed Infrared spectroscopies, the morphological, structural, and optical properties of the system were determined. The reported methodology allowed control over the orientation, length, diameter, and distribution in the catalyst-assisted growth of high-crystalline 1DZnO nanostructures with tailored optoelectronic characteristics. The control over the nanostructured coatings was achieved through operation parameters such as transport gas flow/composition, precursors, substrate employed, catalyst pattern, and temperature.

After the synthesis understanding of these materials, different 1DZnO morphologies were evaluated as photocatalysts for hydrogen production through the water-splitting reaction. It was discovered that 1DZnO with random orientation, high aspect ratio, and ideal diameter distribution exhibit the most stable and effective photocatalytic activity.

Furthermore, CO_2 gas chemo-resistive sensing properties at different concentrations were investigated for the 1DZnO materials synthesized. The results showed a high sensing response for longer 1D nanostructures and faster response time for shorter ones. Good selectivity was also found towards the oxidizing gas. These two applications could then contribute towards the green transition agenda.

Lastly, by evaluating the impact of the morphological and structural factors concerning 1DZnO biofunctionalization methodologies, an appropriate antibody attachment procedure was developed to construct an *E. coli* optical biosensing layer. The results showed an excellent approach to developing efficient biorecognition layers on top of 1DZnO materials without hindering the optical response.

Introduction

In recent years, climate change, energy demand, and health have been regarded as among the most urgent global issues to be resolved[1]. Numerous studies have been conducted concerning these issues in search of alternatives and solutions. Due to their morphological and optoelectronic properties, semiconductor metal oxides are promising candidates for various applications, including environmental remediation, photocatalytic hydrogen production, carbon dioxide detection and capture, and platforms for developing nanostructured biosensors due to their morphological and optoelectronic properties[2,3].

Since its discovery, photocatalytic hydrogen production has been regarded as one of the potential answers to environmental and energy production challenges[4]. ZnO stands out as one of the most utilized semiconductors for photocatalysis. Its band structure satisfies the parameters for photocatalytic hydrogen production under appropriate light irradiation. Moreover, its non-toxicity, biocompatibility, low production cost, and effective charge transport make it a top contender for the photocatalytic water splitting reaction[5].

However, the magnitude of its band gap (3.37 eV) imposes a limitation for photocatalytic activity under visible illumination. This is because it can only use 4% of the solar radiation (near UV region) in photoexcitation processes. Some works have sought to improve efficiency in the visible region by employing strategies such as control over the morphology of the photocatalyst, particle size, heterostructure formation, and noble metal deposition, among others.

Recently, ZnO nanostructures have received significant interest in photocatalysis due to the diversity of nanostructures obtainable and their properties[6]. Nanostructured ZnO can exist in different morphologies, such as nanotubes, nanowires, nanosheets, nanobelts, and nanoflowers, which offer different properties from those of bulk ZnO[7]. Due to high aspect ratios, large surface areas, and structural confinement in radial dimensions, 1D nanostructures have been shown to have favorable mechanical, electrical, optical, and chemical properties in the photocatalytic performance of the system. Consequently, 1D ZnO-based nanomaterials have been successfully used for the photocatalytic production of hydrogen[8].

Advances in ZnO nanostructure growth technology have also been helpful for the development of sensing platforms. ZnO coatings have demonstrated changes in their conductivity due to gas adsorption, making them ideal materials for developing gas-resistive sensors. In addition, the possibility of obtaining ZnO nanostructure platforms with versatile morphologies and surface properties is fundamental to developing technologies for detecting polluting gases that affect human health and environmental integrity. Thus, developing CO_2 sensors is necessary for the green transition framework.

The ZnO nanostructuring process has also proven attractive for developing biosensor devices[9]. Biosensors are selective and sensitive devices for detecting chemical and biological substances at deficient concentrations. Furthermore, they offer the possibility of real-time analysis without the need for sample pretreatment or large sample volumes[10]. As medical diagnostics require

accurate, fast, and inexpensive biosensors, the inherent advantages of optical detection methods (i.e. label-free, no crosslinkers) must be evaluated. The surface and optical properties of 1DZnO offer benefits for the effective immobilization of bioselective layers to various analytes of interest. Moreover, the need to use 1D transducers as active elements in sensors derives from the need to achieve increasingly lower thresholds in detection levels. The significant advantage of using these structures is the increased sensitivity of the devices due to the high surface-to-volume ratio[11]. In addition, surface plasmon resonance phenomena and characteristic photoluminescence make these optical systems promising candidates in optical biosensing[12].

In this work, the synthesis and characterization of one-dimensional ZnO nanostructures were carried out. Subsequently, the performance of the obtained materials in photocatalytic hydrogen production, CO_2 sensing, and as an optical biosensing layer for *Escherichia coli* was evaluated.

Chapter I. Theoretical framework

One-dimensional ZnO nanostructures

ZnO is a binary semiconductor whose use in its polycrystalline form (Figure 1-1 (a)) is widespread in industrial applications, as well as in everyday commercial goods. Thus, the compound is employed in cosmetic products, sunscreens, catalysts, lubricant additives, paint pigmentation, piezoelectric transducers, and bactericidal agent, among others (Figure 1-1(b))[13,14]. This extensive range of applications is a consequence of the n-type semiconductor's electrical character as well as chemical, optical, photocatalytic, and biocompatible capabilities.

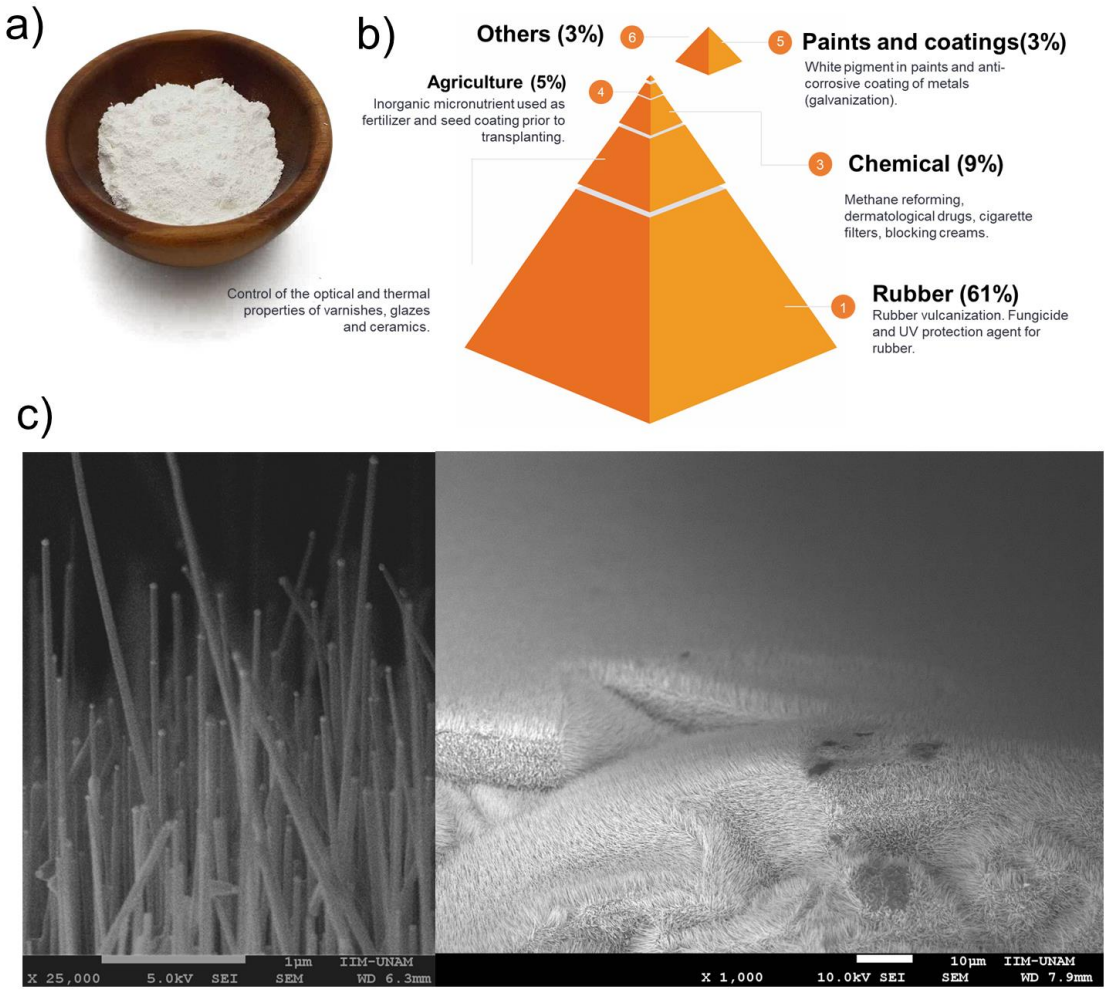

Figure 1-1. (a) Zinc oxide powder (ZnO). (b) Commercial and industrial uses of ZnO in its polycrystalline phase[14]. (c) One-dimensional ZnO nanostructured coating on crystalline substrates obtained in the MAVER-IIM/UNAM laboratory.

ZnO is an attractive material for the fabrication of optoelectronic devices due to its direct gap of 3.37 eV, its excitonic energy at room temperature (60 meV), and its structural resemblance with GaN. It also presents a laser emission in the ultraviolet and adequate transmittance in the UV-Visible spectrum to function as a photosensor material. At ambient pressure and temperature conditions, the material possesses a hexagonal wurtzite structure in which each Zn^{2+} ion is tetrahedrally coordinated with four O^{2-} ions and viceversa (i.e., each oxygen ion

coordinated with four zinc ions). The ideal cell (P63mc, C_{6v}^4) shows a c/a ratio of 1.6. However, structure modifications (i.e., doping, defects) turn the X-Ray diffraction (XRD) experimental results of *c/a* to an interval between 1.593-1.604[15]. The interpenetration of Zn^{2+} and O^{2-} tetrahedrons derives from the sp^3 orbital hybridization and produces the alternate between oxygen and zinc planes of atoms. This coordination is evidence of the polar character in the Zn-O bond. However, the electronegativity difference between Zn and O also suggests an essential ionic contribution to the interaction[16,17]. This results in the polarization of the hexagonal structure along its *c*-axis. The mentioned charge alternate also produces contrary charged planes in the *c* direction as well as positive (001) Zn plane and negatively charged (00$\bar{1}$) O plane. Nonpolar facets occur when a plane is composed of the same number of negative and positive ions. The most common are the *a*-orientated (100) and (110) planes[18]. The relative contribution of the polarity characters in different crystal facets is responsible for phenomena such as anisotropic crystalline growth, defect generation, and functionalization.

Additionally, its biocompatibility allows using ZnO in biological (biosensing, antimicrobial/antivirus, bioimaging) and environmental (photocatalysis, pollution monitoring) applications. The motivation to substitute widely used optical semiconductors (e.g., GaN, CdS) with less contaminating compounds is also relevant, as these materials offer an easier non-toxic recycling option.

Furthermore, recent improvements in the synthesis technology of ZnO-based nanostructures[19,20] have also led to a renewed interest in implementing these materials in diverse research areas. For this reason, a great effort has been made to produce high-quality, low-dimensional ZnO materials. Morphologies such as nanoparticles (NPs), nanowires (NWs), nanorods (NRs), nanoflowers, tetrapods, and thin films, which offer an enhanced surface-to-volume ratio and physicochemical properties are among the most studied nanostructured ZnO platforms. This extensive collection of nanostructured ZnO-based materials encourages their application in modern nanodevices. A relevant group of ZnO nanostructured materials comprises NWs and NRs, often referred to as one-dimensional ZnO nanomaterials (1DZnO). As can be seen in Figure 1-1 (c), the 1DZnO is highly anisotropic in its structure because of a preferential growth direction.

Generally, the one-dimensional structures must have a transversal section (i.e., diameter: d) much shorter than its axial length (l). The aspect ratio determines the $l\ d^{-1}$ morphological proportion of the nanostructure. In such 1DZnO coatings, precise control over the nanostructures' orientation, dispersion, composition, and size must be achieved to implement them in optoelectronic applications. Properties such as efficient charge transport, high crystalline quality, and band gap modulation have been studied in areas including sensing, photocatalysis, and biotherapy[21]. In the last 20 years, more than 33,000 "one-dimensional ZnO nanostructure" articles have been published in indexed journals[22].

Vapor phase growth technique of 1DZnO materials

There are a variety of techniques available for obtaining 1DZnO materials. These can be categorized into vapor phase growth, solution nucleation, and templated

approaches. These vapor phase growth techniques are an example of a bottom-up strategy that allows obtaining nanostructured coatings of high crystallinity and homogeneity on crystalline substrates[23,24].

To achieve preferential nucleation of the gaseous precursors, it is common to use a substrate prepared with a suitable catalyst or with a nuclei-textured surface, as shown in Figure 1-2. Depending on the phase in which the catalyst is present during the nucleation of the 1D structure, the assisted growth mechanism is called VLS (liquid catalyst) or VSS (solid catalyst)[25].

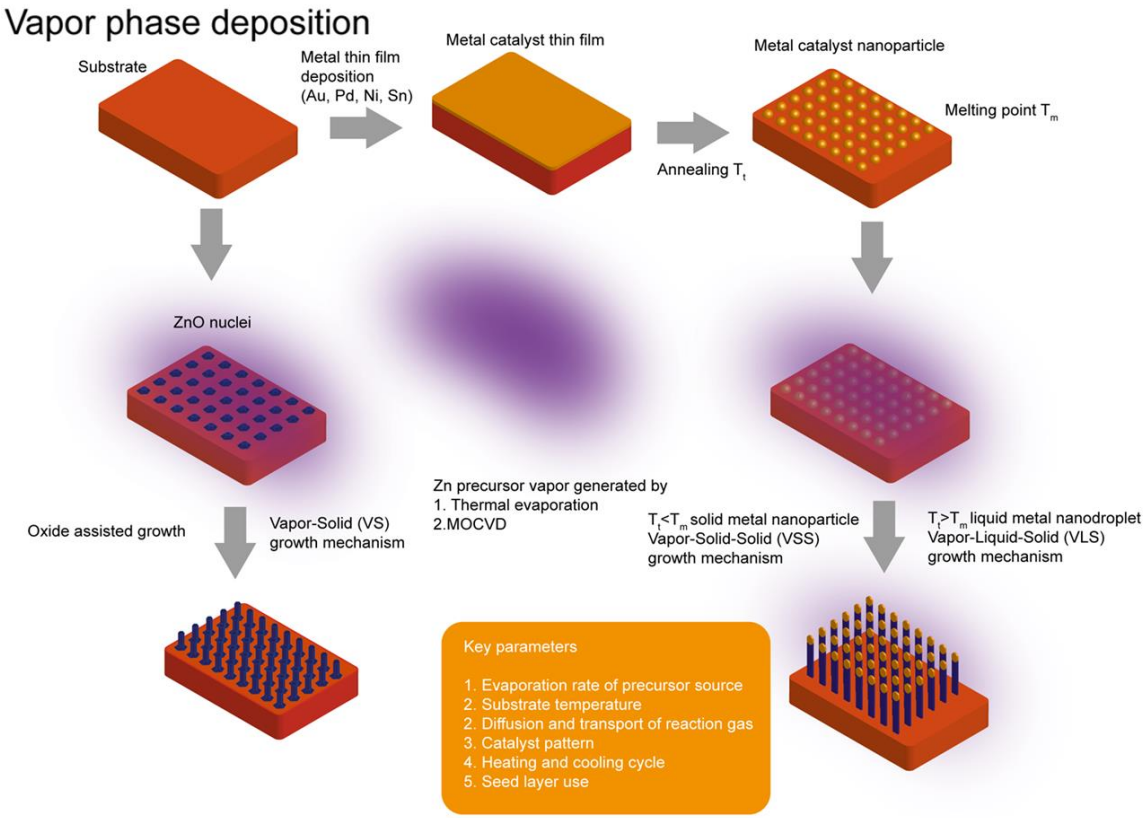

Figure 1-2. Vapor phase growth mechanisms. The supply of precursor gas species to a liquid (VLS) or solid (VSS) catalyzed surface phase is observed. In this way, it is possible to achieve the growth of ZnO nanostructures with axial confinement[26].

The growth process begins with the thermal evaporation of a ZnO precursor to produce Zn (g) vapor. Since the evaporation point of the compound is considerably high, using ZnO:C mixtures instead of pristine ZnO powder has been reported, as the resulting carbothermal reaction can produce zinc vapor at lower temperatures (750°C)[27]. Subsequently, the gaseous reactants are brought to the surface of a liquid-phase catalyst nanoparticle (e.g., Au, Sn, Cu) using a carrier gas. There the diffusion process of soluble precursor atoms takes place. This process continues until a supersaturated condition is reached. Finally, at the substrate-catalyst interface, the Zn precursor is oxidized to form a solid ZnO crystalline structure that results in anisotropic growth of the 1D material as far as the precursor species continue to be supplied or the temperature in the synthesis chamber is reduced (Figure 4-2). This methodology has been used to obtain one-dimensional metal oxides since it was reported by Wagner and Ellis[28].

As simple as it may seem, there are many questions about the precise mechanism that the system follows under certain growth conditions[29].

Understanding the details of the mechanism of catalyst-assisted vapor-phase growth of semiconductor nanostructures is an important area of research to gain control over the morphological properties of the coatings[29–32]. Among the key working parameters are the temperatures of both the substrate and the evaporation source, the pressure of the synthesis chamber, the processes of generation and transport of the gaseous species, the shape and size of the metal catalyst, as well as the crystalline structure of the substrate on which the 1DZnO[32] are obtained.

In addition, the exchange between precursor source gases during growth allows the formation of radial and axial heterostructures. Platforms composed of highly vertically aligned 1DZnO layers have been obtained by taking advantage of the epitaxial growth between the ZnO lattice and the support employed. Thus, highly aligned 1DZnO structures have been obtained on sapphire, GaN, AlGaN, and AlN substrates[33,34].

As already mentioned, the phase difference of the seeded or catalyzed surface defines the growth rate of the nanostructures since the adsorption rate of the gaseous precursor species on solid surfaces is lower compared to liquid ones[35]. Therefore, using metal catalysts reduces the formation energy of 1D nanostructured ZnO and allows precise control over the dimensions and arrangement of the nanostructures. Au NPs is a popular metal catalyst for producing ZnO NWs and NRs[31]. This is due not only to the good solubility of the Zn precursors in Au solution but also to the surface tension of the metal that allows catalytic droplets with high contact angles, advantageous for optimal growth of 1DZnO.

On the other hand, the role of a buffer film between the substrate and the nanostructured ZnO system has also been investigated primarily in cases with high structural incompatibility between the two components (cubic substrates). This film, also called the seed layer, provides the basis for nucleation to produce ZnO growth and controls the alignment of the structures. It has been reported that obtaining 1DZnO materials with controlled dimensions and high aspect ratios on Si substrates requires the use of a ZnO seed layer to reduce the mismatch between the crystal lattice of the substrate and the growing nanostructure[36,37].

Chapter II. Applications

Improving fundamental aspects of daily life, such as health, energy availability, and environmental care, requires developing and implementing new technologies. Integrating cheap, abundant, innocuous semiconducting materials into practical devices is necessary to contribute to the former challenges. Although many semiconductors display outstanding optical, electrical, or magnetic properties, they often lack three necessary characteristics. In other words, they are expensive, scarce, or have high toxicity levels. Thereon, nano ZnO-based materials with inherent properties and advantages have prompted its application in multiple areas including photocatalysis, detection, and gas sensing.

Photocatalytic hydrogen production

Currently, environmental remediation, which includes wastewater treatment (e.g., dyes, pesticides, detergents), CO_2 reduction, and the solar-driven production of energy vectors[38–41], is a response to rising energy demand, industrialization, and modern consumer habits (Figure 2-1 (a)). In pursuit of these goals, heterogeneous photocatalysis is recognized as one of the most promising candidates. The photocatalytic process is broadly defined as accelerating a chemical reaction in the presence of a semiconductor (photocatalyst) and light without the photocatalyst directly participating in the chemical reaction. It begins with the generation of electron-hole pairs through the absorption of photons with energies greater than the semiconductor's bandgap. After the generation of charge carriers, these can either recombine (resulting in the loss of energy as heat or light) or participate in charge transfer processes (oxidation/reduction) with molecules adsorbed on the semiconductor. Both redox reactions can occur within the surface: the reduction of electron acceptor species when the reduction potential is less than the energy of the CB (conduction band) and the oxidation of electron donor species when the potential is greater than the energy of the VB (valence band). In aqueous media, these redox reactions can also form radical (e.g., $^{\circ}OH$, $^{\circ}O_2^-$) and ionic (e.g., OH^-, HO_2^-) species that are highly effective in the degradation of polluting compounds and microbial agents in water cleaning applications[42–45].

Since Honda and Fujishima discovered photocatalytic hydrogen production in 1972[46], it has been regarded as a desirable alternative for generating the carbon-free energy vector. Indeed, this would contribute to addressing the current environmental crises associated with fossil fuel consumption[4] (Figure 2-1 (b)).

In recent years, multiple semiconductors have been tested in the photocatalytic hydrogen evolution reaction (HER), including TiO_2, CdS, CuS, and Fe_2O_3, which sometimes exhibit higher photocatalytic activity than ZnO itself. However, new and simple methodologies to obtain ZnO nanostructures with enhanced optical and electric features, a large surface area to volume ratio, low cost, and scalability for mass production greatly encourage its continual development[47,48].

Due to their ease of crystallization, anisotropic growth, electron mobility (200-1000 $cm^2V^{-1}s^{-1}$), and chemical tunability[5], 1DZnO have been used in photocatalytic HER.

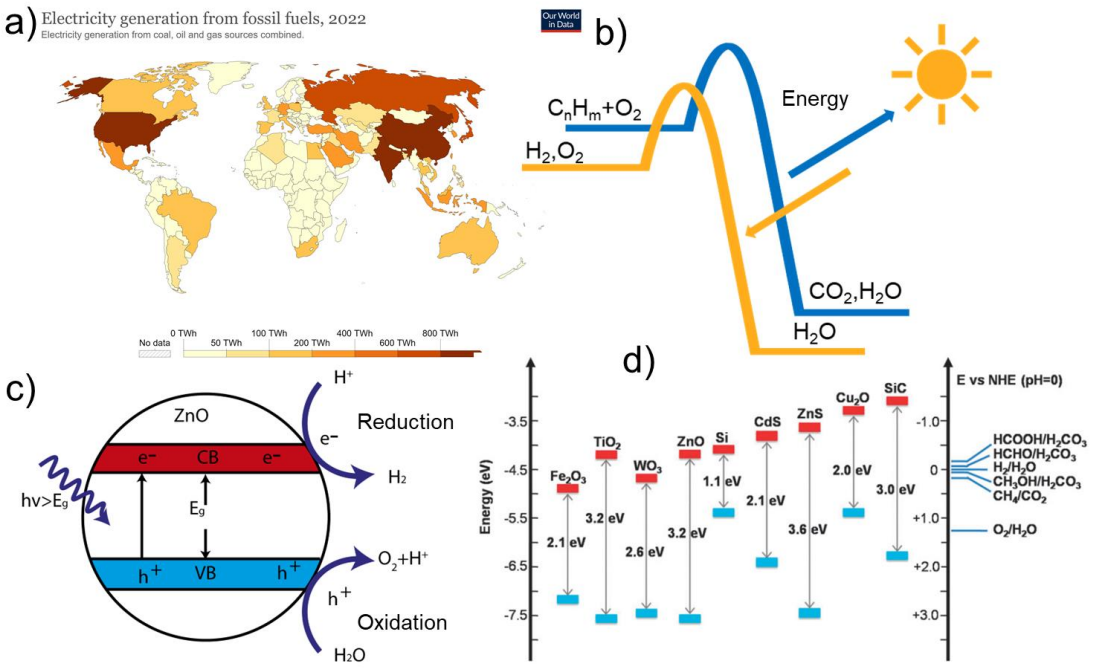

Figure 2-1. (a) Map showing global energy dependence on fossil fuels[49]. (b) Diagram showing energy generation processes from hydrocarbon combustion (blue) and for the generation of carbon-free energy carriers such as hydrogen (yellow). (c) Photocatalytic hydrogen production mechanism using ZnO as photocatalyst. (d) Band edge positions of some semiconductors in relation to the energy levels of various redox reactions[50].

The semiconductor requires a band gap of at least 1.23 eV in a 0-pH solution and illumination of 1008 nm to produce the photocatalytic generation of hydrogen via water splitting. H^+ ions are the electron-accepting species in photocatalytic hydrolysis, while OH^- hydroxyl ions are the donor species (Figure 2-1 (c)). Therefore, the positions of the ZnO valence band (VB = +2.7 V) and conduction band (CB = -0.33 V) relative to the standard hydrogen electrode (NHE) are suitable for the photocatalytic production of hydrogen through the water splitting reaction (Figure 2-1 (d)). The photocatalytic procedure is defined by the reactions listed below:

$$\text{Photoexcitation: } ZnO + 2\ h\nu \rightarrow 2\ e^- + 2\ h^+$$
$$\text{Oxidation: } H_2O + 2\ h^+ \rightarrow 1/2\ O_2 + 2\ H^+$$
$$\text{Reduction: } 2\ H^+ + 2\ e^- \rightarrow H_2$$
$$\text{Net reaction: } H_2O + 2\ e^- + 2\ h^+ \rightarrow H_2 + 1/2\ O_2$$

The photoexcitation reaction on ZnO generates a charge carrier pair, consisting of an electron (e^-) and a hole (h^+). The photogenerated holes then oxidize water, resulting in the production of protons and molecular oxygen. Simultaneously, the electrons initiate a reduction reaction of the protons, leading to the generation of molecular hydrogen. Consequently, in the presence of a photocatalyst, the net reaction produces both hydrogen and molecular oxygen from water. The primary photocatalytic limitations of ZnO are its high electron-hole recombination rates,

low visible light absorption (3-4% of the solar spectrum), and photostability[51]. Therefore, numerous strategies have been implemented to improve the photocatalytic performance of ZnO nanostructures in the visible spectrum[52].

Semiconductor coupling (heterojunctions), non-metal/metal doping, sensitization with organic materials, and noble metal deposition stand out among the most frequently reported approaches[53–57]. These former strategies will have mainly the following effects: modifying the band gap, shifting the absorption range towards the visible, and trapping charge carriers. Yet, these approaches frequently result in the emergence of new obstacles to overcome, as undesirable side effects such as the formation of trap states, interface imperfections, and electronic retro injection to the sensitizer dye tend to emerge. Thus, reducing carrier mobility and negatively impacting the photocatalytic performance of the system. In this regard, the specific built-in potential gradient of axially confined ZnO nanomaterials for enhanced exciton separation is currently being studied[58]. It has been reported that rapid electron transport along the structure's central axis improves the charge carrier collection time. Contrarily, a scattering effect is observed at the grain boundaries of polycrystalline films, which drastically reduces the device's performance. So, monocrystalline 1DZnO structures are desired as they contain few electron trapping sites[8]. Also, the Fermi level introduction by metallization of the semiconductor, which is typically lower in energy than the conduction band of a semiconductor, has been identified as one of the possible approaches to enhance charge separation. This method allows electrons to move toward the noble metal while holes can remain in the valence band[59]. This mechanism can cooperate with the surface plasmon resonance effect to produce plasmonic photocatalysis[55,60,61]. Consequently, the practical implementation of Au and Ag NPs in materials such as TiO_2[62] and MoS_2[63] has been associated with an increase in HER.

For this reason, ZnO-based nanostructures offer a non-toxic, sustainable, and cost-effective alternative to produce hydrogen via photocatalytic mechanisms as the development and search for tailored catalytic materials continue.

CO_2 gas sensing

Currently, the deployment of gas sensor technology is crucial for achieving a fully sustainable society, environmental protection, and the assurance of well-being[64]. For instance, numerous studies have emphasized the impact of various air pollutants on human health and the ecosystem, including H_2S, NO_x, O_3, CO, and certain volatile organic compounds[65,66]. Among the noxious species, CO_2 is one of the most significant worries. For this reason, the availability and development of novel platforms for its efficient and selective detection are crucial to maintaining quality living conditions. CO_2 gas sensing technology could also benefit the biomedical, agriculture, shipping, mining, and food packaging industries. Microelectronic gas sensor systems were created in the past, but their limitations prohibit them from archiving sensitivities in the range of sub-ppm concentrations. For this reason, transducing materials within the nanoscale are employed to detect analytes with high sensitivity[67,68].

Multiple metal oxide nanostructures (e.g., TiO_2, WO_3, and SnO_2) have been utilized to detect CO_2[69]. Nonetheless, ZnO stands out due to its absorption and electrical characteristics, which result in an effective surface transduction response to the target gas contact[70]. In 1962, a ZnO thin film became the first material reported to modify its resistivity owing to the contact with a gaseous phase (Figure 2-2 (a-b))[71]. ZnO is a viable material for using as a gas-sensing layer due to its mass-scalable production methods and high sensitivity, which is equivalent to the performance of commercially available materials. ZnO is the second-most-researched metal oxide semiconductor used as a resistive gas sensor.

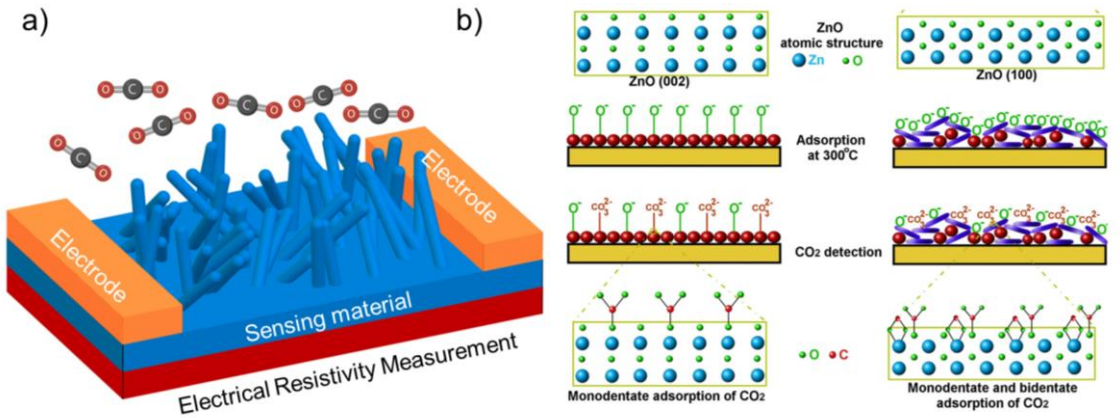

Figure 2-2. (a) Chemiresistive gas sensor material where conductivity response to gas adsorption is observed. (b) Mechanism of CO_2 molecule sensing on ZnO surface[72].

In addition, nanostructured ZnO significantly increases the system's surface area, enhancing the material's adsorption properties. When included as recognizing elements in gas sensing devices, 1DZnO nanostructures exhibit low detection limits, sensitive and quick response, and good recovery times[73–81]. This derives from the high electron mobility along the structure's radial axis and the adjustable sensitivity produced via surface engineering of the nanostructure (i.e., surface defects and functionalization)[81–84]. Therefore, research into the sensing ability of 1DZnO materials towards CO_2 is still not near to being exhausted but remains to be examined in depth. Currently, low defect density, high electron mobility, high surface-to-volume ratio, porosity, and crystallinity are among the significant characteristics impacting the chemoresistance of ZnO-based detectors.

Optical-based immunosensors

The COVID-19 pandemic has demonstrated that many present biotechnologies must continue to advance to combat this and future health crises[85]. Thus, the development of ergonomic, accurate, and user-friendly sensing devices for the quick detection of numerous biological analytes and infectious agents (e.g., nucleic acids, cells, enzymes, proteins, virus and bacteria) is one of the main objectives[9,86]. Even though standard techniques (biochemical and molecular methods) are used to detect pathogens and expensive equipment/reactives, the need for qualified personnel and processing times could become a constraint when the demand for identification increases rapidly. In this context, biosensors are sensitive and selective instruments for the identification of extremely low quantities of biological analytes. A biosensing platform contains a layer of

transducing material that transforms the chemical or physical interaction between the analyte and the sensing layer of the system. Following the nature of the transducer response, sensing devices can be categorized as acoustic, piezoelectric, electrochemical optical, and photoelectrochemical (Figure 2-3 (a-b))[87–98].

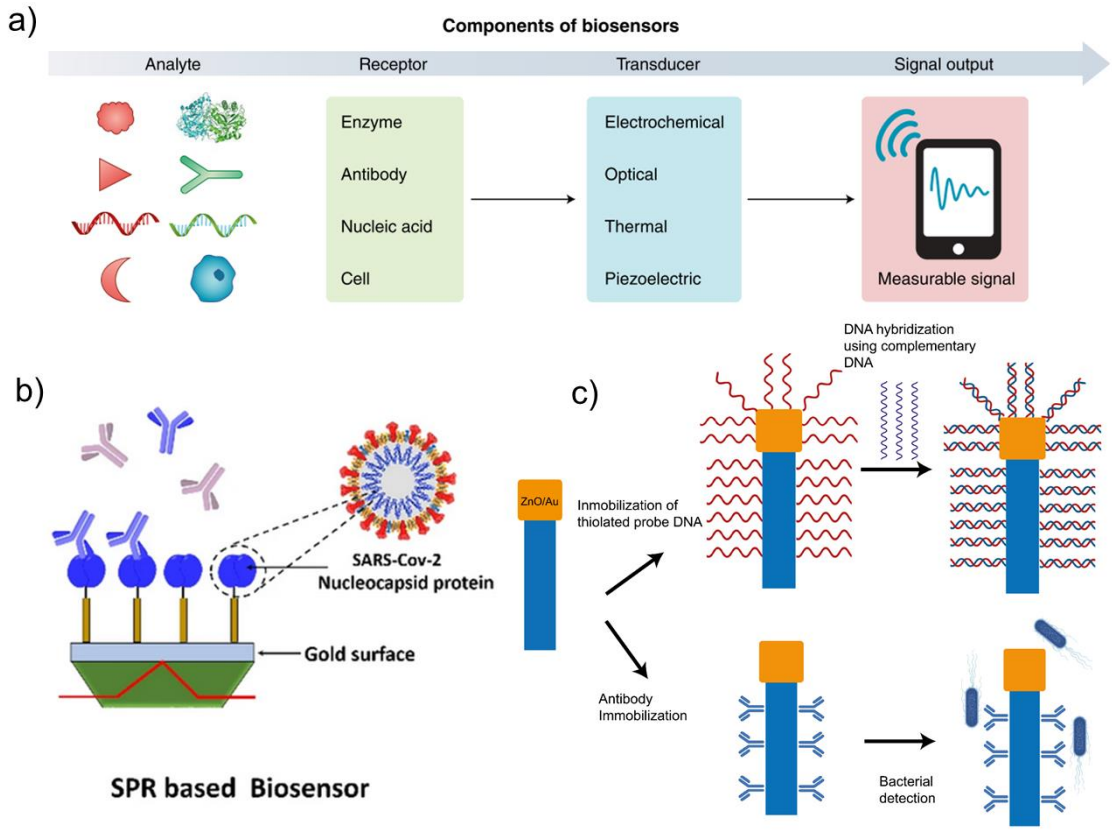

Figure 2-3 (a) Elements that make up a biosensing system: biological analyte of interest, bio-selective element, transducer platform, signal processing system[99]. (b) Plasmonic response optical biosensor for the detection of SARS-CoV-2 virus[100]. (c) 1DZnO platforms for the immobilization of various biosensing agents.

Consequently, the development of more effective biosensing devices with enhanced detection mechanisms are viable options that directly contribute to the identification of present and emerging diseases in the medical, food, water, and environmental sectors. Emerging biosensor devices have a positive outlook for industrial and large-scale processing with acceptable error margins[101–105], so their development has become the subject of intensive study. In addition, advancements in the growing processes of nanostructures have marked a turning point in the evolution of biosensing systems. The ability to generate nanostructured materials with diverse morphological characteristics, adaptable physicochemical properties, and high surface-to-volume ratios is vital for achieving an efficient interaction with various biological analytes. The unique properties of 1DZnO nanostructured materials make them ideal candidates for biosensing applications. For example, the non-center-symmetric structure of ZnO makes it possible to create a vast array of nano-morphologies from this material. Thus, it has been reported that 1DZnO nano-matrices comprised of nanowires and nanorods may be used to produce selective and sensitive biosensors[9,106,107].

All these morphologies offer enhanced biosensing efficacy because of their increased surface area compared to their bulk counterparts. In addition, its high isoelectric point (9.5) enables the attachment of biomolecules to its surface as well as the selective capture of analytes with a low isoelectric point. Their optical sensitivity, piezoelectricity, low cost, and nontoxicity with the human body have enabled their usage in biosensing platforms with lower detection thresholds.

The existence of surface plasmon resonance features and distinctive photoluminescence in 1DZnO metal composites, for instance, has made these systems suitable for optical biosensing[12]. Yet, 1DZnO characteristics like orientation, size, structure, density, and chemical surface modification must be studied to develop efficient immobilization procedures for various biorecognition components (Figure 2-3(c)). Diverse methods exist to produce efficient biosensor devices. Consequently, the manufacturing process may be optimized on several levels. Numerous studies have attempted to boost the sensitivity of biosensors by the site direction of antibodies and/or the application of labels in the case of immunosensors[108]. Other methods look for binding matrices suitable with very sensitive signal responses (e.g., noble metal electrodes)[109,110]. The use of silane as a coupling agent has shown to be a repeatable and generally recognized strategy for producing sensor surfaces[107,111,112]. Most functionalization strategies for ZnO platforms include silane treatments using APTES (3-aminopropyltriethoxysilane) and APTMS (among others) 3-aminopropyltrimetoxysilane)[111,113,114]. These apply to various ZnO nanostructured materials.

In several of these instances, the association between the morphology of ZnO surfaces and antibody immobilization effectiveness has not been fully explored. Therefore, an understanding of antibody functionalization methods on various ZnO nanostructured morphologies might have direct implications for the creation of improved biosensors for the sensitive and accurate detection of important pathogens such as *Escherichia coli* (*E. coli*). This might aid in immobilizing biorecognition components and using low antibody concentrations for a single and precise detection response.

Thus, the present study comprehensively investigates the synthesis of 1DZnO materials using the metal catalyst assisted vapor phase growth technique. It explores various parameters, including gas flows, temperature, pressure, mass, and substrates, to establish the ideal operational conditions for producing ZnO nanostructured coatings with versatile morphological, structural, and optical properties. The study's outcomes enable the precise control over the orientation, length, diameter, luminescence, and surface chemistry of the synthesized nanomaterials.

Furthermore, the work examines the impact of the produced 1DZnO materials properties on their performance in various applications, such as gas sensing, biosensing, and photocatalytic hydrogen production. The results obtained in this study aim to elucidate the optimal morphological and structural characteristics of this class of nanomaterials, which can improve their performance and implementation as transducer and catalytic platforms.

Chapter III

Justification

Both globally and in Mexico, we face several issues that directly affect the population's well-being, including environmental, energy, and healthcare issues. Thus, the effective detection of high-impact diseases, the development of systems for monitoring pollutant gases, and the production of energy vectors whose consumption does not contribute to the emission of greenhouse gases are crucial goals to achieve.

This project is justified by the country's fundamental need to promote and develop materials that contribute to solving these problems. Therefore, it is necessary to deepen the basic research on the synthesis and characterization of one-dimensional ZnO nanostructures (1DZnO), in such a way that guarantees the obtaining of reproducible and adaptable platforms, for their application in the photocatalytic production of hydrogen, CO_2 detection as well as for the development of platforms for optical biosensing of *E. coli*.

Objectives

General Objective

To obtain different morphologies of 1DZnO nanostructures by the metal-assisted vapor phase growth technique for their application in photocatalytic hydrogen production, CO_2 gas sensing and immunosensing devices.

Specific Objectives

- Optimize the growth parameters in the vapor phase technique to obtain homogeneous 1DZnO nanostructured films.
- Extensive characterization of morphological, optical, and compositional properties of 1DZnO platforms by SEM, TEM, AFM, UV-Vis, XRD, PL, TRPL, FTIR, EDS, and XPS characterization techniques.
- Determine the morphological role of 1DZnO materials over their photocatalytic performance towards hydrogen evolution reaction from water splitting.
- Implement different 1DZnO coatings into chemo-resistive sensing systems for CO_2 gas detection.
- Develop a bioreceptive functionalization methodology of 1DZnO to integrate them in *E. coli* optical immunosensors.

Chapter IV Experimental methodology

Sample preparation

One-dimensional ZnO nanostructures (1DZnO) were synthesized by a metal catalyst-assisted vapor-phase growth technique. Electronic-grade crystalline silicon wafers (<100> orientation, n-type, conductivity 75–125-Ω cm^{-1}) were used as substrates for the ZnO nanostructures. These substrates were coated with ZnO and ZnO: Al thin films to function as a buffer layer (seed layer) between the substrate and the nanostructured metal oxide matrix. Experiments were also performed in which the deposition of such seed layer films was omitted, and the nanostructures were synthesized directly on the silicon surface. Subsequently, all substrates were coated with Au thin films to function as a metal catalyst during growth. The growth process was carried out in a tubular furnace using a quartz boat to place both precursors and substrates. The reactor configuration allowed control over parameters such as temperature, pressure, precursor species, gas flow, and position of the substrates during the synthesis processes. The variation of these parameters allowed modulation of the nanostructured ZnO morphologies obtained. The main stages of the metal catalyst-assisted growth mechanism (VLS) are illustrated in Figure 4.1. A detailed description of the different steps in the fabrication of one-dimensional ZnO nanostructures is given below.

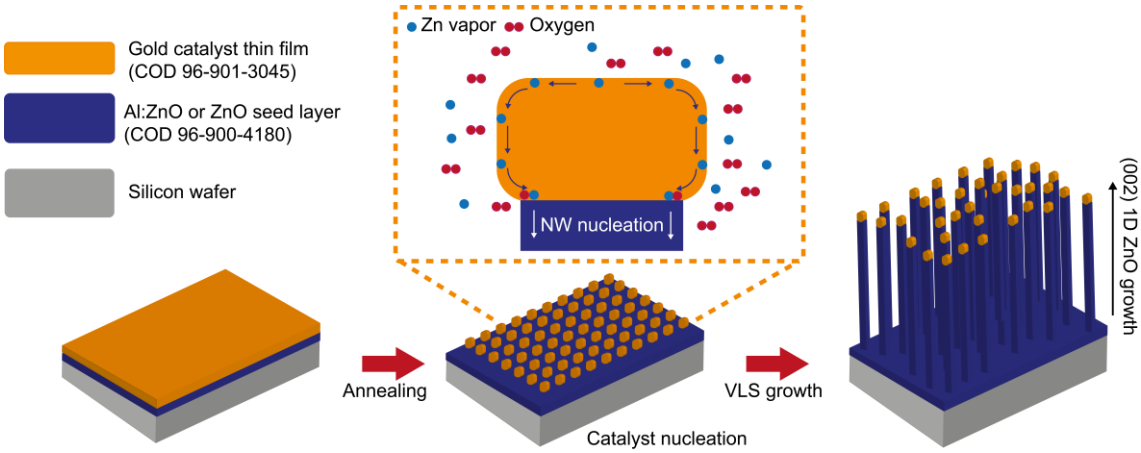

Figure 4.1 Graphical representation of the experimental process to obtain one-dimensional ZnO nanostructures. The main stages of the VLS growth mechanism are represented (i.e., metal catalyst nucleation, diffusion of the vapor species, and anisotropic nanowire crystal growth).

The synthesis and characterization experiments of 1DZnO presented in this work were carried out in the MAVER/de-nano laboratory (Low Dimensional Materials Department) and characterization laboratories of the Materials Research Institute (IIM) of the UNAM.

Seed layer preparation

Aluminum-doped ZnO and ZnO thin films were deposited by USP and sputtering, respectively. In both cases, <100> crystalline silicon substrates were used. The silicon substrates were cleaned using ultrasonic baths in deionized water,

trichloroethylene, acetone, isopropanol, and HF:HNO_3:H_2O solution (1:10:100). After each cleaning step, the samples were dried with pressurized nitrogen.

ZnO thin film

The deposition of ZnO thin films on silicon substrates was carried out using a magnetron sputtering system (Intercovamex®). A commercial ZnO PLASMATERIALS® target (2" diameter × 0.125" thick) and a target-substrate distance of 4 cm were used for the cathodic erosion process. High vacuum condition (base pressure 9.3×10^{-5} mbar) was achieved using a mechanical and turbomolecular pump arrangement. Ar (99.999%) was used as the working gas at a flow rate of 30 sccm to achieve a working pressure of 1.2×10^{-2} mbar. The control of the gas injection flow rates was carried out using a Bronkhorst® Mass Flow controller. The plasma was activated with a power of 40 W during the 60 min growth of the films.

ZnO: Al thin film

Al-doped ZnO (AZO) thin films were obtained using the ultrasonic spray pyrolysis technique. An 85 % methanol / 15% distilled water solution with 0.1 M concentration of zinc acetate dihydrate ($C_4H_{10}O_6Zn*2H_2O$) and 4.45 % atomic concentration of aluminum acetylacetonate ($Al(C_5H_7O_2)_3$) was used as a precursor for the pyrolytic reaction. The precursor solution was homogenized with a magnetic stirrer at room temperature for one hour. A nebulizer was used to volatilize the species and then to bring them to the surface of the substrates using air flows (thrust: 2.563 l/min, director: 0.642 l/min) into the synthesis chamber. To carry out the pyrolytic reaction on the surface of the silicon substrates, they were placed in a tin bath at a temperature of 475ºC. The deposits had a duration of 17 minutes.

Au catalyst deposition

After the deposition of ZnO and AZO thin films, the samples were coated with a 4 nm film of gold. A DC sputtering system (Cressington Scientific) and an Au Ted Pella® target (57 mm diameter x 0.1 mm thick) were used for the deposition of the catalyst layer. With this equipment, a base pressure of 0.075 mbar was achieved, and then an Ar flow was introduced until a working pressure of 0.100 mbar was obtained. The plasma was generated with a current of 20 mA at room temperature. Piezoelectric quartz crystals were used to estimate the thickness of the film deposited. The duration of the process was 20±2 s. As an optional step and to evaluate the nucleation effect of the Au thin films, some samples were subjected to a heat treatment at a temperature of 900ºC in an inert Ar atmosphere before VLS growth.

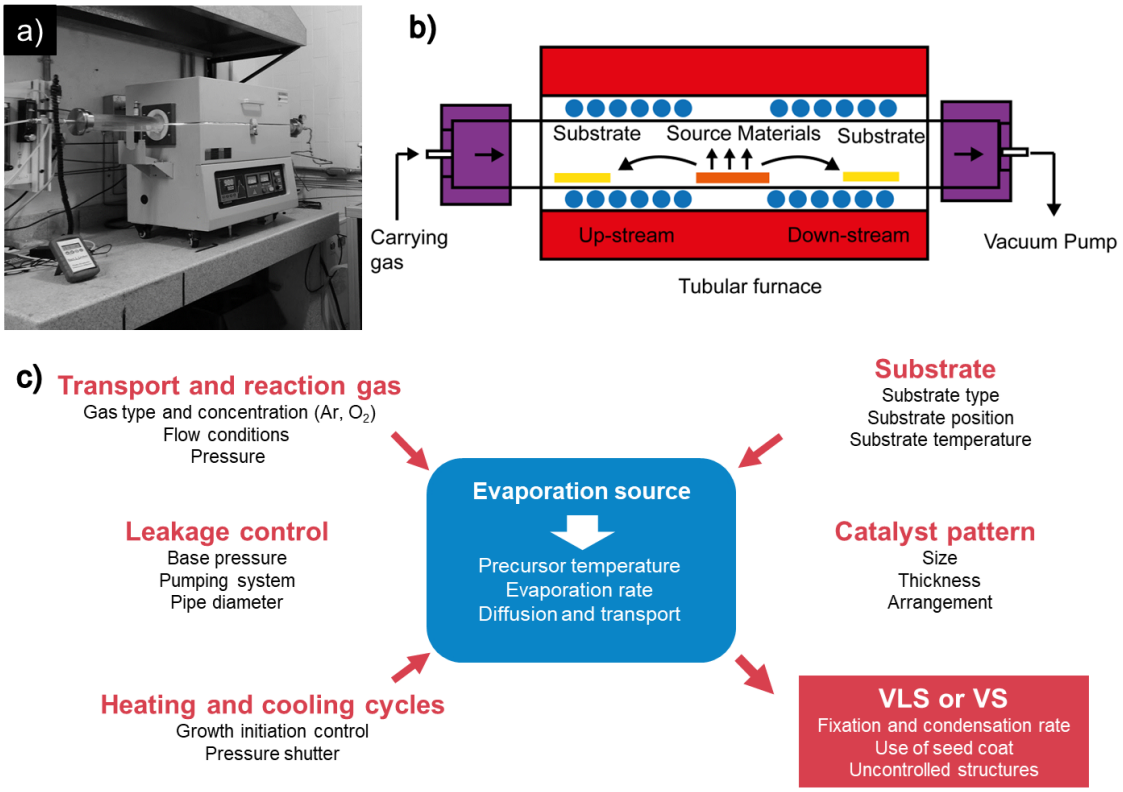

Figure 4 2. a) Photograph showing the experimental arrangement for obtaining 1DZnO nanostructures. b) Schematic of the high-temperature reactor for the fabrication of ZnO nanostructures. The production of gaseous precursor species from solid materials and their subsequent displacement to the substrate surface using transport flows is observed. c) Conceptual map showing the main variables involved in the VLS growth process of 1DZnO materials.

Vapor phase growth of 1DZnO materials

Subsequently, after plating the substrates with the gold catalyst film, vapor-phase growth of the one-dimensional ZnO nanostructures was carried out. The synthesis of the nanostructures was performed using an Intecilab® high-temperature tube furnace, as shown in Figure 4-2 (a). Figure 4-2 (b) shows a schematic of the interior of the reactor, where quartz containers inside the furnace are shown in orange and yellow. In one of the bays (yellow), the previously prepared substrates (ZnO/Au, AZO/Au, Si/Au) were placed, while in the other (orange), a 1:1 (mass: mass) mixture of ZnO:C powders were placed to generate gaseous Zn species through a carbothermal reaction at high temperatures. It is also noted that the injection of the carrier gases was connected to one end of the tube, controlled by a Mass Flow system. A mechanical extraction pump and a valve to modulate the working pressure of the synthesis were placed at the other end. The quartz vessels were positioned in such a way that the vapors produced by the precursors were displaced to the substrate surface in the same direction as the carrier flow (downstream configuration) or against it (upstream configuration).

Once the samples were placed, and the reactor was sealed, a purging process was carried out using a flow of 30 sccm of Ar. Subsequently, the heating curves

were started at atmospheric pressure. Once the desired synthesis temperature was reached, the working pressure was set, and the reactive gases were introduced. The growths had a duration of 60 min. Figure 4-2 (c) shows a conceptual map illustrating the main variables involved in the growth mechanisms in metal catalyst-assisted vapor-phase synthesis. These, in turn, define the morphological nature of the ZnO materials obtained. The parameters varied during the synthesis experiments are presented in Table 4-1.

Table 4-1. Growth conditions for obtaining different 1DZnO morphologies by vapor phase growth technique.

Precursor's temperature	900, 950 ^{o}C
Working pressure	3.5, 30, 780 mbar
Flow Gas	Ar, Ar+O_2
Ar Flow	36, 71, 500 sccm
O_2 Flow	0,1, 0.2, 10 sccm
Precursors mass	200,300 mg
Position	Upstream, Downstream
Substrate	ZnO/Au, AZO/Au, Si/Au
Previous heat treatment	0, 1

Sample characterization

Different techniques were used to characterize the morphological, structural, optical, and electrical properties of the 1DZnO materials obtained. Scanning electron microscopy (SEM), transmission electron microscopy (TEM), and scanning transmission microscopy (STEM) images were used to observe the morphological characteristics of the samples. The micrographs were obtained using JEOL JSM-7600F, LEICA Steroscan 440, JEOL ARM200F, and JEOL JEM-201 microscopes. Some samples were prepared for electron microscopy with a focused ion beam (FIB) JEOL JEM-9320FIB equipment (gallium source and a voltage of 30kV). A Nanosurf Naio atomic force microscope (AFM) was used in tapping mode to study the topography of the materials obtained. Additionally, Rigaku Ultima IV equipment was used in its grazing beam configuration (GIXRD) to determine the crystalline structure of the nanostructured films obtained.

To study the optical properties of the obtained systems, UV-Visible spectroscopy and photoluminescence techniques were used. The UV-Vis specular measurements were carried out with Filmetrics F10-RT-UV equipment using deuterium and halogen lamps as excitation sources. Diffuse reflectance measurements were performed with a Cary UV-Vis-NIR spectrometer with an integrating sphere. On the other hand, photoluminescence spectroscopy measurements were performed with a Kimmon Koha He-Cd laser (325 nm, 20 mW) as an excitation source and an Acton SpectraPro 2500i spectrometer as the detection system. Time-resolved photoluminescence (TRPL) spectra were also

measured using a Horiba Nanoled-250 pulsed source (1ns, 1-2pJ/pulse) with a wavelength of 375 nm.

X-ray photoelectron spectroscopy (XPS) and Fourier Transformed Infrared (FTIR) spectroscopy were used for the chemical characterization of the samples. The XPS spectra were obtained with an XPS PHI 5000 VersaProbe II microscope, while the FTIR spectra were measured with Bruker Vertex 70 equipment.

Samples applications

After the characterization of the obtained ZnO nanostructures, the performance of the platforms was evaluated in CO_2 sensing, photocatalytic hydrogen production, and E-coli optical biosensing applications. The experimental procedures and characterization techniques employed for these applications are described below.

Photocatalytic hydrogen evolution reaction

The photocatalytic film samples were put in water containing a combination of Na_2S (0.35 M) and Na_2SO_3 (0.25 M) as a hole scavenger agent. Afterward, thirty minutes of nitrogen bubbling were used for degassing the reactor. For the time-course kinetic studies, a 300 W Newport Xenon light source (Model: 6258, Ozone-free) was employed as an irradiation source. To discard thermal contributions to the reaction's catalytic performance, the lamp was cooled by water passing through a metal jacket. Each experiment was conducted at atmospheric pressure. The gas analysis was performed using a gas chromatograph (Bruker 450-GC) augmented with an Ar flow and a thermal conductivity detector for H_2 detection. For GC calibration, a standard gas sample with a constant concentration of hydrogen was employed. It was not possible to quantify H_2 in water, so it was ignored in the performance computations. As a control experiment, it was corroborated that in the absence of ZnO photocatalyst thin films, a combination of water/Na_2S/Na_2SO_3 cannot produce H_2 under $\lambda > 295$ nm light radiation. Further photo deposition platinization of the 1DZnO materials was carried out using an eight wt. % H_2PtCl_6 in 2µL H_2O solution[115].

The photocatalytic tests were carried out in collaboration with the University of Liverpool and Strathclyde.

CO_2 gas sensing

Silver contacts were deposited over obtained 1-D ZnO nanostructures using commercially available conductive silver printing ink (Dyesol® DYAG100 -Sigma Aldrich) for gas sensing experiments. After that, all samples were heat treated for two hours at 120^{o}C to eliminate all residues and achieve ohmic contact between the sensor layer and silver electrodes.

This is required to guarantee that resistance changes are independent of contact interface features. Next, a homemade gas detecting system was used to test each of the films in varied concentrations of carbon dioxide, namely 1, 10, 50,

100, and 200 parts per million (ppm). The system comprises a 0.8 L chamber with an integrated ceramic heater to control the sensing measurement temperature and two resistance probes linked to a Fluke 289 Multimeter to monitor dynamic sensing responses.

After placing each sample in the chamber, a mass flow controller was used to purge the chamber with various carbon dioxide concentrations to dynamic response curves. All sensing measurements were conducted at 250^{o}C, where resistance changes were recorded at temperatures lower than 250^{o}C. It is important to note that the reaction and recovery durations are determined by factoring in the corresponding 10 to 90 % change in the dynamic response curve.

Using the following equations, gas sensing parameters such as Sensing response ($S_{r\%}$), the Response time (T_{res}), and Recovery time (T_{rec}) were computed for each concentration from the dynamic responses.

$$S_{r\%} = (R_g - R_o) / R_g * 100$$

$$T_{res} = T_{Sat} - T_o$$

$$T_{rec} = T_f - T_{Sat}$$

R_g and R_o represent the resistances in the presence of carbon dioxide and air, respectively. T_o, T_{Sat}, and T_f represent the starting, maximum, and termination periods of the dynamic response curve, respectively. A schematic of the experimental setup used to measure the response of 1DZnO materials to CO_2 is presented in Figure 4-3. The CO_2 sensing tests were carried out in collaboration with the Universidad Nacional Autonoma de Hidalgo (UAEH).

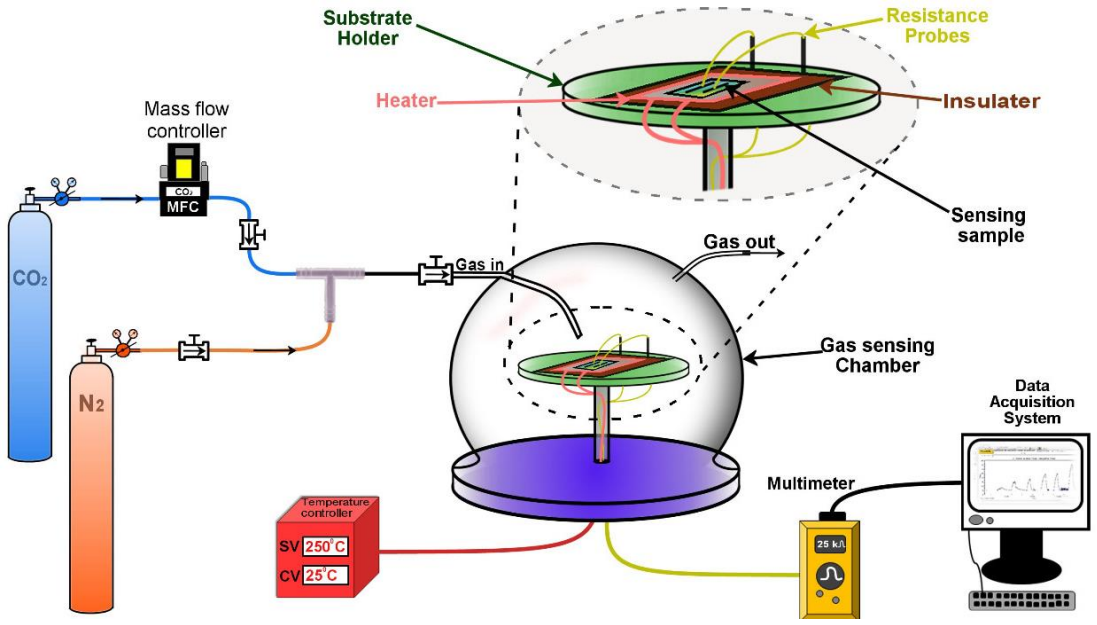

Figure 4-3. Diagrammatic illustration of the experimental set up of the CO_2 gas sensing unit.

***E. coli* optical biosensing layer**

Process 1: For the development of an optical biosensing layer on 1DZnO nanostructured coatings, the first step consisted of activating the semiconductor surface using KOH/H_2O solution for 30 minutes. After the hydroxylation of the surface, the samples were raised with water and then silanized in a 3% APTMS (3-aminopropyltrimetoxysilane) solution in acetone for 40 min. A prior thermal treatment at 110 °C for 90 min allows the polymerization of the APTMS layer. Subsequently, immobilization of anti-total *E. coli* antibodies on 1DZnO/APMS surface was carried out. For this, a 100 μg/mL antibody solution in PBS (Phosphate-buffered saline) at 4 ˚C for 60 min. Consecutive washes with PBS ensured the correct fixation of the biorecognition agents.

Process 2: With the results obtained by process 1 described above, we proceeded to select a specific 1DZnO morphology and to improve the biofunctionalization procedure employed. Thus, hydroxylation was carried out using a 0.1 M solution of KOH in methanol for 10 min. After that, the samples were washed with methanol and silanized with three different methodologies. The methodologies are described in Table 4-2.

Table 4-2. Improvement of functionalization strategy for the selected 1DZnO morphology.

Strategy	Silanization conditions	Contact time
Ac20	1% APTMS solution diluted in $(CH_3)_2$ CO	20 minutes
Ac5	1% APTMS solution diluted in $(CH_3)_2$ CO.	5 minutes
Tol	1% APTMS solution diluted in anhydride toluene	10 minutes

All samples were then washed using acetone and annealed at 110ºC for 90 min. Then, anti-flagella *E. coli* antibodies were attached to the 1DZn/APTES surfaces (Ac, Ac5, Tol) using a 30 μg/mL antibody solution in PBS (4 ºC for 60 min). Three subsequent PBS washes (5 min each) were used to reduce unspecific IgG adhesions.The Bradford method was used with BioRad Bradford protein assay to quantify the antibody immobilization efficiency in a Thermofisher Scientific Multiska GO Microplate spectrophotometer. For further details in the methodology please refer to Salinas. et. al.[116]. The biofunctionalization tests were carried out in collaboration with Centro de Investigación en Biotecnología Aplicada (CIBA)-IPN.

Chapter V. Results: Sample obtention

Seed layer preparation: ZnO and AZO thin films

The thin films that were deposited on silicon substrates by sputtering and USP techniques are shown in Figure 5-1 (a-f). Panel (a) shows a photograph of the Ar plasma used to perform the erosion of the ZnO target. The deposition plate can be seen in the top part of the chamber. Systematizing the working conditions, obtaining ZnO thin films with a thickness of 117±5 nm (determined by morphological analysis of cross-section SEM micrographs) as a homogeneous coating on the whole substrate surface was possible. Figure 5-1 (b-c) shows the scanning electron micrographs of the deposited ZnO films. The surface is made up of grains of similar sizes to each other. In addition, no important differences are observed in the contrast of the secondary electron image, so it is valid to assume that there are no abrupt variations in the roughness. On the other hand, the system used to obtain AZO-type seed coatings is shown in Figure 5-1 (d). Homogeneous coatings of 650±30 nm were obtained with this system. The grains of the film surface was observed by scanning electron microscopy images, where it can be observed that the grain size obtained is larger than those of the films synthesized by sputtering. It can also be seen that the morphology of the grains is different for each technique. Those obtained in the USP samples show edges associated with a better crystallinity, in contrast to the rounded grains of the sputtering samples related to a more amorphous character.

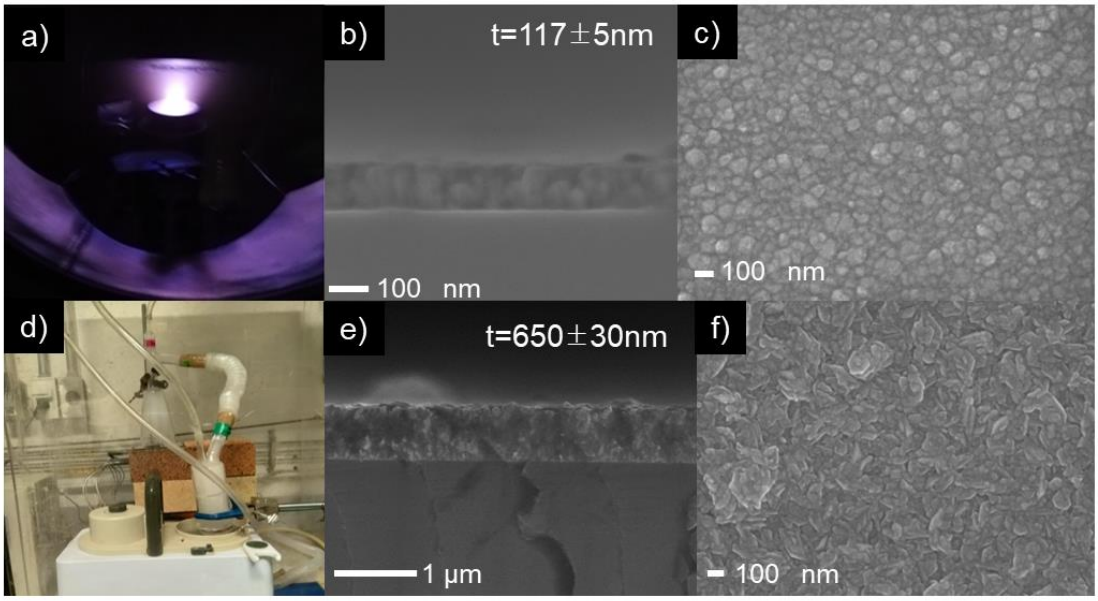

Figure 5-1. (a) Photograph of the deposition plasma for obtaining ZnO thin films by the sputtering technique. (b-c) SEM micrographs showing the morphology of the samples in (b) cross-section and (c) top view. (d) Photograph of the USP equipment for the growth of AZO films. (e-f) Scanning electron microscopy images of the synthesized AZO films in (e) cross-section and (f) top view.

GIXRD measurements made it possible to determine the crystalline structure of the synthesized films. The diffractograms of the coatings obtained by both synthesis techniques are shown in Figure 5-2 (a). In the two cases, the crystalline system's identification coincided with the wurtzite phase of ZnO (ICSD-193696).

The AZO films show a polycrystalline character in which the crystalline planes (100), (002), (101), (102), (110), and (103) are identified, with (101) having the highest relative intensity. In contrast, ZnO coatings deposited by sputtering show a preferential orientation presenting peaks (002) and (103) only. The peaks in the latter samples show a considerable broadening due to the reduction of the crystallite size (higher degree of amorphism), which is consistent with the observations made through electron micrographs. It is also possible to distinguish a shift between the positions of the peaks towards higher values of the Bragg angle of the AZO samples with respect to the ZnO films because of the effect of doping with Al atoms.

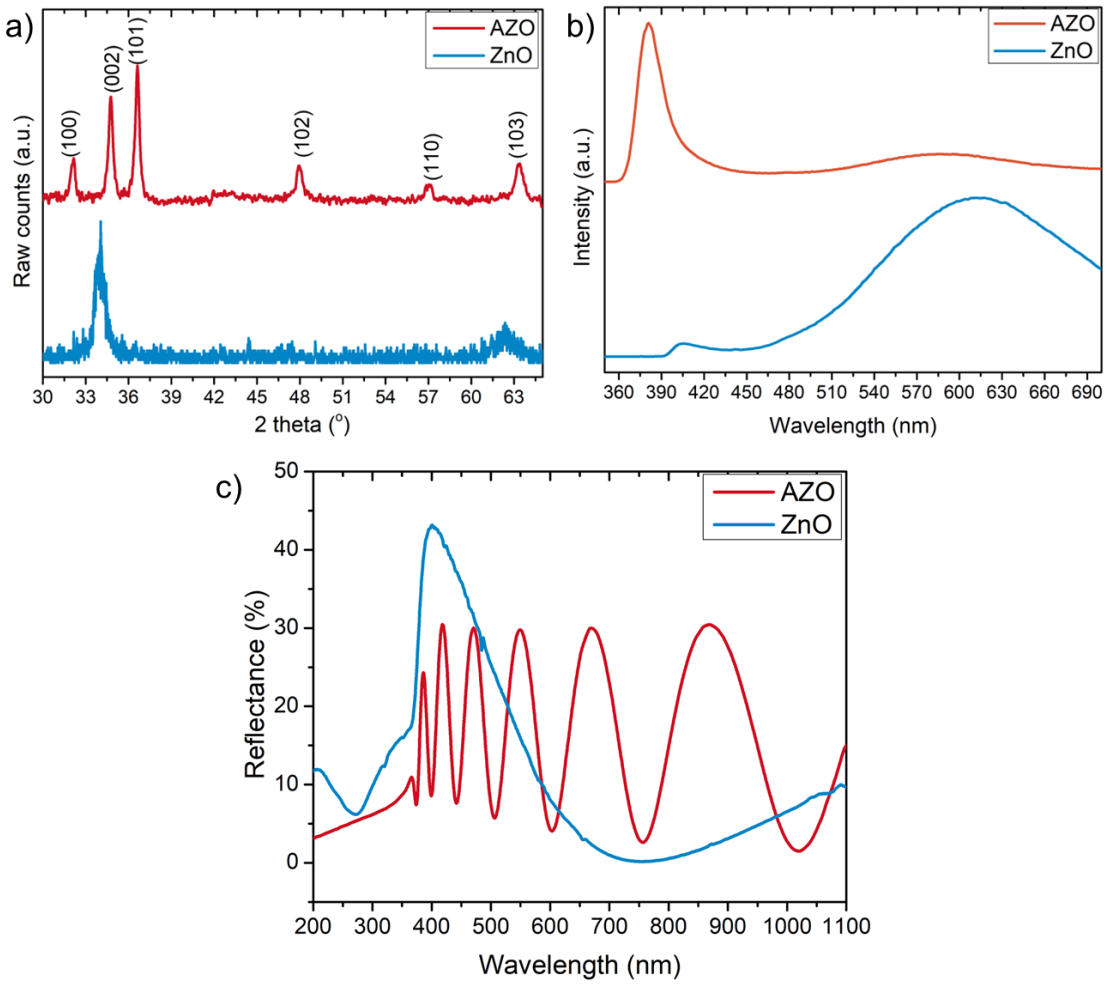

Figure 5-2. (a) X-ray diffractograms in grazing incidence mode, (b) photoluminescence spectra, and (c) specular reflectance spectra of synthesized AZO and ZnO samples.

Figure 5-2 (b) shows the photoluminescence spectra of ZnO films with and without doping. The spectra are very different, observing the presence of an emission in the UV region for the AZO samples and a broad band in the visible region for the ZnO samples. The emission process is due to excitonic band-band recombination when the emission is centered in the UV region. On the other hand, the ZnO-based films present an emission in the visible region which is attributed to recombinations with radiative centers generated within the band as

a result of point defects in the ZnO structure (e.g., vacancies, interstitials, antisites). The fundamental difference between the optical properties of the two types of coatings lies in the reactive and thermal conditions under which the samples are synthesized. In the case of the USP technique, the high temperature and the presence of an oxygen-rich atmosphere inhibit the formation of point defects in the ZnO lattice.

On the contrary, the inert atmosphere and low-temperature conditions of the sputtering system allow the formation of imperfections responsible for the visible emission of the material. Figure 5-2 (c) shows the obtained specular reflectance spectra of the coatings. As can be seen, there is also a significant difference between the optical properties of the two systems. From the number of local maxima present in the spectra, it is possible to state that the thickness of the AZO films is greater than that of the ZnO films. Using the Kubulka Munk model, values for the optical band gap of the samples were determined, obtaining results of 3.2 eV and 3.4 eV for the AZO and ZnO samples, respectively.

Metal catalyst deposition

Once the seed layer thin films were obtained, a series of studies of the optical and morphological properties of the metal catalyst used was performed. Due to the scalable nature of the sputtering process with respect to that of the USP system, the seed layer-catalyst studies were completed using only ZnO films. Figure 5-3 (a) shows a photograph of the DC sputtering equipment that coats substrates with Au thin films. As discussed in the experimental section, polished silicon and ZnO-coated silicon substrates were metalized. Figure 5-3 (b) shows a SEM image of ZnO films with the Au catalyst layer. From the contrast of the image, it is possible to state that a homogeneous coating of the semiconductor is obtained with the deposition conditions used in this work. Subsequently, some samples were subjected to a thermal treatment at 900^{o}C before the 1DZnO growth to study the effect of thermal treatments on the catalyst nucleation. In this way, Au nanoparticles (AuNPs) of quasi-spherical morphology with diameters of (55±17) nm were obtained on the substrates coated with ZnO films (Figure 5-3 (c)). When the catalyst deposition was performed directly on Si substrates, the AuNPs obtained presented a diameter of (45±13) nm (Figure 5-3 (d)).

Likewise, specular reflectance spectra were measured at the different stages of incorporation of the metal catalyst on the different substrates used (Figure 5-3 (e-f)). The first of these graphs shows the changes in reflectance generated by different Au morphologies on ZnO-coated substrates. A blue shift of the minima of the reflectance curves associated with absorption maxima is observed as one goes from ZnO->ZnOAu film-> ZnOAu NPS. This kind of behavior originated from a resonance process of the Au plasmon and presented a strong absorption in the green region of the visible spectrum. The same phenomenon is presented in samples where Au is deposited directly on silicon substrates. In these systems, the 520-550 nm Au plasmon band is observed for the SiAu (film) sample. The reflectance of the SiAu(NPs) system with respect to SiAu(film) is increased due

to the direct Si substrate surface exposure, which has a considerably higher reflectance than the catalyst film.

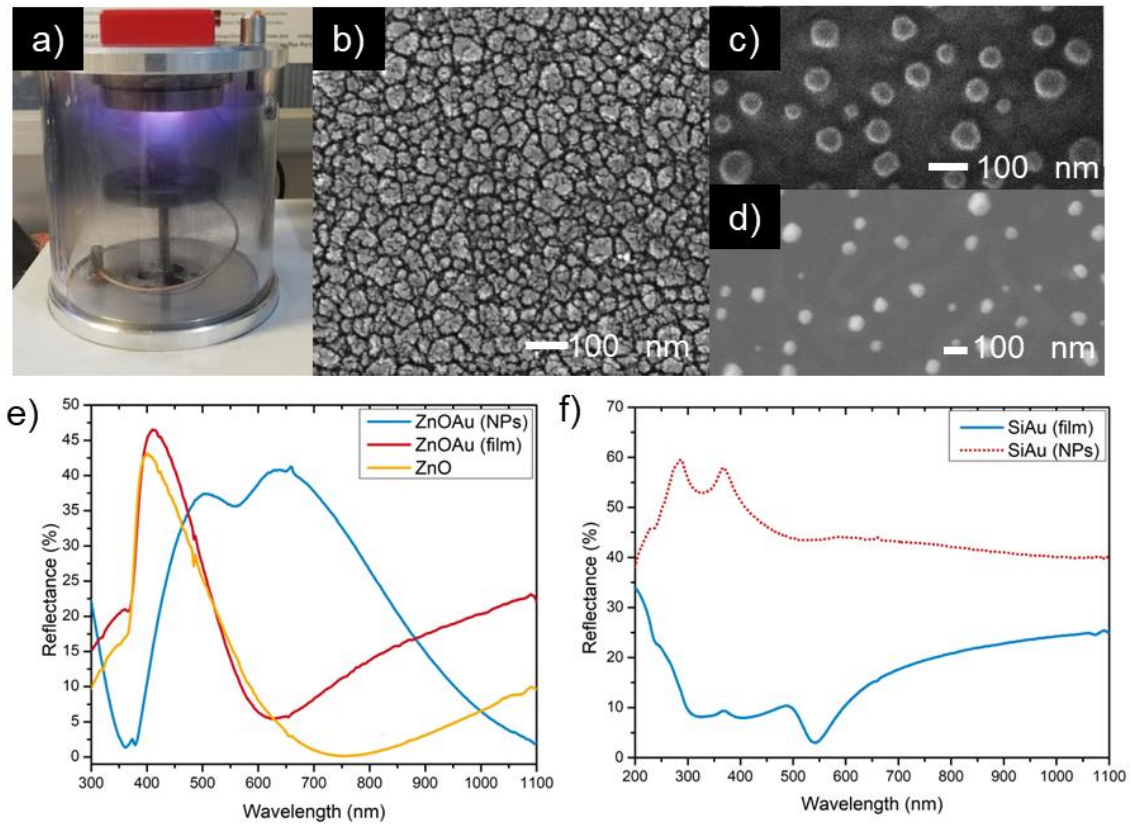

Figure 5-3. (a) DC sputtering equipment is used to obtain Au catalyst films. (b) SEM micrograph in top view showing the homogeneous metallic coating of ZnO semiconducting surface. (c-d) Catalyst nucleation process on (c) ZnO-coated substrates and (d) Si wafers. (e-f) Specular reflectance spectra of both metalized semiconductor substrates.

Vapor phase growth of 1D nanostructures

With all these considerations regarding the preparation of the substrates, a series of experiments were carried out to obtain 1DZnO nanostructures with particular emphasis on controlling the morphological, structural, and optoelectronic properties. Figure 5-4 shows some of the different morphologies obtained by the metal catalyst-assisted vapor phase growth technique. The radar graphs schematizing the synthesis conditions used to obtain the morphologies shown in the corresponding micrographs are also presented in Figure 5-4. The numerical assignment in the graphs responds to the following numerical code: Position (1: upstream, 2: downstream) and Substrate (1: SiAu(film), 2: SiAu(NPs), 3: ZnOAu(film), 4: ZnOAu(NPs), 5:AZO). The working conditions are also summarized in Table 5-1.

Hence, it is possible to observe the versatility offered by the technique in terms of control over morphological parameters of 1DZnO materials such as orientation, length, diameter, and even the simultaneous formation of 2D structures at the base of the 1D nanostructured matrix (1DZnO_4). In all cases, the obtained

platforms offer a considerable increase in terms of surface area compared to thin film materials. The conditions explored during the development of this project have allowed the obtaining of coatings conformed by 1DZnO structures with lengths ranging from 0.7 µm to 20µm and with diameters ranging from 39 nm to 150 nm.

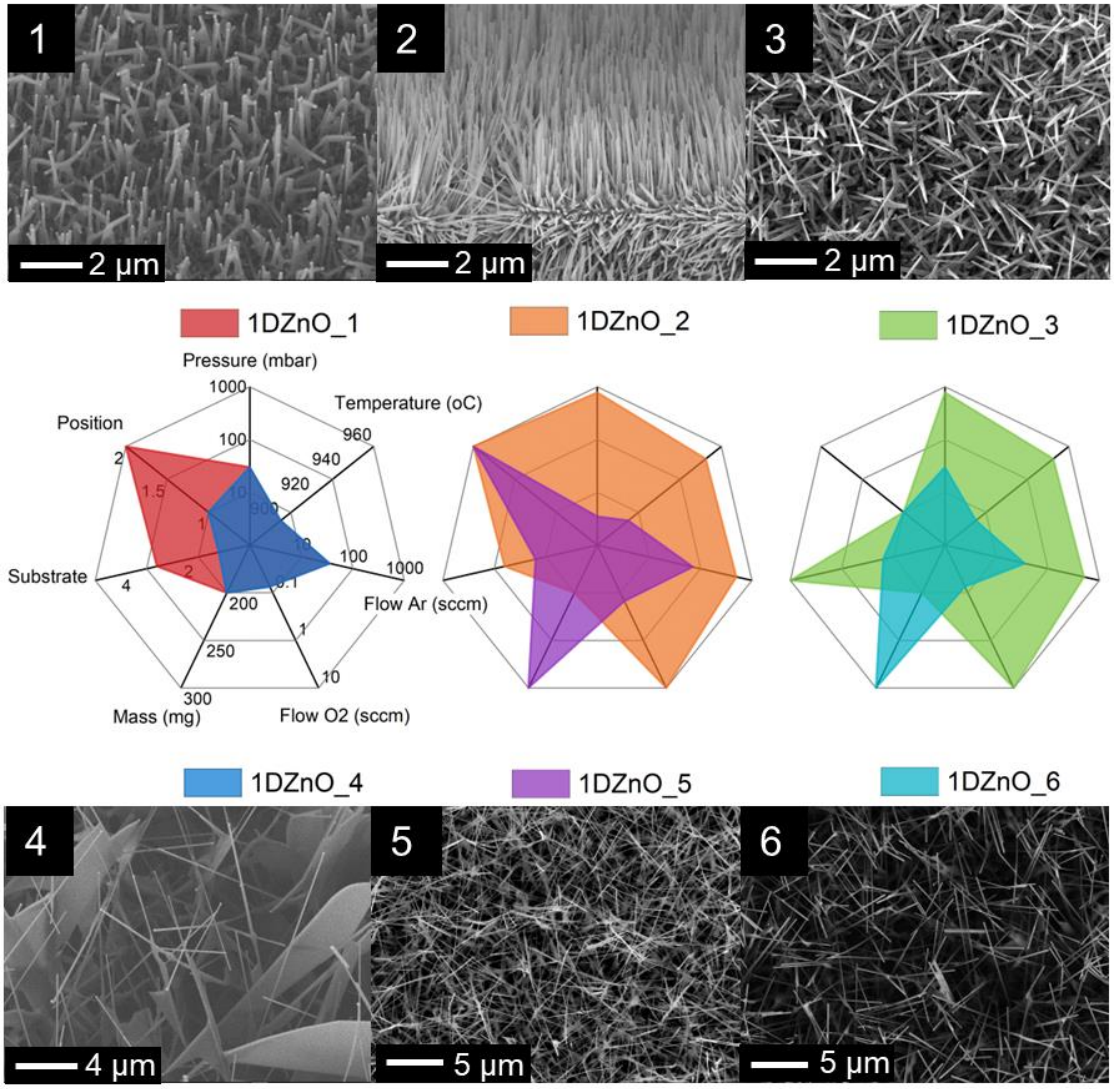

Figure 5-4. Different morphologies of one-dimensional ZnO nanostructures obtained by the metal catalyst-assisted vapor-phase growth technique. Scanning electron microscopy micrographs show varying working conditions' effects on ZnO nanostructured materials' length, diameter, and orientation. Radar plots illustrate working conditions used for synthesizing different morphologies of 1DZnO.

With high-resolution contrast images (backscattered electron signals), it was possible to observe the presence of gold nanoparticles at the tip of the ZnO backbone matrix. Later, by means of TEM electron diffraction the cubic gold structure was also corroborated in tip of a single 1DZnO nanostructure. This fact is strong evidence that the growth mechanism followed by the nanostructures is a metal catalyst-assisted one. Furthermore, given the high temperatures at which these experiments were carried out, the catalyst phase was in the liquid state.

Given the phases' coexistence, the system's growing mechanism is also known as vapor-liquid-solid (VLS). Hence, the control and study of the Au film and nanoparticles used as seeds for the growth process play a fundamental role in the morphological characteristics of the 1DZnO coating obtained.

Table 5-1. Growth conditions for obtaining different 1DZnO morphologies by vapor phase growth technique. DS: downstream, US: upstream configurations.

Sample	1DZnO_1	1DZnO_2	1DZnO_3	1DZnO_4	1DZnO_5	1DZnO_6
Pressure (mbar)	30	780	780	30	3.5	30
Temperature (°C)	900	950	950	900	900	900
Flow Ar (sccm)	35.7	500.0	500.0	35.7	71.4	71.4
Flow O_2 (sccm)	0.1	10.0	10.0	0.1	0.2	0.2
Mass (mg)	200	200	200	200	300	300
Substrate	ZnOAu	ZnOAu	AZOAu	SiAu	SiAu_HT	ZnOAu_HT
Position	DS	DS	US	US	DS	DS

One of the most important parameters for obtaining repeatable and controllable 1D morphologies of ZnO is the partial oxygen concentration in the growth atmosphere. While the carbothermal reaction of the precursors causes volatile Zn species to be generated, the presence of a slightly oxidizing atmosphere is necessary for the formation of ZnO at the Au-ZnO growth interface. However, the presence of an atmosphere with excess oxygen causes the total oxidation of carbon in the ZnO: C mixture and thus inhibits the reduction process necessary to produce gaseous Zn species. The operating window for this work was 2% oxygen with respect to the Ar content in the furnace.

In addition, another implementation made to the reactor was the addition of a pressure shutter. The improvement consists of employing a pressure reduction so that the precursor species can increase their mobility rate and reach the growth interface on the substrate surface. In this way, by operating with vacuum conditions during the growths, it was possible to obtain homogeneous 1DZnO coatings even in the upstream position and with flows up to 72 sccm, as shown in Figure 5-5. In this last figure, we can observe the effect of varying the working pressure and pressure during vapor phase growths using substrates with and without the seed layer. With this series of experiments, it was possible to determine that at too low-pressure conditions (3.5 mbar), the formation energy for a vapor-solid-solid growth mechanism is reduced, thus leading to the formation of two-dimensional ZnO structures (walls) simultaneously. These results also provided evidence of the possibility of obtaining 1D ZnO nanostructures of considerable length (10 µm) directly on Si substrates without the need of a buffer layer, which implies a significant reduction in the processing times for the fabrication of this type of material.

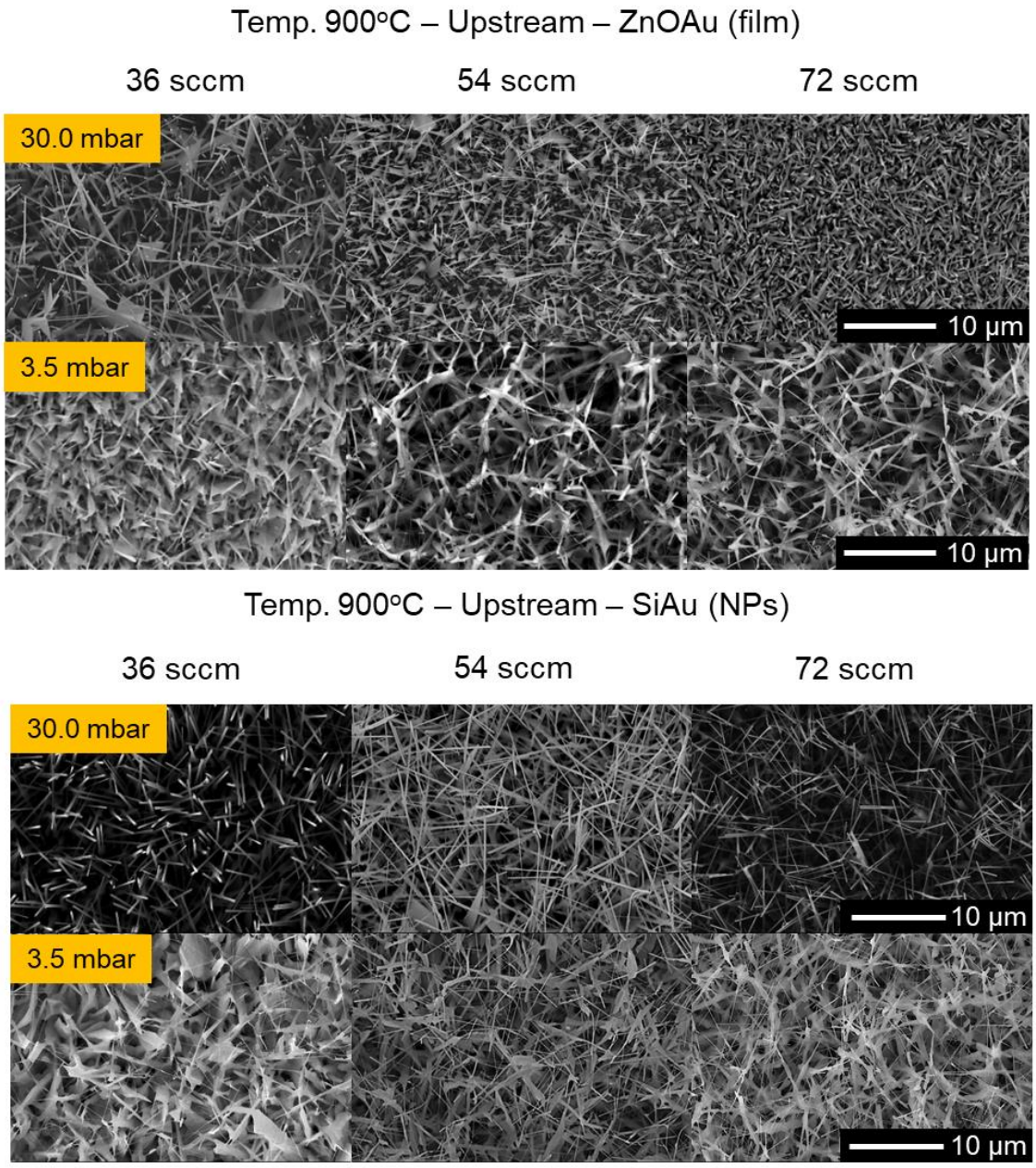

Figure 5-5. SEM images show one-dimensional ZnO nanostructured coatings on SiAu(NPs) and ZnOAu(film) substrates under different flow rates and working pressures in the upstream configuration.

Figure 5-6 (a) shows the X-ray diffractograms measured in a grazing incidence configuration. With these measurements, it was possible to identify that the crystalline phases of the ZnO nanostructures correspond to a hexagonal system (ICSD-193696) while the catalyst crystallizes in a cubic phase (ICSD- 611625).

The difference between the diffraction patterns depends on the orientation of the structures with respect to the plane of the substrate, where it could be determined that the presence of several planes of high intensity corresponds to the growth of ZnO crystals in a disordered manner. On the other hand, the preferential orientation for the (002) and (103) planes is a product of the growth of ZnO crystals in a favored direction, resulting in highly aligned nanostructures.

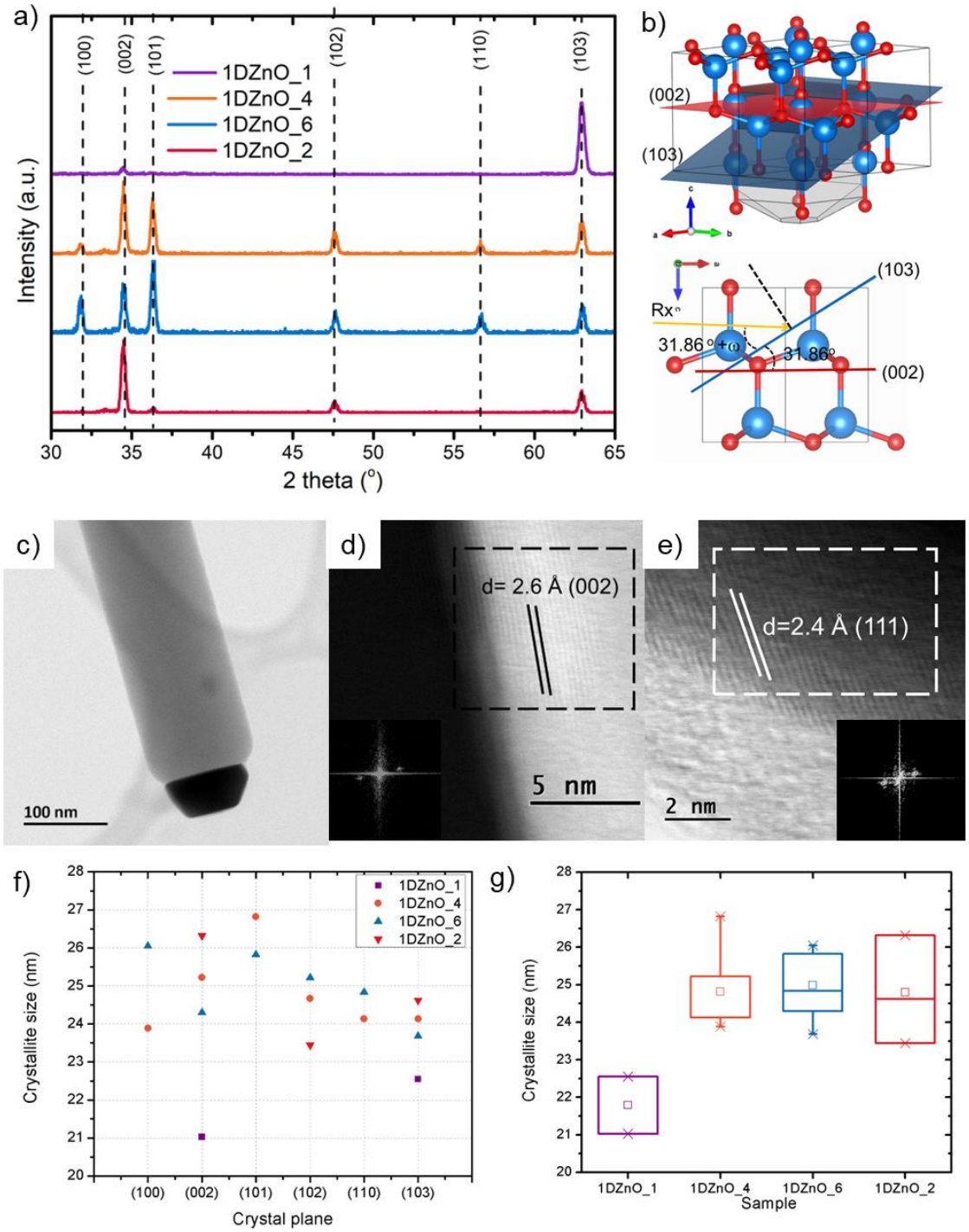

Figure 5-6. (a) X-ray diffractograms showing the different dominant planes obtained as a function of the orientation of 1DZnO nanostructures. (b) A model describing the Bragg condition between incident X-rays and the (103) / (002) planes. (c) TEM micrograph showing compositional contrast of ZnO-Au interface. (d-e) HRTEM images showing interplanar distances of (d) ZnO backbone matrix and (e) Au catalyst nanoparticle. (f) Crystallite sizes calculated from the Debye Scherrer equation. (g) Box plots showing the crystallite sizes determined for each of the studied samples.

It's worth noting that the high intensity of the (103) reflection in one of the diffractograms shown in Figure 5-6 (a); it appears to imply that this plane has a

preferred orientation. Naturally, due to the employed grazing incidence setup, reflections from crystal planes parallel to the surface must be avoided, and the preferred orientation of the (103) plane may be in a direction other than normal to the surface. To understand this orientation, one must consider the following correlation: the angle between the (103) and (002) planes in the ZnO nanostructure is 31.86, which is highly similar to the Bragg angle of the (103) planes (31.54). As depicted in Figure 5-6 (b), the incident grazing rays are roughly in the Bragg condition for the (103) plane when the (002) plane is parallel to the surface of the substrate. In other words, detecting a high-intensity (103) reflection in the grazing incidence setup corresponds to the parallel orientation of the (002) plane with respect to the surface. Grazing incidence diffractograms can be used to determine the preferred orientation.

The earlier observation regarding the preferential orientation suggests that 1DZnO (or a significant number of them) are vertical, with their axis parallel to the surface. Therefore, the existence of additional peaks in the diffractograms is not due to the polycrystalline nanostructure structure but rather to the orientation of a portion of the single-crystal nanostructures in distinct directions.

Figure 5-6 (c) depicts a transmission electron microscopy image where the contrast between the nanostructure's tip and the support matrix is visible. In this regard, bright spots correlate to the heavier element (Au), whereas the dark areas correspond to the lighter compound (ZnO). HRTEM images were used to later support this claim. Near the growth interface, (002) ZnO (d=2.6 Å, ICSD-193696) and (111) Au (d=2.4 Å, ICSD-611625) planes were revealed by Fast Fourier Transform (FFT) analysis of these micrographs. Consequently, the tip is composed of gold (cubic), whereas the support has a hexagonal ZnO structure. The appearance of Au nanoparticles at the tip proves that the metal effectively promoted the growth mechanism, hence favoring the production of 1DZnO nanostructures in all samples.

Considering the FWHM (Full Width Half Maximum) values of the XRD diffraction peaks in Figure 5-6 (a), the crystallite sizes were determined using the Debye Scherrer equation. The resulting sizes were calculated for each sample based on all the peaks observed. These results are displayed in Figure 5-6 (f). It is noteworthy that although there is a slight variation in crystallite size among the samples, no discernible distinction is evident in the sizes calculated for different crystal planes within the same sample. This outcome is not expected, as the confinement of the nanostructure would likely affect grain size differently across various planes. Nevertheless, such an effect is only significant in ultrathin structures, as demonstrated in the research conducted by Xiong et al[117]. In their study, they report the production of ZnSe nanobelts measuring 5 nm in thickness, where differential broadening between distinct crystalline planes is observed.

Hence, given that the diameters of the 1DZnO nanostructures are in the range of hundreds of nanometers, there is no substantial disparity in the broadening of the peaks in the diffractograms (Figure 5-6 (g)). This finding aligns well with the outcomes reported in other studies involving 1DZnO structures of comparable dimensions to those explored in this research[118–120].

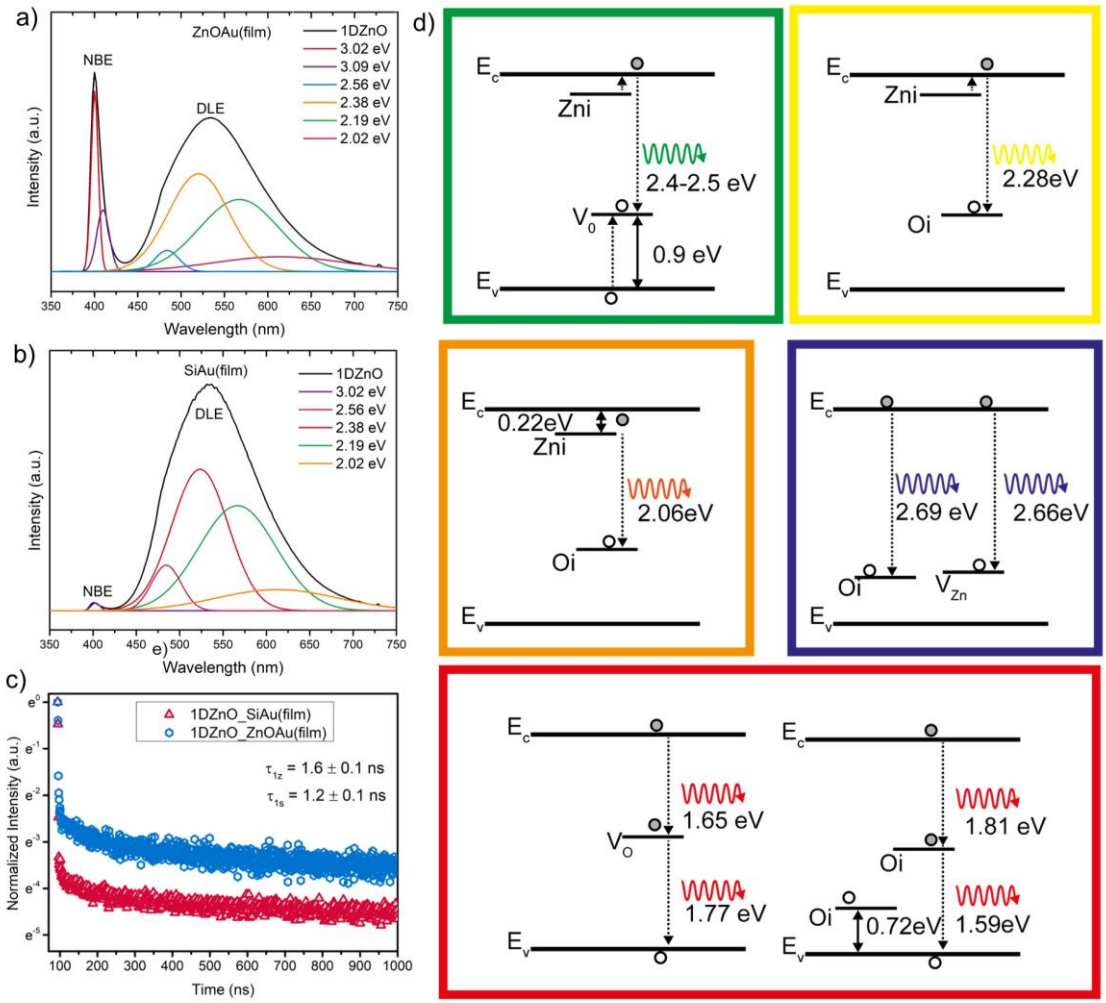

Figure 5-7. (a-b) Photoluminescence spectrum of 1DZnO nanostructures at room temperature (Black). Deconvolution curves (color). Inset displaying NBE band in a sample of 1DZnO grown without the use of seed layer. (c) Dynamic decay spectrum measured at 3.3 eV. d) DLE transitions associated with emissions in different regions of the visible spectrum[121].

To determine the optical properties of the systems, the photoluminescence of the materials synthesized with and without the use of a seed layer (labeled in this case as 1DZnO_za and 1DZnO_sa respectively) was measured (Figure 5-7 (a-b). In both instances, two emission bands were observed. The first is located near the edge of the ultraviolet spectrum and is linked to band-to-band recombination (NBE: near band emission). The other is located in the visible region and has a defect-related origin (DLE: deep-level emission).

The proportion between the intensities of such emissions is a valuable indicator of the defect concentration in the produced nanostructures [121–123]. Thus, in circumstances where I(NBE)/I(DLE)<1, the major emission process can be referred to as defect recombination. ZnO intrinsic imperfections such as vacancies (absent Zn or O atoms), antisites (Zn->O or O->Zn atoms inversion), and interstitials (extra Zn or O atoms) are abundant. They have been demonstrated to be accountable for some features of the material's optoelectronic behavior[124]. Deconvolution of the PL spectra was done to explain in detail the relationship between the distinct emission bands found in the

samples and the related recombination centers (color curves Figure 5-7 (a,b)). In both instances, Gaussian curves were employed to model the emission. Affiliating the fitting curves with point defects described in the literature, zinc vacancies (V_{Zn}) and zinc interstices (Zn_i) were identified as material defects associated with blue emissions (3.09, 3.02 eV)[125,126]. In addition, single-charged zinc vacancies (V_{Zn}^-) and oxygen vacancies (V_O) were attributed to the cyan (2.56 eV)[127] and bright green band emission(2.38 eV)[128], respectively. Lastly, the yellowish green (2.19 eV) and orange (2.02 eV) emissions were correlated to V_OZn_i complex vacancy[126] and oxygen interstice (O_i)[129] in turn.

Moreover, employing time-resolved photoluminescence, the lifetimes of excitons in the materials were measured (Figure 5-7 (c)). Based on the nature of the decay, an exponentially decaying adjustment was applied. ($I=A_1\exp(-t/\tau_1)+A_2\exp(-t/\tau_2)+A_3\exp(-t/\tau_3)$). In samples prepared with the use of ZnO seed layer, time decay constants of τ_{1z}=1.6±0.1 ns, τ_{2z}=101±7 ns, and τ_{3z}=1095±61 ns (R^2=0.95) were determined, whereas for samples grown directly over Si substrates values of τ_{1s}=1.2±0.1 ns, τ_{2s}=209±46 ns and τ_{3s}=2014±969 (R^2=0.96) were calculated. It is generally known that decays in the range of a few ns are related to free exciton radiative recombination[130].

On the other hand, non-radiative phonon emission phenomena are responsible for faster recombination rates (ps order)[131]. The carrier lifetimes determined in this study are longer than those previously reported for comparable ZnO nanostructures(0.26 ns ZnO nanorods[130], 0.35 ns ZnO tetrapods[132]). Because of the high defect concentration in the lattice, the carrier radiative recombination ratio of the semiconductor is increased. In addition, it was observed that the radiative recombination process is size-dependent, implying that the lifetime rises as the size grows[133]. It is being reported that the thermal excitation mechanism among sub-band-gap states can enhance the lifetime of ZnO materials to the millisecond scale for moderate and slow decay (τ_2 and τ_3)[134]. A summary of the opto-structural characteristics of the above-mentioned materials is given in Table 5-2.

Table 5-2. Opto-structural characteristics of 1DZnO nanostructured coatings synthesized with and without the use of ZnO seed layer. Diameter, aspect ratio (AR), dominant emission wavelength and time decay constant are shown.

Sample	Diameter (nm)	AR	λ_{max} (nm)	τ_1 (ns)
ZnOAu(film)	152±59	21.1±0.1	411± 2	1.6±0.1
SiAu(film)	118±52	12.7±0.1	521± 2	1.2±0.1

Considering the above, control over the morphology and optical properties of 1D ZnO nanostructures can be achieved through the presented synthesis technique. Moreover, the tunable longitude, diameter, orientation, structure, and luminescent features are significant and essential for their incorporation in optoelectronic applications. As will be explored in the coming chapters, they include photocatalytic hydrogen generation, CO_2 gas sensing, and optical biosensing development.

Chapter VI Results: Photocatalytic hydrogen evolution

After gaining expertise in the vapor transport synthesis approach for obtaining diverse morphologies of 1DZnO nanostructures[135], the influence of the morphological and optical features of ZnO-based nanomaterials on the photocatalytic hydrogen evolution reaction efficiency is described. Adjustment in the synthesis method's growth parameters enabled optimizing the aspect ratio, surface area, and orientation of the 1DZnO nanomaterials for stable and efficient photocatalytic activity in the water-splitting process. The present section clarifies the operating parameters (substrate temperature, seed layer, and the use of diverse carrier gas mixes) required to obtain crystalline, morphologically regulated, and pure 1DZnO nanostructures for improved water-splitting efficiency. This work was published in the International Journal of Hydrogen Energy (2020), doi: 10.1016/j.ijhydene.2020.08.247 (IF: 7.139), with the title: Photocatalytic hydrogen production performance of 1-D ZnO nanostructures: Role of structural properties[136].

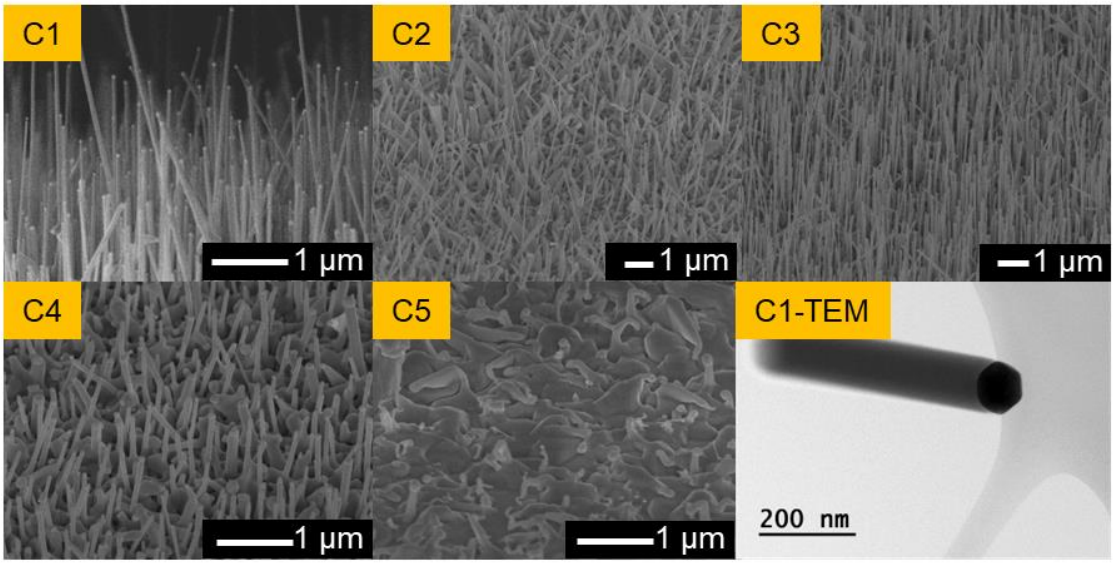

Figure 6-1. C1-C5: SEM micrographs of 1DZnO nanostructures obtained by vapor transport growth assisted by a metal catalyst. Light-field TEM images of single 1DZnO nanostructure.

Figure 6-1 illustrates SEM micrographs of the 1DZnO nanostructures grown by the vapor transport technique mentioned in previous sections. For these experiments mechanism, a mixture 1:1 ZnO:C mixture was used for carbothermal reduction in a 1:1 ratio using an Ar flow of 8.33×10^{-6} m^3/s for 60 min at a pressure of 780 mbar. A change in the morphology as a function of growth conditions can be observed. The conditions for the obtention of such samples are presented in Table 6-1. The resulting nanostructures grow primarily in two orientations, as evidenced by SEM images. Samples C1 and C3 present many 1DZnO nanostructures growing vertically (002 orientation), generating an almost 90° angle with the substrate plane.

In other words, homogeneous coatings of the substrate with vertical-orientated 1DZnO materials were obtained with these conditions.

Table 6-1. Growth conditions and structural parameters of the samples 1DZnO materials obtained by vapor transport growth technique. Mono (M) and polycrystalline (P) AZO thin films were used as seed layers.

Morphological parameters					
Sample	T [°C]	O_2/Ar ratio	Substrate	D [nm]	L [mm]
C1	950	~2%	AZO_M	57±16	2.77±0.51
C2	950	~2%	AZO_P	85±24	2.55±0.55
C3	950	<2%	AZO_M	56±12	2.19±0.39
C4	950	<2%	AZO_P	62±18	0.77±.25
C5	400	~2%	AZO _M	-	-

In some instances, 1DZnO structures also grow at an angle of around 65°. (C2 sample). The growth direction of the nanostructured ZnO matrix depends epitaxially on the seed layer, where for the C2 sample, a polycrystalline AZO thin film was used instead of a monocrystalline one (samples C1, C3, and C5). In contrast to samples C1 to C3, sample C4 lacks the anisotropic crystallization of ZnO, causing the formation of shorter nanostructures. These samples verify the fundamental function of the O_2/Ar mix ratio, which is used as a carrier gas during the vapor transport process. By analyzing the kinetics connected with the Au nanocatalyst, it is possible to understand the effect of O_2 on nucleation development. It is essential to note that neither solid nor liquid gold offers soluble media for O_2. Thus, diffusion of O_2 to the growth Au-ZnO interface cannot occur via the catalyst drop. The elevated growth rate at a higher partial oxygen pressure is explained by a stable adhesion coefficient of the Zn atoms in the Au catalyst and their subsequent oxidation to ZnO at the substrate interface. A steady adhesion coefficient of Zn atoms in the gold catalyst and their subsequent oxidation to ZnO at the growing interface is responsible for the increased growth rate at a more significant partial oxygen pressure. The results of the morphological statistical analysis performed on the SEM micrographs of samples C1-C4 are shown in Table 6-1. Sample C5 features small structures whose morphologies are not well-controlled, and distribution is not uniform across the substrate's surface. This sample demonstrates the influence of the comparatively low temperature during growth which impacts the kinetics of the nucleation[32]. Liquid metal catalysis cannot be induced at temperatures below 650 °C since Au film cannot melt and permit the diffusion of Zn species to synthesize 1DZnO.Therefore, low-temperature samples must be produced through a VSS (vapor-solid-solid) mechanism in which the Zn(g) species are adsorbed mainly on the solid surface of the catalyst[137]. In this instance, the parameters utilized to produce these samples did not permit the formation of a uniform nanostructured coating; hence no statistical analysis of the morphology was performed.

In the TEM micrograph shown in Figure 6-1, a distinct contrast between the tip and axial support can be observed, so no significant dispersion of Au throughout the structure can be expected. This kind of interface between a noble metal and a semiconductor can decrease the probability of electron-hole recombination, causing more proficient charge separation and, thus, increasing the photocatalytic performance. Compared to the traditional metallization approach in which metal deposition occurs after synthesis, the current growth technique enables obtaining 1DZnO nanostructures with in-situ metal nanoparticles on their tips. This finding encourages using the obtained materials in photocatalysis applications such as hydrogen generation.

X-ray diffractograms of the distinct 1DZnO morphologies are shown in Figure 6-2 (a). Features in the scanning electron micrographs (SEM) agree with those obtained in the XRD spectra, namely, patterns characterized by a single diffraction peak corresponding to the micrographs' highly oriented arrangement. Despite the nanostructure growth, samples C1, C2, and C3 kept the dominating (002) peak, which is associated with *c*-oriented crystal growth. Multiple crystallographic orientations are visible in the pattern for sample C5, where the substrate temperature was significantly lower than in other experiments. In this case, the primary orientation is toward the (103) peak. The difference in the number of peaks in the diffractogram indicates the shift from VLS to VSS in the nanostructure's growth mechanism. In addition, a peak of gold is present in each pattern, which corresponds to the metal catalyst used during the synthesis. Although the growth parameters for samples C1 through C4 are similar, the Ar/O_2 and seed layers differ significantly.

As depicted in Figure 6-2 (a), samples (C1 and C3) that grew highly aligned were those for which monocrystalline (002) oriented AZO films were employed, hence preserving preferential growth in this orientation. Instead, numerous oriented 1DZnO were formed in the C2 sample using a polycrystalline AZO layer. These results demonstrate the epitaxial link between the nanostructure formed and the seed layer employed. In contrast, a lower O2 concentration effect in the carrier gas mixture was explored for samples C3 and C4, in which shorter structures were obtained in either crystal-oriented AZO films. With these results, the effects of epitaxial and chemical factors on the morphology of 1DZnO materials were investigated.

Figure 6-2 (b) illustrates the reflectivity of 1DZnO samples. In ZnO materials, absorption under 400 nm is ascribed to the intrinsic band-to-band electron transition. As demonstrated in Figure 6-2 (b), samples with greater aspect ratios (C1, C2, C3) exhibited a decreased reflection in the visible region. Due to their more specular surface, samples C4 and C5 exhibit a greater reflectance than the other three samples. Reflectance data suggests that the shape-dependent light response of 1DZnO structures may lead to improved light trapping features and, consequently, to enhanced photocatalytic activity. The observed oscillations in samples C4 and C5, as opposed to C1-C3, may be attributed to their heterogeneous nature or thickness, resulting in an interference behavior of the reflectance spectra.

Figure 6-2 (c) displays typical emission spectra of the different 1DZnO samples. As formerly indicated, a strong emission between 450 and 660 nm can be seen, which is related to deep-level defect recombination (DLE). PL emission in the green region is commonly attributed to oxygen vacancies (V_O), i.e., electrons recombine with photo-promoted holes occupying oxygen vacancies states in the band gap of the material, resulting in the visible luminescence phenomena[138]. Additionally, PL emission is influenced by other variables, including crystalline nature, surface morphology, composition, and doping. The ratio between the intensities of the near-edge excitonic (NBE) and DLE bands was determined to estimate the contribution of the defect levels in the radiative process. Therefore, I (NBE)/I (DLE) ≈ 0.001 for the 1DZnO given in this work shows that DLE emission greatly predominates over excitonic recombination.

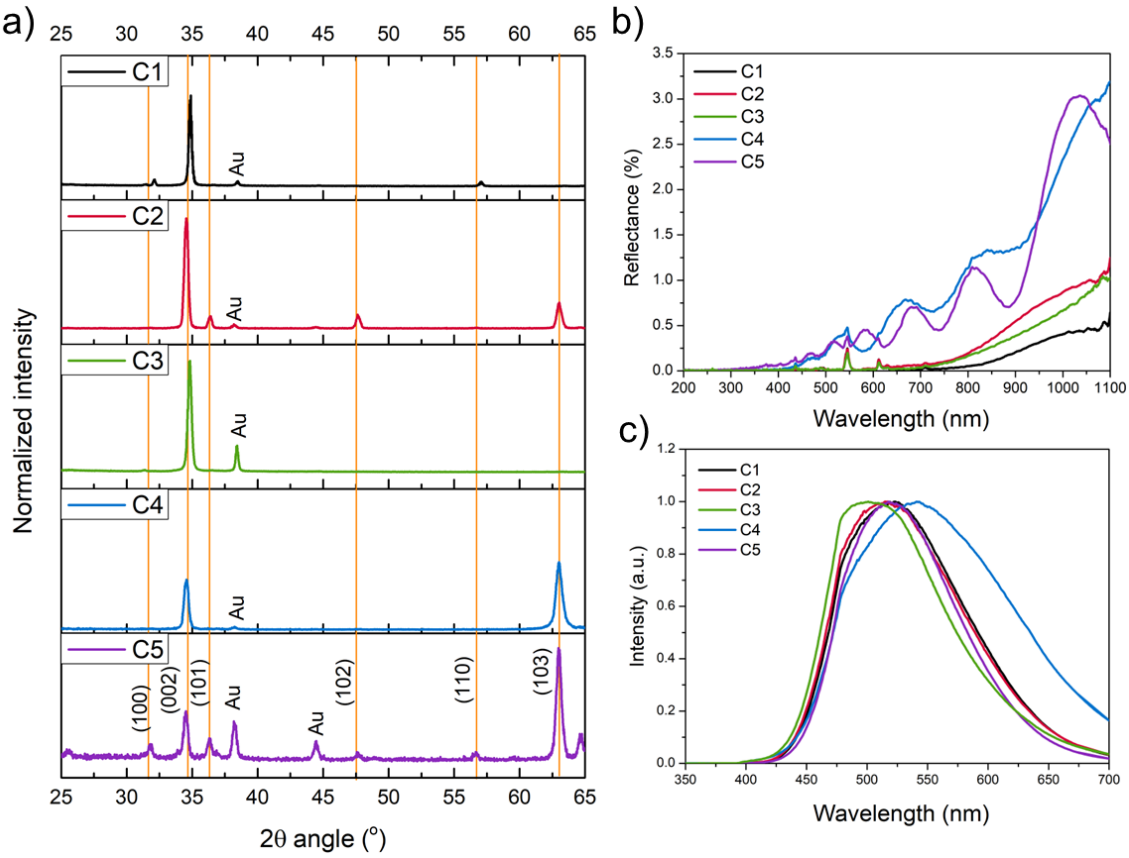

Figure 6-2. (a) GIXRD diffractograms of 1DZnO nanostructures (C1 to C5); (b) UV-Visible reflectance spectrum and (c) PL emission of ZnO based 1D nanomaterials (C1 to C5).

The tailored defects occurring in semiconductors surface could be utilized as especially active photocatalytic sites for reactions such as CO_2 reduction, N_2 fixation, and hydrogen generation (HER), according to earlier research[139]. This approach is referred to as defect engineering. By adding unsaturated defects, specific molecule adsorption sites could be produced. Defect engineering is thus a technology that holds promise for developing photocatalytic applications besides water splitting.

Careful examination of the geometrical properties of the 1DZnO samples was performed to correlate the morphological features with the photocatalytic reaction performance. By calculating the volume and surface area occupied by the nanostructures (according to their average diameter and length) per geometric film surface, an estimation of the 1DZnO's active mass on the samples was found. The results are presented in Figure 6-3 (a).

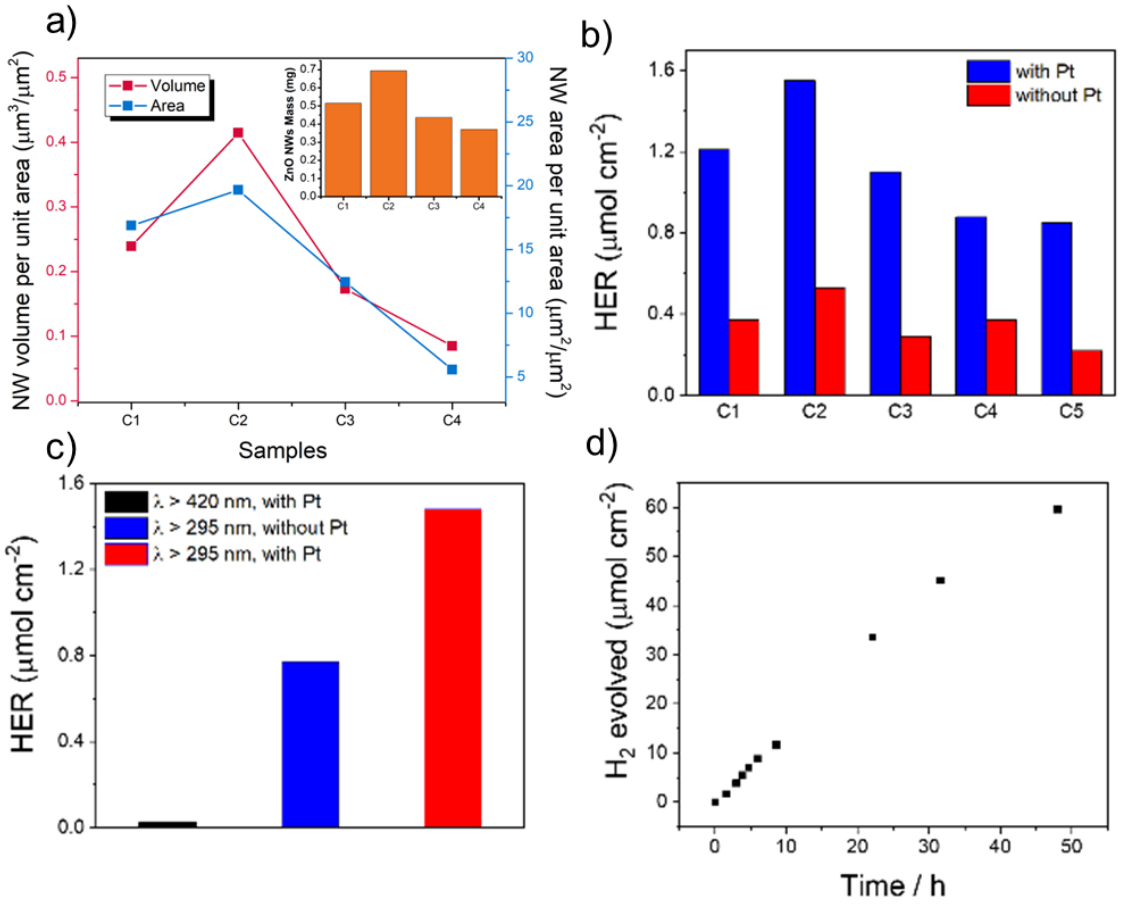

Figure 6-3. (a) (Left) Surface and (Right) volume of 1DZnO materials per geometric substrate surface. (Inset) 1DZnO matrix estimated mass. (b) Evaluation of the photocatalytic hydrogen production performance of 1DZnO films (red: without Pt addition, blue: platinized) under 300 W illumination (λ> 295nm) for 5 hours. (c) HER of sample C2 under different spectral filters and both with and without the addition of co-catalyst. (d) Hydrogen evolution reaction over time for co-catalyzed C2 sample under λ > 295 nm irradiation.

Next, when a hole scavenger agent was present, the hydrogen evolution reaction from proton reduction of the 1DZnO materials was studied. The benefit of retrieving the photocatalyst from the solution when using 1DZnO matrices supported by solid substrates over commonly reported suspension systems could be beneficial in upcoming scalable applications. In the addition of a Na_2S/Na_2SO_3 solution (hole-scavenger), all 1DZnO materials generated hydrogen from water.

As shown in Figure 6-3 (b), under 300 W illumination and λ> 295nm, sample C2 presented the best hydrogen production performance (0.53 μmol cm^{-2}). The other samples exhibited generation rates between 0.37-0.22 μmol cm^{-2}. Without adding a co-catalyst, no HER was observed in any of the materials under visible

illumination. Therefore, after photo platinization of the systems, an improvement in the water splitting reaction was reflected for all tests under broadband illumination (1.21, 1.55, 1.10, 0.88, 0.85 µmol cm^{-2}; for C1, C2, C3, C4, and C5 respectively. Figure 6-3 (b)). The performance trend with and without a co-catalyst is comparable, where it was noted that the C2 morphology with the addition of a co-catalyst presents the best HER efficiency under visible illumination (0.02 µmol cm^{-2}) Figure 6-3 (c). Thus, it can be concluded that ZnO coating nano structuration results are beneficial, as inhomogenus1DZnO films (C5) present the lowest photocatalytic response. For structures with high form factors (C1-C3), a better response is obtained for larger diameter structures. It is, therefore, possible that the diameter and orientation of the ZnO matrix determine the rate at which the excitons reach the semiconductor surface, as well as the light-trapping properties of the system. Finally, to determine the stability of the platinized C2 sample, the HER of the system was monitored for 50 hours under broadband illumination. The results (Figure 6-3 (d)) show no significant changes in the activity of the photocatalyst, thus corroborating the stability of the films used in the H_2 production reaction.

Chapter VII. Results: CO_2 gas sensing

This section describes a straightforward, cost-effective, and time-efficient method for growing one-dimensional ZnO nanostructures (NWs/NRs) for use as a CO_2 gas sensor. Furthermore, a comparison is made between the opto-structural and gas sensors properties of 1DZnO nanostructures grown both with and without a seed layer and with two different gold catalyst thicknesses (2 and 4 nm). The sensing properties of CO_2 gas at varying concentrations were studied, and NWs with a seed layer exhibited a relatively greater sensing response. In comparison, no seed-layered samples (NRs) responded twice as fast. Direct growth of 1D ZnO nanostructures on silicon wafers will facilitate their integration with conventional fabrication techniques for gas sensing devices. The results presented in this section were published in the Journal Sensors and Actuators: B. Chemical, Vol 337 (2021), doi: 10.1016/j.snb.2021.129765 (IF: 9.221), with the title: One-dimensional Au-ZnO hybrid nanostructures based CO_2 detection: Growth mechanism and role of the seed layer on sensing performance[140].

The 1DZnO nanostructures were prepared using 2 and 4 nm Au catalyst films deposited on USP-AZO films and directly on Si <100> substrates. The samples are then categorized as 1D-USP (structures obtained using AZO seed layers deposited by USP) and 1D-NSL (samples where no seed layer was used). Furthermore, depending on the thickness of the Au catalyst film employed (4 / 2 nm), the samples were labeled as 1D-USP-Au2, 1D-USP-Au4, 1D-NSL-Au4, and 1D-NSL-Au4. The synthesis experiments were carried out at a temperature of 950^{o}C and a pressure of 780 mbar. As a precursor, 200 mg of a ZnO:C mixture was used in a 1-to-1 ratio. All materials were obtained in the downstream configuration with an Ar/O_2 flow of 500 sccm (2 % oxygen).

Figure 7.1 (a-b) shows SEM images of the 1D-USP and 1D-NSL samples employing 4 nm catalyst films. Using similar images, it was possible to determine the lengths and diameters of the synthesized nanostructures. When substrates were coated with USP seed layers, the lengths were 2.63-4.52 µm and diameters of 39-87 nm for samples with 2 and 4 nm of gold, respectively. It can be corroborated then that longer and thicker 1DZnO are obtained by using thicker catalyst films. On the other hand, for samples with no seed layers (1D-NSL) were employed, the length and diameter values determined were 1.96-1.59 µm and 56-85 nm for samples with 2 / 4 nm Au respectively.

It has been previously reported that the lattice mismatch between the substrate and the nanostructure to be synthesized plays an important role in the morphology obtained. In the particular case of ZnO and Si, the mismatch corresponds to 41 % Ievtushenkoa et al. [141]. Most of the works report the use of thin buffer films between the two semiconductors. In addition, thermal oxidation of the Si substrate to SiO_2 has also been reported as a possible mechanism of inhibition to the growth of 1DZnO nanostructures by reducing the availability of epitaxial nucleation sites[142]. Despite this, obtaining semiconducting ZnO nanostructures on silicon substrates is of great interest as it would allow this type of array to integrate in commercial optoelectronic devices.

Some authors determine that an efficient relaxation of the growth interface determines that the growth of the 1D structure becomes an energetically favorable process. Thus, depending on the mismatch between the substrate and the nanostructure, critical radii values are proposed (*Rc*), below which the growth of 1DZnO is promoted by the effective relaxation of the interface stress [143–145] In the SEM images of Figure 7-1 (a-b) it is also possible to observe the presence of Au nanoparticles at the tip of the ZnO arrays. This supports that the predisposing mechanism in the growth of 1DZnO in these experiments was metal catalyst assisted. With this, it is validated that it is possible to obtain structures with specific characteristics to perform in specific applications through the selection of the growth conditions.

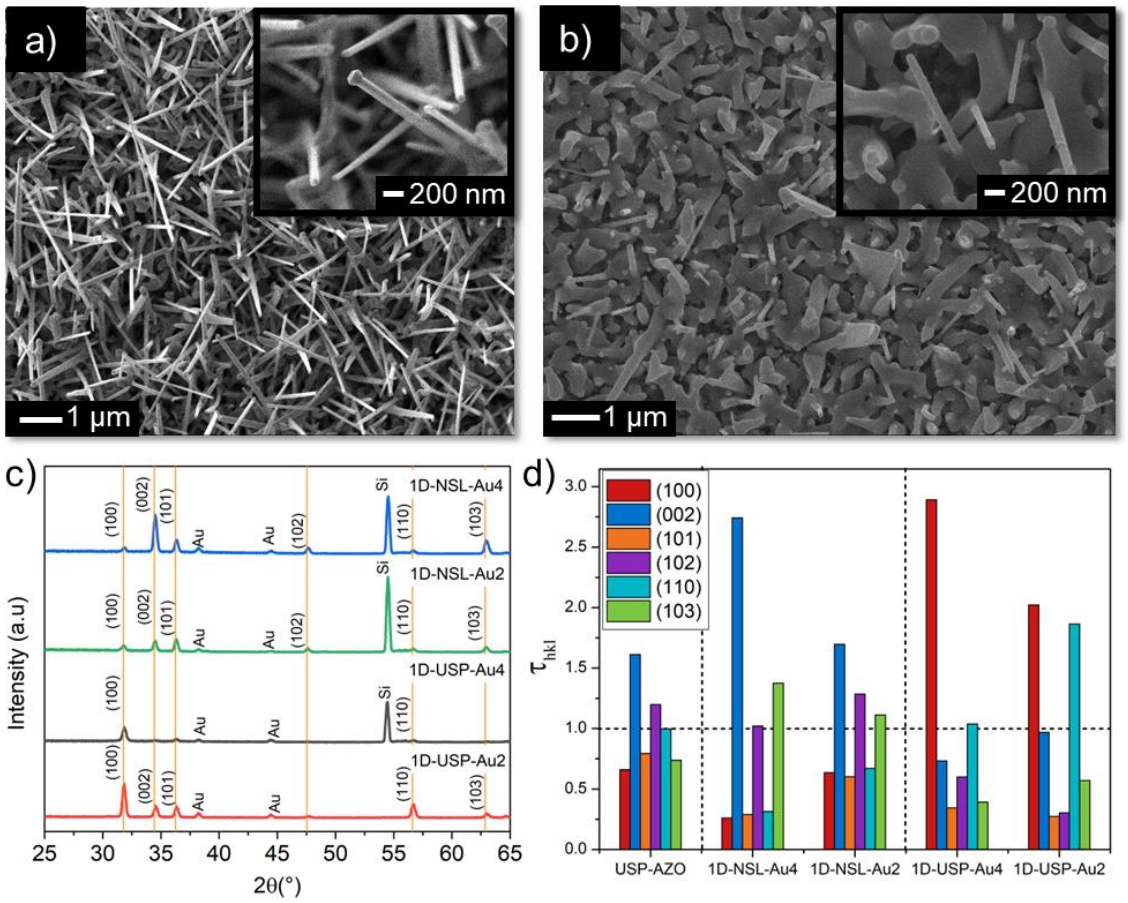

Figure 7-1. (a-b) SEM images of 1DZnO samples synthesized with (a) the use of AZO seed layer deposited by USP and (b) directly on silicon substrates, using 4 nm Au as the catalyst. (c) GIXRD diffractograms for 1D-USP and 1D-NSL samples with 4 / 2 nm Au. (d) Texture coefficients of the AZO seed layer and NSL/USP 1DZnO samples catalyzed with both 4 and 2 nm of Au.

The GIXRD spectra of the obtained samples are shown in Figure 7-1 (c). By identification of the diffraction peaks present, the presence of ZnO in its wurtzite phase was corroborated in all the synthesized samples. The presence of two peaks (38.1º and 44.1º) associated with the metal catalyst was also observed. In the case of the samples obtained directly on Si, a polycrystalline character and a

preferential orientation different from that of the USP samples were observed. To study in more detail the role of the seed layer on the growth of the 1DZnO, the relative crystalline orientations were determined by calculating the texture coefficients of the coatings:

$$\tau_{hkl} = \frac{I_c^{hkl}/I_0^{hkl}}{\frac{1}{N}\sum_N \left[\frac{I_c^{hkl}}{I_0^{hkl}}\right]}$$

I_0^{hkl} is the reference intensity of the reflection associated with the hkl family of planes in a powder sample. *N* corresponds to the number of diffraction peaks analyzed. Figure 7-1 (d) shows the calculated texture coefficients for the 1DZnO samples and the AZO-USP film used. In these plots, we can observe that the (002) plane presents a preferential orientation (greater than 1) for the NSL samples and the AZO seed layer. This coincidence can be explained by taking as a reference the model of Glas et al.[146]. In this work, the authors report that the initial phases of the nucleation process of one-dimensional semiconductor nanostructures resemble the Volmer-Weber mechanisms of thin film growth without considering the radial confinement associated with the metal catalyst. Thus, since both thin film and 1DZnO-NSL are grown directly on the same type of single-crystal substrate, the orientation of the systems is expected to be similar. For the 1DZnO-USP samples, peaks (100) and (101) are observed with high intensity, corresponding to inclined orientations with respect to the substrate surface. The preferential orientation of the structures in these directions is due to the polycrystalline characteristics of the substrate used, resulting in the axial growth of the ZnO matrix in multiple directions. These results are consistent with previous work[135,147] and the morphologies observed by SEM (Figure 7-1 (a)).

The chemical features of the synthesized 1DZnO systems were studied by XPS spectroscopy. The broad scanning spectra (0-1100 eV) of all samples are presented in Figure 7-2 (a). In these spectra, the characteristic signals of zinc (Zn3s, Zn3p, Zn3d, and Zn2p), oxygen (O1s), carbon (C1s), and gold (Au4f7) orbitals were observed. Auger electron signals were also detected. Spectra calibration was performed using the carbon 1s orbital (285 eV) as a reference. Spin-orbit splitting (23 eV)[148] between the $Zn2p_{3/2}$ (1021.7 eV) and $Zn2p_{1/2}$ (1044.6 eV) orbitals was observed in all samples. Once the characteristic signals were identified, high-resolution measurements of the $Zn2p_{3/2}$ orbital were performed for all samples (Figure 7-2 (b)). By a deconvolution process, it was possible to observe a different shift for specific samples, suggesting the appearance of Zn in different oxidation states.

On the one hand, the most intense peak (1021.8 eV) present in all samples has been associated in the literature with both metallic Zn or Zn^{2+} present in the ZnO lattice[149,150]. The deviation of this signal at higher energies can be explained by the generation of structural defects, mainly oxygen vacancies. Thus, the appearance of a second peak (1023.1 eV) in both USP samples indicates a deviation of the compound's stoichiometry[151]. In the case of the 1DZnO-NSL samples, this second peak presented a different shift, which may be due to differences in defect density or surface chemistry with respect to the 1DZnO-USP

samples. The presence of various oxidation states in Zn indicates can indicate a departure from the ideal wurtzite structure, implying the existence of point defects or stoichiometry deviation. This observation was further supported by analyzing the signals from the O1s orbital.

The signal localized at (1023.9 eV) for the 1DZnO-NSL-Au2 sample has been previously related to zinc hydroxide[152]. In contrast, the 1022.42 eV signal in the 1DZnO-NSL-Au4 sample coincides with the reported shift for the $Zn2p_{3/2}$ orbital resulting from defect generation in ZnO nanostructured materials[153,154].

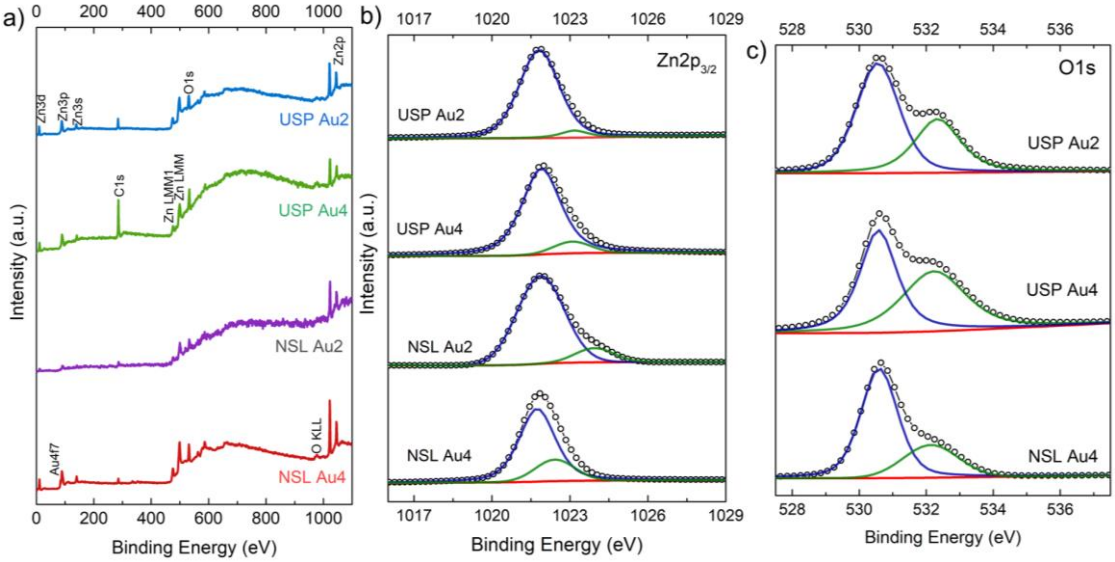

Figure 7-2 (a) XPS broad scan spectra of the synthesized 1DZnO samples. Signals associated with Zn, O, Cu and Au are labeled. (b-c) XPS measurements of (b) Zn2p3/2 (c) O1s orbitals for different 1DZnO samples. Fitting using Lorentzian-Gaussian curves. Background in red.

However, the poor energetic separation between the different oxidation states of Zn evaluates other peaks necessary to corroborate the statements made. Therefore, the systematic evaluation of the O1s orbital was performed for all the samples, appreciating the appearance of an asymmetric main peak (Figure 7-2 (c)). The main contribution of this signal was consistently set at 530.6 eV in all spectra. This value shows a shift to higher energies with respect to the standard value of 530 eV for O^{2-} present in ZnO, so it is commonly associated with the formation of reduced zinc oxide (i.e., ZnO_x). Thus, it is corroborated that there is a deviation from the stoichiometry of the obtained materials. The asymmetric character of the signal (532.2 eV) has been linked to the adsorption of OH/O groups[148,151]. Finally, it was possible to detect the presence of the $4f_{7/2}$ (83.7 eV) and $4f_{5/2}$ (87.4 eV) Au orbitals. Due to the electronic interaction at the metal-semiconductor interface, a shift of these signals towards lower energies was observed with respect to the values of the orbitals in the bulk metal: Au $4f_{7/2}$ 84.0 eV and Au $4f_{5/2}$ 87.6 eV[155].

In addition, PL measurements showed a broadband emission centered in the green region for all the synthesized materials. As discussed in previous sections, the most accepted mechanism to which these radiative recombinations are

attributed is associated with oxygen defects (2.31-2.37 eV, V_O[128]), which confirms that these are responsible for the compound stoichiometry deviation, as observed in the XPS measurements.

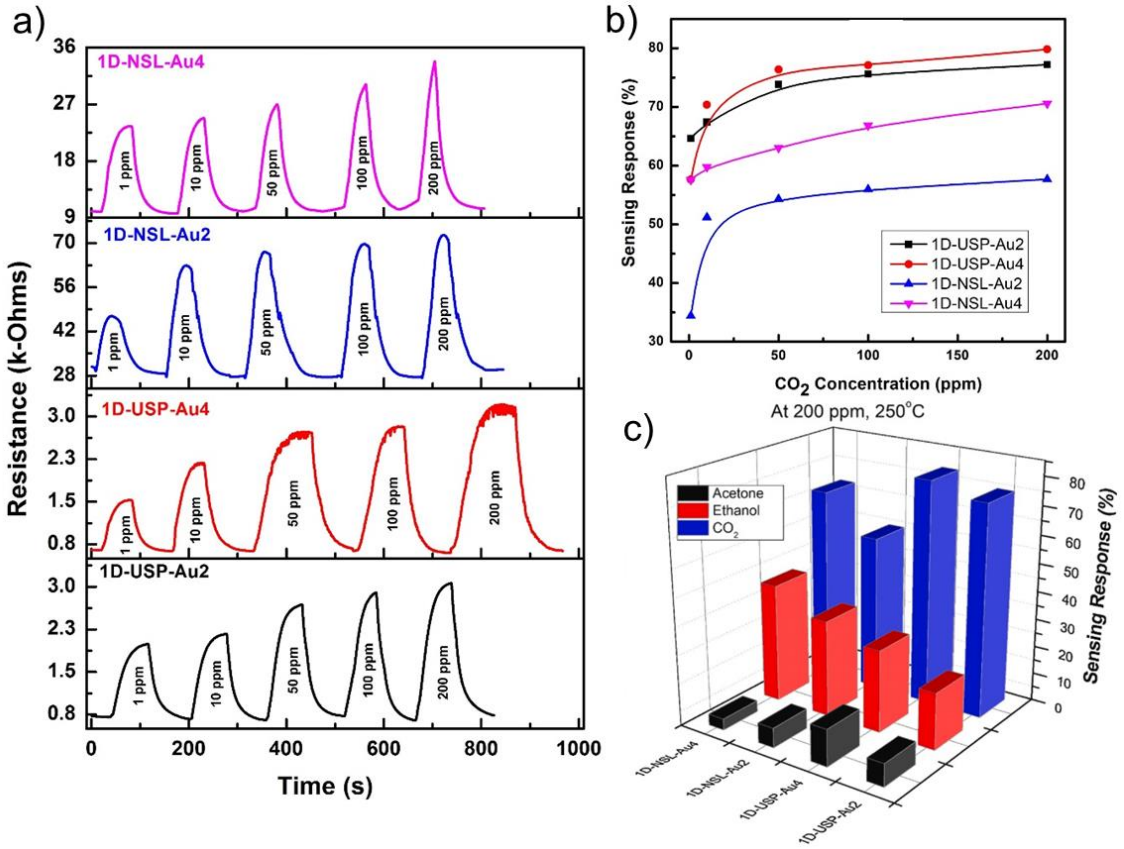

Figure 7-3. (a) Dynamic responses and (b) sensing response of 1DZnO materials to different CO_2 concentrations. (c) Response of ZnO platforms to various gases at a concentration of 200 ppm and 250ºC.

To determine the sensing performance towards different CO_2 concentrations (1, 10, 50, 100, 200 ppm), the dynamic resistance curves of the synthesized 1DZnO matrices were measured (Figure 7-3 (a)). These graphs showed an increase in the resistivity of all the samples when a CO_2 atmosphere was present. The increase in the resistivity of the material is due to the adsorption of the gas as CO_3^{2-} groups on the surface of the semiconductor[156]. In the graphs, a more significant increase in the electrical response of the material is also shown in proportion to the CO_2 concentration in the chamber. This is explained by the fact that the higher the concentration of the analyte, the greater the adsorption of the gas on the ZnO, and consequently, a greater change in the resistivity is produced[157]. In addition, it is also observed that the resistance of the 1DZnO materials differ from each other before CO_2 is introduced into the sensing chamber. Roughly, NSL samples exhibit higher base resistivity (28 KΩ) than those in which a seed layer is used for growth (USP: 0.8 KΩ). The interconnection between the nanostructures forming a denser and more homogeneous coating in the 1DZnO-USP samples may be responsible for the lower resistivity of the system (Figure 7-1 (a)). Contrarily, the 1DZnO-NSL samples could owe their

more resistive behavior to obtaining semiconductor arrays without interconnection and with lower homogeneity in growth (Figure 7-1 (b)). It was also observed that samples synthesized with 4 nm catalyst films presented lower resistivity than those with 2 nm Au for both USP and NSL. This is attributed to the conductive behavior of gold.

In the sensing response plots (Figure 7-3 (b)), a signal saturation process is observed in all samples as the CO_2 concentration rises. It has been reported that the availability of surface defects (i.e., oxygen vacancies) in ZnO is responsible for the preferential adsorption of oxidizing gases. Thus, as the available defects become saturated due to increasing gas concentration, it is also possible to observe a stagnation in the response signal[72].

The sensing curves also show that 1DZnO-USP coatings present a higher response than 1DZnO-NSL. This difference can be explained in terms of the morphological differences in the samples. On the one hand, it is possible to observe that the higher aspect ratio, density, and random orientation structures present in 1DZnO-USP result in higher surface area and platform conductivity. These characteristics thus favor CO_2 adsorption and improve the sensing response of the system. In contrast, the 1DZnO-NSL nanostructures presented lower surface area and conductivity, so their response would be expected to be reduced. It is also observed in Figure 7-3 (b) that, regardless of the use of buffer films in the growth, the obtained nanostructures show better performance as the amount of catalyst used was increased (Au 4nm). This may be due to the higher availability of sensing area in the matrix (morphological parameters) and surface defects confirmed by SEM and XPS.

Employing these dynamic resistance measurements, it was possible to determine the response and recovery times of the materials toward CO_2 detection. In this way, it was found that the 1DZnO-USP samples present longer response and recovery times than the 1DZnO-NSL ones. The lowest response time was 37 s for the 1DZnO-NSL material with 4 nm of Au. The difference may lie in the slower penetration of CO_2 molecules into coatings with a higher density of 1DZnO and, therefore a more gradual adsorption-desorption process[158]. It is also to be expected that an increase in gas-semiconductor interaction associated with more sensitive systems will lead to more extended response and recovery times[159].

Finally, the selectivity studies towards CO_2 of the obtained platforms are shown in Figure 7-3 (c). The sensitivities for other gases (acetone, ethanol) at a concentration of 200 ppm and an operating temperature of 250^{o}C are shown. All the materials studied show a high sensitivity for CO_2 compared to the other gases. Thus, the opposite behavior of the surface resistivity of ZnO for reducing gases (e.g., acetone, ethanol) is observed, making it an attractive platform for selective CO_2 detection.

Therefore, the present work describes a methodology by which it is possible to obtain 1DZnO nanomaterials in a controllable/reproducible way and with a possible integration to existing semiconductor technology for its implementation in the detection of reducing gases.

Chapter VIII Results: Optical biosensing

In this section, we report the synthesis of nanostructured ZnO arrays with controlled morphological features for their implementation in optical immunosensing platforms. The results show a morphological and structural dependence over the biofunctionalization strategy employed. Thus, the optimal morphology for anti- E. coli antibody binding on the semiconductor surface was determined, obtaining 100% immobilization efficiency using a low antibody concentration solution (30 mg/mL). The results presented here have been published in the Journal of Advanced Materials Interfaces (2023), doi.org/10.1002/admi.202300167 (IF: 6.389), with the title: Interaction Study of Anti‐E. coli Immobilization on 1DZnO at Nanoscale for Optical Biosensing Application[116].

Figure 8-1(a-f) shows SEM micrographs of the 1DZnO coatings employed for developing biosensing platforms. In this case, the samples were synthesized on silicon substrates (with and without the ZnO seed layer) and metalized with 4 nm of Au. The synthesis in all cases was carried out at a temperature of 950 ^{o}C and a pressure of 30 mbar (60 minutes), using a 1:1 mixture of ZnO:C powders as precursors. By controlling the flow rates employed, the position of the precursors (upstream or downstream configuration), and the preparation of the substrates, it was possible to vary the morphological properties as illustrated in Figure 8-1 (a-f). The obtained samples were then grouped into three different types of morphologies: 1DZnO_1, 1DZnO_2, and 1DZnO_3.

The coatings labeled as 1DZnO_1 (Figure 8-1 (a-b)) were obtained directly on Si substrates (without seed layer) and employing a flux (Ar/O_2) of 36 sccm in the upstream position. In these samples, it is possible to observe the simultaneous formation of 1DZnO (nanowires) and 2DZnO (nanowalls) on the substrate. In this case, the growth mechanism is a mixture of VLS and VSS processes. Even when using a substrate that has high crystalline incompatibility with the nanomaterial to be synthesized, it is observed that highly homogeneous coatings were obtained under the reported conditions. The nanostructures show a diameter of (136±11) nm and a length of (8.1±2.7) µm.

In the case of samples 1DZnO_2 and 1DZnO_3, ZnO sputtered silicon substrates (ZnO thin film of 200±10 nm thickness) in downstream positions were used with fluxes of 36 and 72 sccm, respectively. It is possible to observe that for lower flow conditions (1DZnO_2: Figure 8-1 (c-d)), nanostructures of (0.8±0.1) µm in length were obtained with a predominant vertical alignment. In this case, the pressure and flow rates employed allow a stable supply of the precursor species to the growth interface, thus obtaining a homogeneous coating. In contrast, with high flows (1DZnO_3: Figure 8-1 (e-f)), a higher growth rate is observed than in the previous cases, obtaining nanostructures with a length of (8.3±3.4) µm. Moreover, it is possible to perceive that some catalyst nanoparticles are supported by the seed layer and not by axial ZnO structures, suggesting an unstable supply to the growth interface. Figure 8-1 (g) shows the histograms of morphological features determined by SEM image analysis of the three types of samples studied. It is observed that regardless of the length of the nanostructures, the diameter is confined in all cases between 140-130 nm.

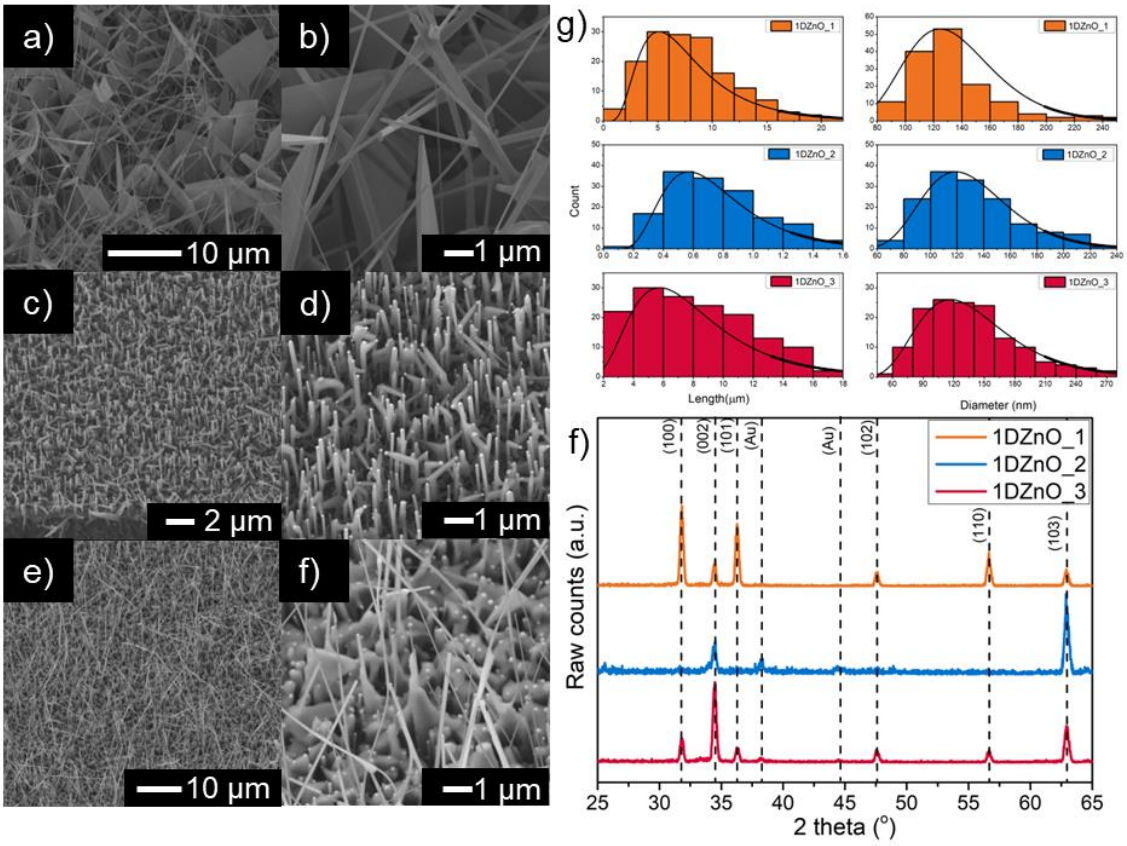

Figure 8-1. (a-f) SEM micrographs of one-dimensional ZnO nanostructures synthesized at 950ºC and 30 mbar. (a-b) 1DZnO_1 samples were obtained without the use of seed coatings in the upstream position (36 sccm Ar/O_2). Intercalation between 1DZnO structures and 2DZnO can be seen. (c-f) Samples synthesized with the use of seed layer in downstream position, (c-d) Morphology 1DZnO_2 (36 sccm Ar/O_2) composed of highly aligned nanostructures (e-f) Morphology 1DZnO_3 (72 sccm Ar/O_2) nanostructures with the high form factor. (g) Distributions of morphological parameters present in the synthesized materials. (f) GIXRD diffractograms of the studied ZnO nanostructured materials.

GIXRD measurements identified the wurtzite of ZnO and cubic Au phases (ZnO: ICSD-193696 and Au: ICSD-611625). For the sample where the presence of walls is observed (1DZnO), there is a polycrystalline behavior in the diffractogram, the peaks of greater intensity are associated with inclined planes to the support surface. The presence of these crystal orientations is associated with growth in random directions. On the other hand, for sample 1DZnO_2, the dominant plane (103) in the grazing angle configuration is associated with highly vertical-oriented growth[160]. Lastly, for sample 1DZnO_3, a polycrystalline behavior is observed in which the peak with the highest intensity is (002), which may be associated with the preferential orientation of the seed layer used for growth.

Subsequently, antibody immobilization tests were carried out on the surface of the nanostructured ZnO arrays. The process consisted of activating the ZnO samples with a KOH solution to react with the silanization agent (APTMS). On this ZnO/APTMS polymerized surface, the biorecognition agents (Anti- *E.coli*)

were attached. To monitor changes in the surface chemistry of the samples, FTIR measurements were performed at each of the biofunctionalization stages (Figure 8-2 (a-c)). For the 1DZnO_1 samples, the presence of wall-like structures results in counterproductive for the development of a bioselective layer since once the silanization process is carried out, the presence of siloxane (Si-O-Si) bonds is not observed. This suggests poor polymerization of the APTMS layer and limited immobilization of the recognition antibodies.

On the other hand, sample 1DZnO_2 (Figure 8-2 (b)) signals at 1062 and 1108 cm^{-1} associated with Si-O and Si-O-Si bonds, respectively, suggest a good coating of the APTMS layer. This observation is reinforced by the appearance of signals from amine (N-H: 1582 cm^{-1}) and methyl (C-H: 2851 & 2920 cm^{-1}) groups in the 1DZnO_2/APTMS samples[161,162]. The immobilization of the antibodies on the surface of the 1DZnO_2 semiconducting matrix was corroborated by signals at 1693 cm^{-1} (C=O) and 1536 cm^{-1}(N-H) of amide groups and disulfide signals (520 and 682 cm^{-1}) belonging to the immunoglobulins used[163,164].

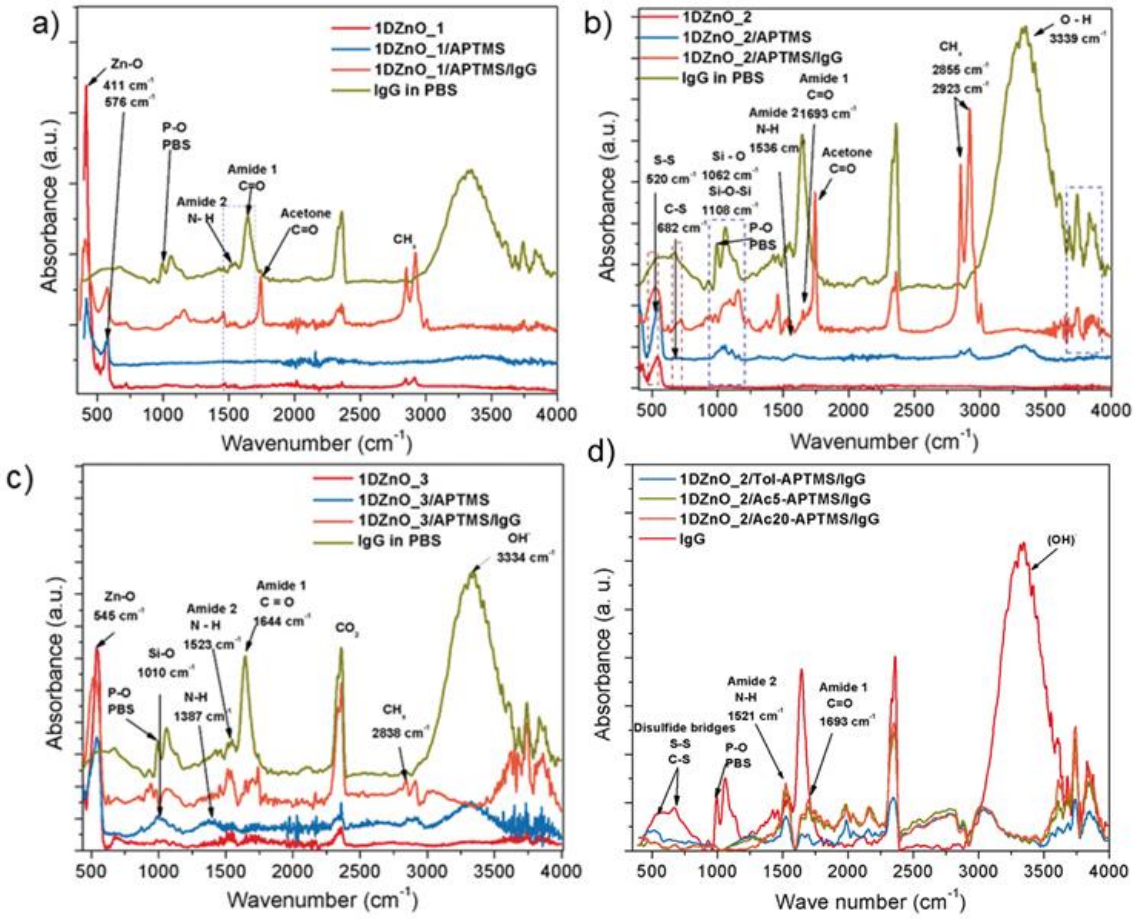

Figure 8-2. (a-c) FTIR spectroscopy measurements of the different 1DZnO morphologies synthesized to evaluate the biofunctionalization process: i) ZnO pristine surface ii) APTMS silanization iii) Anti- *E. coli* immobilization. (d) FTIR monitoring of optimized biofunctionalization methodology for 1DZnO_2 samples.

Figure 8-2 (c) shows the changes resulting from the functionalization of sample 1DZnO_3. The 1010 cm^{-1} signal is mainly related to the Si-O bond and weakly to

the Si-O-Si, so the number of functional groups for antibody anchoring is expected to be lower than for the 1DZnO_2 sample. The initial results determined that the 1DZnO_2 sample presents the best morphology for developing an inmunosensing bioselective layer.

Having determined this, the functionalization strategy was optimized by reducing hydroxylation and silanization reaction times (Table 4-2 depicts functionalization methodology details). Figure 8-2 (d) shows the results of the different functionalization strategies using acetone and toluene as solvents of the APTMS agent at different contact times: Ac5, Ac20, Tol (Acetone: 5 / 20 min, Toluene: 10 min). In these spectra, it is possible to observe signals of amide groups (C=O / N-H) and disulfide bridges that corroborate the presence of antibodies on the surface of the semiconducting material.

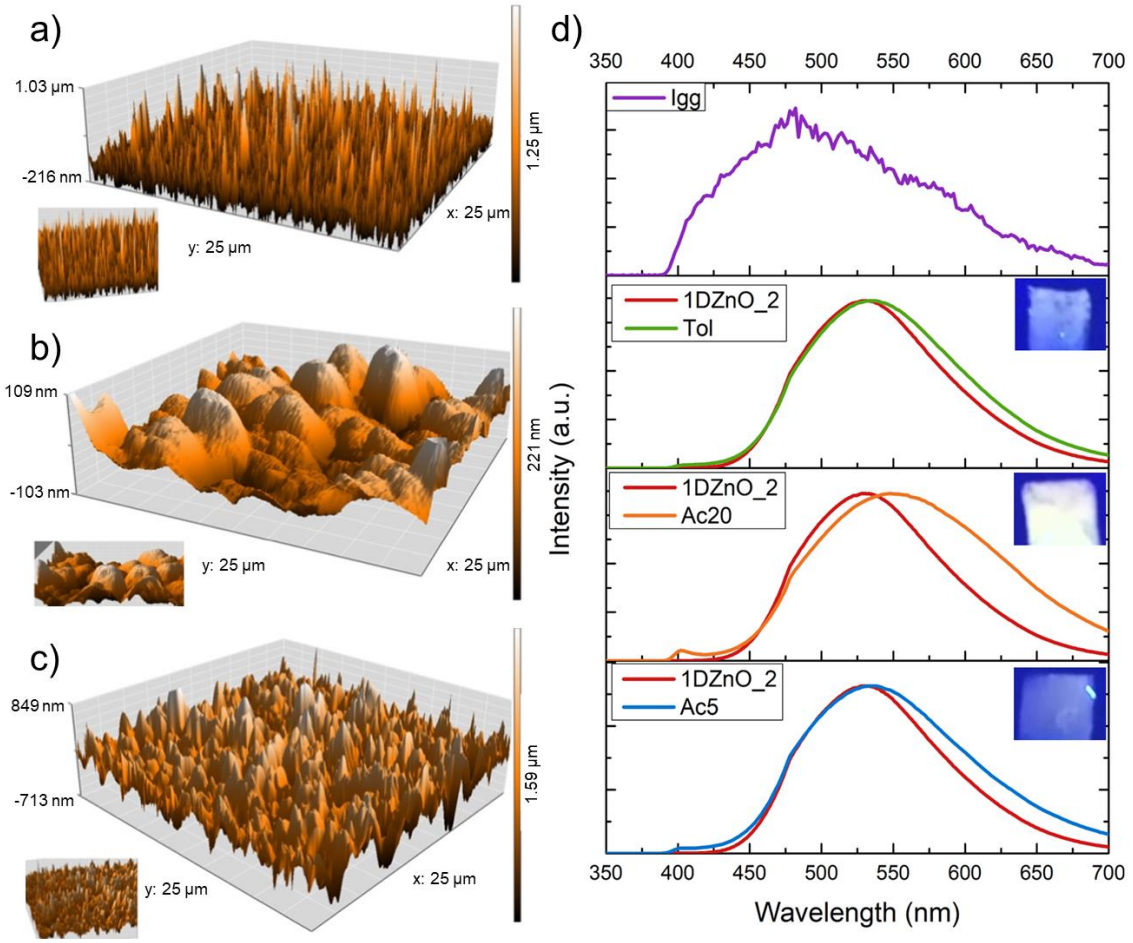

Figure 8-3. (a-c) AFM micrographs of the sensing platform at different stages of the functionalization process, (a) One-dimensional ZnO nanostructures (1DZnO_2) (b) Silanization: 1DZnO/APTMS (c) Immobilization of antibodies: 1DZnO_2/APTMS/IgG. (d) Photoluminescence response for IgG biofunctionalized platforms using different solvents and contact times.

Likewise, AFM measurements were performed at different stages of the biofunctionalization process to evaluate the changes in the topography of the sensing surface. As seen in Figure 8-3 (a-b), the average roughness of the system changes drastically with the APTMS coating of the 1DZnO resulting from

the polymerization of the silanizing agent to form islands. Subsequently, an increase in roughness was observed when antibodies were immobilized on the system's surface (Figure 8-3 (c)), thus corroborating the results of the biofunctionalization strategy employed.

To determine the optical transduction response of the platform, the photoluminescence signal of 1DZnO_2 samples was measured before and after antibody immobilization strategies (Ac5, Ac20, Tol). In Figure 8-3 (d), we observe a red shift of the emission of the material resulting from the functionalization with the bioselective coating. It has been previously reported that APTMS coating of ZnO surfaces causes defect migration in the semiconductor lattice, thus changing the emission of the material (Brauer et al.[114]). In addition to the signal shift, an enhancement of the DLE bandwidth is also observed, which could be linked with antibodies functionalization producing new energy levels.

At the same time, Figure 8-2 (c) insets portray the photographs of the functionalized substrate emissions when they are illuminated with a low-power UV lamp. With the naked eye, it is possible to appreciate a change in coloration from green color in 1DZnO samples without antibodies to a blue coloration after immobilization. The figure also shows the photoluminescence measurement of the antibody used (anti *E. coli*) supported on a silicon wafer.

The changes produced by the chemical alteration of the surface also generate a change in the signal of the NBE band (400 nm), where an increase of the signal is observed after igG immobilization. Processes such as hydroxylation could affect the availability of point defects on the semiconducting surface and therefore change the emission of the compound.

Notably, the results demonstrate that the development of a bioselective layer based on APTMS-IgG does not undermine the optical signal of the material and therefore allows the system obtained to be used for the optical detection of target analytes (*E. coli*) where a signal quenching in response to the monitored biointeraction is expected.

To corroborate the functionalization process of the 1DZnO materials, FIB equipment was used to prepare samples in which the APTMS coating of the structures could be appreciated. Figure 8-4 (a-e) shows the electron microscopy images where the axial surface of the semiconductor coated by a polymeric layer of APTMS is observed. It is important to note that the conditions used for the silanization process allow obtaining a homogeneous coating of the surface of the ZnO nanostructures and does not result only in the formation of a horizontal film covering the top of the system. This allows us to efficiently take advantage of the high surface area offered by the platform. Using the STEM-EDS technique, it was possible to carry out a compositional mapping of the ZnO/APTMS/IgG interface; the results are shown in Figure 8-4 (f-l). With these scans, it was possible to identify characteristic elements (S, P) of the amino acids that make up the immobilized antibodies on the entire surface of the 1DZnO. The presence of Si homogeneously on the material's surface is due to the APTMS agent used to develop the bioselective layer. These results show consistency with the signals monitored by FTIR and with the roughness results determined by AFM. Therefore, the results presented demonstrate that the methodology employed

allows for obtaining a biosensor layer in a homogeneous and reproducible manner on the surface of the nanostructured ZnO platform.

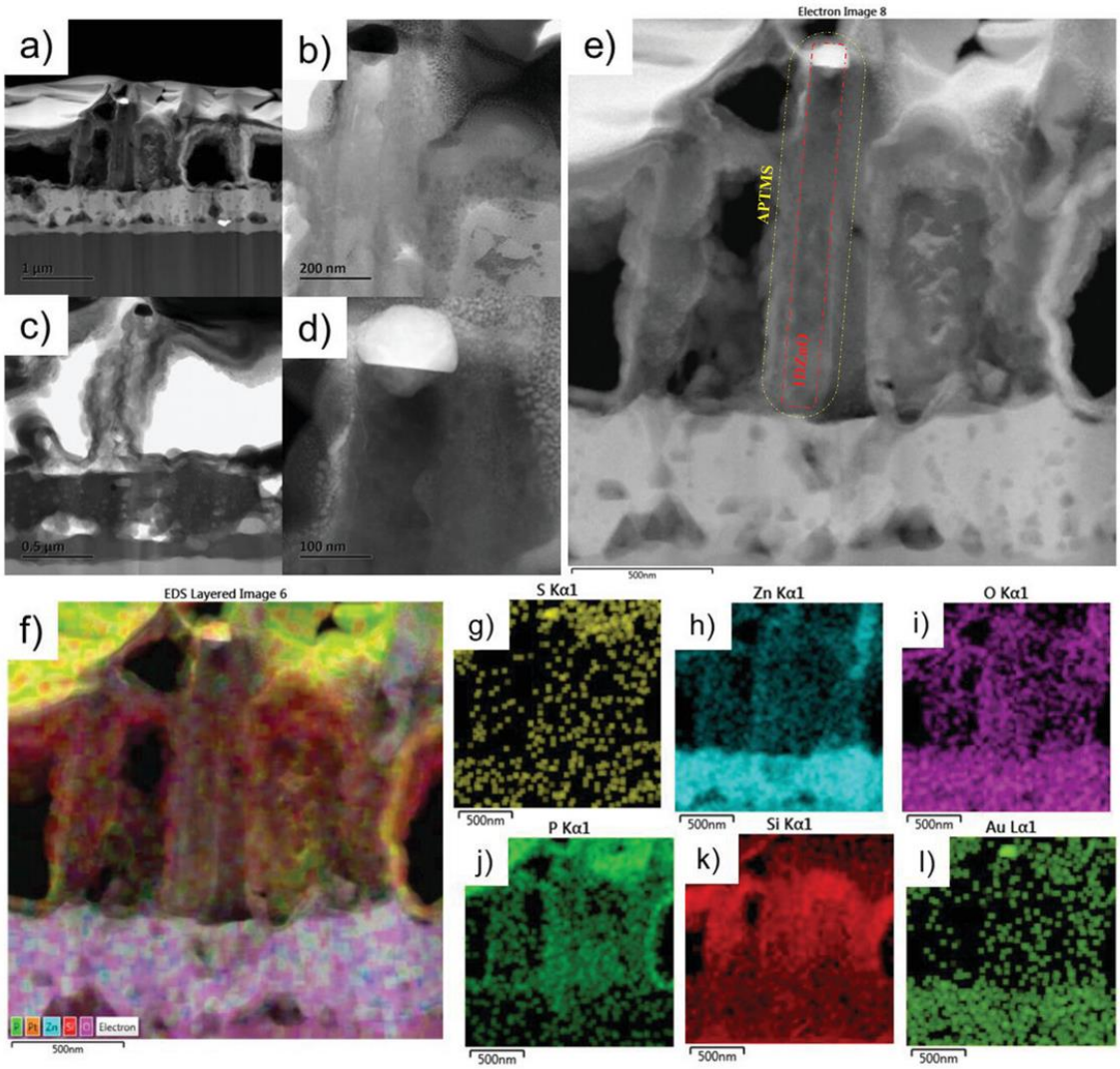

Figure 8-4. (a-e) Transmission electron microscopy images of one-dimensional ZnO nanostructures showing the APTMS/IgG biofunctionalization of the material surface. (f-l) EDS compositional mappings showing the distribution of characteristic elements of the different components of the bioselective layer.

Finally, a validation process was carried out to quantify the immobilization of the antibodies using the Bradford method. Utilizing a calibration curve, it was possible to correlate the UV absorbance with the protein concentration in a solution. Using an initial solution with a 30 µg/mL concentration of antibodies, washes of the 1DZnO_2/APTMS system (prepared with different solvents) were performed to determine the remnant concentration and thus calculate the immobilization efficiency of antibodies on the support. Table 8-1 shows the results obtained.

Through this process, it was possible to determine that the sample mwe1DZnO_2 treated with acetone for 5 minutes obtained the APTMS layer with the highest availability of functional groups for the immobilization of anti-*E. coli* antibodies. Thus, the current work presents a controllable and reproducible strategy to obtain

sensing surfaces on nanostructured ZnO platforms with optical features that justify their use in developing optical immunosensors for *E. coli*.

Table. 8-1 Quantification of antibody immobilization by Bradford method for 1DZnO_2/APTMS samples.

Functionalization treatment	Antibody concentration (μg/mL)				*Immobilization efficiency (%)
	Antibody stock	Wash 1	Wash 2	Wash 3	
Tol	1.2	N.D	N.D	N.D	96.0 (28.8 μg/mL)
Ac5	N.D	N.D	N.D	N.D	100.0 (30.0 μg/mL)
Ac20	14.2	N.D	N.D	N.D	52.7 (15.8 μg/mL)

* Calculated using a starting antibody stock concentration of 30 μg/ml. N.D: non detectable

Chapter IX Conclusions

Despite the large number of nanomaterials reported to date, the nanostructuring of any material, including ZnO, presents challenges in controlling the physical and chemical properties obtained due to low dimensionality effects. However, this is a fundamental requirement for archiving nanostructured materials integration into nanodevices.

Therefore, this work describes the physicochemical properties and tunability of one-dimensional nanostructured ZnO materials (1DZnO) obtained by a metal-assisted vapor phase growth. A series of conditions are reported by which it is possible to obtain homogeneous 1DZnO coatings on crystalline Si substrates, even without using seed layer buffer films. Moreover, parameters such as pressure, carrier flows, catalyst pattern, and precursors employed allow for precise control of the optical, structural, and morphological properties of the 1DZnO synthesized. In this regard, the necessity of an oxidizing atmosphere for the anisotropic crystallization of the materials was experimentally corroborated. Also, the role of pressure modulation on the ZnO materials growth was studied as better mobility of the gas precursors to the nucleation interface in response to the working pressure reduction was observed. This allows the obtention of high aspect 1DZnO even in upstream and high flow conditions. All the materials obtained showed intense visible emission attributed to point defects and diffraction signals attributed to a single crystal structure.

On the other hand, the results of photocatalysis tests showed hydrogen evolution for all the 1DZnO materials studied in the presence of a sacrificial agent and under broadband illumination. Samples with high aspect ratios and random orientation resulted in the best performance and stability for the photocatalytic water splitting reaction. The increase in the system's surface area and light-trapping properties stand out among the proposed enhancement mechanisms with respect to the powdered material. In addition, the simultaneous obtaining of AuNPs at the tip of the ZnO matrix produced by the catalyst-assisted growth offers an advantage for obtaining plasmonic-based photocatalysts.

In the case of gas sensing, 1DZnO platforms with different aspect ratios (NWs/NRs) were implemented in a chemo-resistive CO_2 sensing coating. The characterization performed by XPS and PL showed a deviation from the stoichiometry of the synthesized ZnO nanostructures. The gas detection study showed that 1DZnO with higher aspect ratios (NWs) exhibited a sensitivity of ~80 %, while those with lower aspect ratios (NRs) presented faster response times ~37 s. Thus, it was proved that the obtained materials could perform as sensitive and selective transducers to the presence of oxidizing gases such as CO_2. Also, since the NRs samples were obtained directly on Si substrates, the methodology reported in this section significantly reduces the time and cost of the fabrication process.

Finally, a functionalization strategy for obtaining bioselective layer for *E. coli* on the surface of 1DZnO was developed. FTIR, AFM, STEM, and PL results demonstrated a correct silanization of the semiconductor with APMTS agent as well as the efficient immobilization of Anti- *E. coli* antibodies on its surface.

Through these characterization techniques, it was possible to elucidate the functionalization mechanism and the chemical modification of the nanostructured surface. This could result in the improvement of optical immunosensors based on PL response. The reported methodology demonstrated 100% immobilization efficiency using a 30 µg/ml solution of antibodies. With all this in mind, the results presented can be here can contribute to the progress of controllable semiconductor nanodevices to tackle the environmental, energy, and health problems relevant today.

Published articles

1. **Galdámez-Martínez A**, Bai Y, Santana G, Sprick RS, Dutt A. Photocatalytic hydrogen production performance of 1-D ZnO nanostructures: Role of structural properties. Int J Hydrogen Energy. 2020; 45:1-10. doi:10.1016/j.ijhydene.2020.08.247
2. Ortiz-Casas B*, **Galdámez-Martínez A***, Gutiérrez-Flores J*, et al. Bio-acceptable 0D and 1D ZnO nanostructures for cancer diagnostics and treatment. Mater Today. 2021; 50(November):533-569. doi:10.1016/j.mattod.2021.07.025
3. Jain M, **Galdamez-Martinez A**, Dutt A, Matsumoto Y. Photoluminescence properties of SiOxCy-films deposited under argon atmosphere and Si-based organometallic precursor by O-Cat-CVD. CCE 2021 - 2021 18th Int Conf Electr Eng Comput Sci Autom Control. 2021;(Nicolet 560):12-15. doi:10.1109/CCE53527.2021.9633067
4. Jaime EA, Tolibia SM, Rodelo CG, Salinas RA, **Galdámez-Martínez A**, Dutt A. Interaction of virus-like particles and nanoparticles with inorganic materials for biosensing: An exciting approach. Mater Lett. 2022;307(August 2021):1-5. doi:10.1016/j.matlet.2021.131088
5. Gutiérrez Rodelo C*, Salinas RA*, Armenta Jaime E*, **Galdámez-Martínez A*,** et al. Zinc associated nanomaterials and their intervention in emerging respiratory viruses: Journey to the field of biomedicine and biomaterials. Coord Chem Rev. 2022;457(xxxx):214402. doi:10.1016/j.ccr.2021.214402
6. Malagón G JF, Salinas RA, **Galdámez A**, Orduña-Díaz A, Dutt A. Functionalization of 3-aminopropyltrimethoxysilane Self-Assembled Monolayers on ZnO/Au nanowires: Role of the Seed layer. Mater Lett. 2021;290:129452. doi:10.1016/j.matlet.2021.129452
7. **Galdamez A**, Serrano A, Santana G, et al. DNA probe functionalization on different morphologies of ZnO/Au nanowire for bio-sensing applications. Mater Lett. 2019;235:250-253. doi:10.1016/j.matlet.2018.10.026
8. Serrano A, Arana A, **Galdámez A**, et al. Effect of the seed layer on the growth and orientation of the ZnO nanowires: Consequence on structural and optical properties. Vacuum. 2017;146:509-516. doi:10.1016/j.vacuum.2017.03.010
9. **Galdámez-Martínez A***, Dutt A*, Jain M, et al. Decay emission study of ZnO nanostructures obtained by low-pressure vapor transport technique. Appl Surf Sci Adv. 2022;12(September):100334. doi:10.1016/j.apsadv.2022.100334
10. **Galdámez-Martinez A**, Santana G, Güell F, Martínez-Alanis PR, Dutt A. Photoluminescence of zno nanowires: A review. Nanomaterials. 2020;10(5):857. doi:10.3390/nano10050857
11. González-Garnica M*, **Galdámez-Martínez A***, Malagón F, et al. One dimensional Au-ZnO hybrid nanostructures based CO_2 detection: Growth mechanism and role of the seed layer on sensing performance. Sensors Actuators B Chem. 2021;337(January):129765. doi:10.1016/j.snb.2021.129765

12. Salinas R A*, **Galdámez-Martínez A*,** Tolibia S E M, Garduño C, Ramos C, Santana G, Orduña A and Dutt A. Interaction Study of Anti- E. coli Immobilization on 1DZnO at Nanoscale for Optical Biosensing Application Adv. Mater. Interfaces, 2023. doi.org/10.1002/admi.202300167

*Equal contribution

Bibliography

1. Sustainable Development Goals | UNDP. https://www.undp.org/content/undp/en/home/sustainable-development-goals.html.
2. Jiang, J., Pi, J. & Cai, J. The Advancing of Zinc Oxide Nanoparticles for Biomedical Applications. *Bioinorg. Chem. Appl.* **2018**, (2018).
3. Guayaquil-sosa, J. F. Photocatalytic Hydrogen Production using a Mesoporous TiO2 Doped with Pt : Semiconductor Synthesis , Oxidation-Reduction Network and Quantum Efficiencies . (2018).
4. Zhang, K. & Guo, L. Metal sulphide semiconductors for photocatalytic hydrogen production. *Catal. Sci. Technol.* **3**, 1672–1690 (2013).
5. Rokade, A. *et al.* Electrochemical synthesis of 1D ZnO nanoarchitectures and their role in efficient photoelectrochemical splitting of water. *J. Solid State Electrochem.* **21**, 2639–2648 (2017).
6. Sahu, D. R., Liu, C. P., Wang, R. C., Kuo, C. L. & Huang, J. L. Growth and application of ZnO nanostructures. *Int. J. Appl. Ceram. Technol.* **10**, 814–838 (2013).
7. Willander, M. *et al.* Zinc oxide nanorod based photonic devices: Recent progress in growth, lightemitting diodes and lasers. *Nanotechnology* **20**, (2009).
8. Govatsi, K., Seferlis, A., Neophytides, S. G. & Yannopoulos, S. N. Influence of the morphology of ZnO nanowires on the photoelectrochemical water splitting efficiency. *Int. J. Hydrogen Energy* **43**, 4866–4879 (2018).
9. Tereshchenko, A. *et al.* Optical biosensors based on ZnO nanostructures: Advantages and perspectives. A review. *Sensors and Actuators B-Chemical* **229**, 664–677 (2016).
10. Kang, Z. *et al.* Enhanced photoelectrochemical property of ZnO nanorods array synthesized on reduced graphene oxide for self-powered biosensing application. *Biosens. Bioelectron.* **64**, 499–504 (2014).
11. Niepelt, R. *et al.* Biofunctionalization of zinc oxide nanowires for DNA sensory applications. *Nanoscale Res. Lett.* **6**, 511 (2011).
12. Viter, R. *et al.* The influence of localized plasmons on the optical properties of Au/ZnO nanostructures. *J. Mater. Chem. C* **3**, 6815–6821 (2015).
13. Espitia, P. J. P., Otoni, C. G. & Soares, N. F. F. *Zinc Oxide Nanoparticles for Food Packaging Applications*. *Antimicrobial Food Packaging* (Elsevier Inc., 2016). doi:10.1016/B978-0-12-800723-5.00034-6.
14. Antrekowitsch, J. *et al.* Zinc and Residue Recycling. *Handb. Recycl. State-of-the-art Pract. Anal. Sci.* 113–124 (2014) doi:10.1016/B978-0-12-396459-5.00009-X.
15. Morkoç, H. & Özgür, Ü. *Zinc Oxide: Fundamentals, Materials and Device Technology*. *Zinc Oxide: Fundamentals, Materials and Device Technology* (2009). doi:10.1002/9783527623945.
16. Chennupati Jagadish, S. J. P. *Zinc Oxide Bulk, Thin Films and Nanostructures: Processing, Properties, and Applications*. (Elsevier Science, 2006).
17. Butcher, P. N., March, N. H. & Tosi, M. P. *Crystalline semiconducting materials and devices*. (Springer, 1986).
18. Dulub, O., Boatner, L. A. & Diebold, U. STM study of the geometric and electronic structure of ZnO(0 0 0 1)-Zn, (0 0 0 $\bar{1}$)-O, (1 0 $\bar{1}$ 0), and (1 1 $\bar{2}$ 0) surfaces. *Surf. Sci.* **519**, 201–217 (2002).
19. Noman, M. T., Amor, N. & Petru, M. Synthesis and applications of ZnO nanostructures (ZONSs): a review. *Crit. Rev. Solid State Mater. Sci.* **47**, 99–141 (2022).
20. Beitollahi, H., Tajik, S., Garkani Nejad, F. & Safaei, M. Recent advances in ZnO nanostructure-based electrochemical sensors and biosensors. *J. Mater. Chem. B* **8**, 5826–5844 (2020).
21. Mukhtar, A., Wu, K., Cao, X. & Gu, L. Magnetic nanowires in biomedical applications. *Nanotechnology* **31**, 433001 (2020).
22. Clarivative. Web of Science Query: 1DZnO nanostructures. https://www.webofscience.com/wos/woscc/summary/11724ba8-37b2-4660-bec3-c56a7a035201-8543860d/times-cited-descending/1 (2023).
23. Ditshego, N. M. J. Zno nanowire field effect transistor for biosensing: A review. *J. Nano*

Res. **60**, 94–112 (2019).

24. Rong, P., Ren, S. & Yu, Q. Fabrications and Applications of ZnO Nanomaterials in Flexible Functional Devices-A Review. *Crit. Rev. Anal. Chem.* **49**, 336–349 (2019).
25. Wahab, R. *et al.* Zinc Oxide Nanostructures and their Applications. *Intell. Nanomater. Process. Prop. Appl.* **28**, 183–212 (2012).
26. Ortiz-Casas, B. *et al.* Bio-acceptable 0D and 1D ZnO nanostructures for cancer diagnostics and treatment. *Mater. Today* **50**, 533–569 (2021).
27. Prete, P., Lovergine, N. & Tapfer, L. Nanostructure size evolution during Au-catalysed growth by carbo-thermal evaporation of well-aligned ZnO nanowires on (100)Si. *Appl. Phys. A Mater. Sci. Process.* **88**, 21–26 (2007).
28. Suh, D.-I., Byeon, C. C. & Lee, C.-L. Synthesis and optical characterization of vertically grown ZnO nanowires in high crystallinity through vapor-liquid-solid growth mechanism. *Appl. Surf. Sci.* **257**, 1454–1456 (2010).
29. Güniat, L., Caroff, P. & Fontcuberta I Morral, A. Vapor Phase Growth of Semiconductor Nanowires: Key Developments and Open Questions. *Chem. Rev.* **119**, 8958–8971 (2019).
30. Li, X., Ni, J. & Zhang, R. A Thermodynamic Model of Diameter- and Temperature-dependent Semiconductor Nanowire Growth. *Sci. Rep.* **7**, 1–8 (2017).
31. Bhat, S., Shrisha, B. V. & Naik, K. G. Au catalyst assisted growth of ZnO nanowires by vapour phase transport method on p-Si and fabrication of p-Si/n-ZnO heterojunction diode. *AIP Conf. Proc.* **1665**, 10–13 (2015).
32. Menzel, A. *et al.* Tuning the growth mechanism of ZnO nanowires by controlled carrier and reaction gas modulation in thermal CVD. *J. Phys. Chem. Lett.* **3**, 2815–2821 (2012).
33. Wang, Z. L. Zinc oxide nanostructures: Growth, properties and applications. *J. Phys. Condens. Matter* **16**, R829–R858 (2004).
34. Huang, M. H. *et al.* Room-temperature ultraviolet nanowire nanolasers. *Science* **292**, 1897–9 (2001).
35. Kong, X., Wei, C., Zhu, Y., Cohen, P. & Dong, J. Modeling of Catalyst-free Growth Process of ZnO Nanowires. *Procedia Manuf.* **26**, 349–358 (2018).
36. Bahramian, R., Moshaii, A. & Eshghi, H. Effect of seeding modification of substrate on the growth and UV detection properties of ZnO nanowires. *Mater. Lett.* **179**, 222–225 (2016).
37. Güell, F. *et al.* Raman and photoluminescence properties of ZnO nanowires grown by a catalyst-free vapor-transport process using ZnO nanoparticle seeds. *Phys. Status Solidi Basic Res.* **253**, 883–888 (2016).
38. Du, C. Y. *et al.* Facile synthesis of Z-scheme ZnO/Ag/Ag3PO4 composite photocatalysts with enhanced performance for the degradation of ciprofloxacin. *Mater. Chem. Phys.* **260**, (2021).
39. Choudhary, M. K., Kataria, J., Bhardwaj, V. K. & Sharma, S. Green biomimetic preparation of efficient Ag-ZnO heterojunctions with excellent photocatalytic performance under solar light irradiation: a novel biogenic-deposition-precipitation approach. *Nanoscale Adv.* **1**, 1035–1044 (2019).
40. Tan, W. K. *et al.* Facile Fabrication of Plasmonic Enhanced Noble-Metal-Decorated ZnO Nanowire Arrays for Dye-Sensitized Solar Cells. *J. Nanosci. Nanotechnol.* **20**, 359–366 (2019).
41. Zhang, L. *et al.* CdS/ZnO: A Multipronged Approach for Efficient Reduction of Carbon Dioxide under Visible Light Irradiation. *ACS Sustain. Chem. Eng.* (2020) doi:10.1021/acssuschemeng.0c00190.
42. Liu, Y. J. *et al.* Self-assembled ZnO/Ag hollow spheres for effective photocatalysis and bacteriostasis. *Mater. Res. Bull.* **98**, 64–69 (2018).
43. Sohrabnezhad, S. & Taghaddosnezhad, S. Incorporation of ZnO-Al layered double oxide in AgMCM-41 nanocomposite for photodegradation of dye. *Appl. Clay Sci.* **157**, 130–138 (2018).
44. Yao, C. *et al.* Au-Decorated ZnO Nanorod Powder and Its Application in Photodegradation of Organic Pollutants in the Visible Region. *Phys. status solidi* **218**, 2000737 (2021).
45. Zhang, Y., Zhou, J. B., Li, Z. & Feng, Q. Q. Photodegradation pathway of rhodamine B with novel Au nanorods @ ZnO microspheres driven by visible light irradiation. *J. Mater. Sci.* **53**, 3149–3162 (2018).

46. Fujishima, A. & Honda, K. Electrochemical Photolysis of Water at a Semiconductor Electrode. *Nature* **240**, 226–229 (1972).
47. Ramirez-Canon, A., Medina-Llamas, M., Vezzoli, M. & Mattia, D. Multiscale design of ZnO nanostructured photocatalysts. *Phys. Chem. Chem. Phys.* **20**, 6648–6656 (2018).
48. Ghasaban, S., Atai, M. & Imani, M. Simple mass production of zinc oxide nanostructures via low-temperature hydrothermal synthesis. *Mater. Res. Express* **4**, (2017).
49. OurWorldinData. Electricity generation from fossil fuels. https://ourworldindata.org/ (2023).
50. Fan, W., Zhang, Q. & Wang, Y. Semiconductor-based nanocomposites for photocatalytic H2 production and CO2 conversion. *Phys. Chem. Chem. Phys.* **15**, 2632–2649 (2013).
51. Alomair, N. A. & Mohamed, H. H. Single step green synthesis of Au/ZnO/rGO nanocomposites for visible light photocatalytic application. *Mater. Res. Express* **6**, (2019).
52. Wang, Z. *et al.* Progress on extending the light absorption spectra of photocatalysts. *Phys. Chem. Chem. Phys.* **16**, 2758–2774 (2014).
53. Chiarello, G. L., Dozzi, M. V. & Selli, E. TiO2-based materials for photocatalytic hydrogen production. *J. Energy Chem.* **26**, 250–258 (2017).
54. Seo, Y. S. & Oh, S. G. Controlling the recombination of electron-hole pairs by changing the shape of ZnO nanorods via sol-gel method using water and their enhanced photocatalytic properties. *Korean J. Chem. Eng.* **36**, 2118–2124 (2019).
55. Pirhashemi, M., Habibi-Yangjeh, A. & Rahim Pouran, S. Review on the criteria anticipated for the fabrication of highly efficient ZnO-based visible-light-driven photocatalysts. *J. Ind. Eng. Chem.* **62**, 1–25 (2018).
56. Chen, X., Shen, S., Guo, L. & Mao, S. S. Semiconductor-based {Photocatalytic} {Hydrogen} {Generation}. *Chem. Rev.* **110**, 6503–6570 (2010).
57. Samadi, M., Zirak, M., Naseri, A., Khorashadizade, E. & Moshfegh, A. Z. Recent progress on doped ZnO nanostructures for visible-light photocatalysis. *Thin Solid Films* **605**, 2–19 (2016).
58. Yang, P. Y. P. Semiconductor nanowires for energy conversion. *Nanoelectron. Conf. (INEC), 2010 3rd Int.* 527–546 (2010) doi:10.1109/INEC.2010.5424441.
59. Ameta, R. & Ameta, S. *Photocatalysis: principles and applications*. (CRC Press, 2017).
60. Guo, S., Li, X., Zhu, J., Tong, T. & Wei, B. Au NPs@MoS2 Sub-Micrometer Sphere-ZnO Nanorod Hybrid Structures for Efficient Photocatalytic Hydrogen Evolution with Excellent Stability. *Small* **12**, 5692–5701 (2016).
61. Awazu, K. *et al.* A plasmonic photocatalyst consisting of silver nanoparticles embedded in titanium dioxide. *J. Am. Chem. Soc.* **130**, 1676–1680 (2008).
62. Liu, E. *et al.* Plasmonic Ag deposited TiO 2 nano-sheet film for enhanced photocatalytic hydrogen production by water splitting. *Nanotechnology* **25**, (2014).
63. Shi, Y. *et al.* Hot Electron of Au Nanorods Activates the Electrocatalysis of Hydrogen Evolution on MoS<inf>2</inf> Nanosheets. *J. Am. Chem. Soc.* **137**, 7365–7370 (2015).
64. Piecyk, M. I. & McKinnon, A. C. Forecasting the carbon footprint of road freight transport in 2020. *Int. J. Prod. Econ.* **128**, 31–42 (2010).
65. Kampa, M. & Castanas, E. Human health effects of air pollution. *Environ. Pollut.* **151**, 362–367 (2008).
66. Manisalidis, I., Stavropoulou, E., Stavropoulos, A. & Bezirtzoglou, E. Environmental and Health Impacts of Air Pollution: A Review. *Front. Public Heal.* **8**, (2020).
67. Yadav, V. K. S., Daniel, T. T. & Paily, R. P. Gas Sensors Based on Drop-Casted ZnO Nanowires and Micro-Cantilever Printed Ag Contacts. *IEEE Sens. J.* **20**, 4951–4958 (2020).
68. Dan, Y., Evoy, S. & Johnson, A. T. C. Chemical Gas Sensors Based On Nanowires. *Sensors (Peterborough, NH)* **1**, 1–33 (2008).
69. Eranna, G. *Gas Sensing Devices Metal Oxide*. (2012).
70. Karthik, T. V. K., Martinez, L. & Agarwal, V. Porous silicon ZnO/SnO2 structures for CO2 detection. *J. Alloys Compd.* **731**, 853–863 (2018).
71. Seiyama, T., Fujiishi, K., Nagatani, M. & Kato, A. A New Detector for Gaseous Components Using Zinc Oxide Thin Films. *J. Soc. Chem. Ind. Japan* **66**, 652–655 (1963).
72. Karthik, T. V. K. *et al.* Sprayed ZnO thin films for gas sensing: effect of substrate temperature, molarity and precursor solution. *J. Mater. Sci. Mater. Electron.* **31**, 7470–

7480 (2020).
73. Van Hieu, N. *et al.* Comparative study on CO2 and CO sensing performance of LaOCl-coated ZnO nanowires. *J. Hazard. Mater.* **244**–**245**, 209–216 (2013).
74. Maarouf, M. & Al-Sunaidi, A. Investigating the chemisorption of CO and CO2 on Al- and Cu-doped ZnO nanowires by density-functional calculations. *Comput. Theor. Chem.* **1175**, 112728 (2020).
75. Srivastava, M. & Srivastava, A. Electron transport in CO2 adsorbed ZnO nanowire: DFT study. *Chem. Phys. Lett.* **729**, 17–23 (2019).
76. Jeongseok, L. *et al.* Improved sensitivity of α-Fe2O3 nanoparticle-decorated ZnO nanowire gas sensor for CO. *Sensors (Switzerland)* **19**, (2019).
77. An, G. *et al.* CO 2-mediated synthesis of ZnO nanorods and their application in sensing ethanol vapor. *J. Nanosci. Nanotechnol.* **11**, 1252–1258 (2011).
78. Kumar, M., Bhati, V. S., Ranwa, S., Singh, J. & Kumar, M. Pd/ZnO nanorods based sensor for highly selective detection of extremely low concentration hydrogen. *Sci. Rep.* **7**, 1–9 (2017).
79. Çolak, H. & Karaköse, E. Synthesis and characterization of different dopant (Ge, Nd, W)-doped ZnO nanorods and their CO2 gas sensing applications. *Sensors Actuators, B Chem.* **296**, 126629 (2019).
80. Tiwale, N. Zinc oxide nanowire gas sensors: Fabrication, functionalisation and devices. *Mater. Sci. Technol. (United Kingdom)* **31**, 1681–1697 (2015).
81. Guo, J. *et al.* High-performance gas sensor based on ZnO nanowires functionalized by Au nanoparticles. *Sensors Actuators, B Chem.* **199**, 339–345 (2014).
82. Consonni, V., Briscoe, J., Kärber, E., Li, X. & Cossuet, T. ZnO nanowires for solar cells: A comprehensive review. *Nanotechnology* **30**, (2019).
83. Al-Hashem, M., Akbar, S. & Morris, P. Role of Oxygen Vacancies in Nanostructured Metal-Oxide Gas Sensors: A Review. *Sensors Actuators, B Chem.* **301**, 126845 (2019).
84. Choi, S. W. & Kim, S. S. Room temperature CO sensing of selectively grown networked ZnO nanowires by Pd nanodot functionalization. *Sensors Actuators, B Chem.* **168**, 8–13 (2012).
85. Tang, Z. *et al.* Insights from nanotechnology in COVID-19 treatment. *Nano Today* **36**, 101019 (2021).
86. Gutiérrez Rodelo, C. *et al.* Zinc associated nanomaterials and their intervention in emerging respiratory viruses: Journey to the field of biomedicine and biomaterials. *Coord. Chem. Rev.* **457**, 214402 (2022).
87. Purwidyantri, A. *et al.* Speckled ZnO Nanograss Electrochemical Sensor for Staphylococcus epidermidis Detection. *J. Electrochem. Soc.* **164**, B205–B211 (2017).
88. Naresh, V. & Lee, N. A review on biosensors and recent development of nanostructured materials-enabled biosensors. *Sensors (Switzerland)* **21**, 1–35 (2021).
89. Dong, X. X. *et al.* Photoelectrochemical response to glutathione in Au-decorated ZnO nanorod array. *J. Mater. Chem. C* **7**, 5624–5629 (2019).
90. Han, Z., Luo, M., Chen, L., Chen, J. & Li, C. A photoelectrochemical immunosensor for detection of α-fetoprotein based on Au-ZnO flower-rod heterostructures. *Appl. Surf. Sci.* **402**, 429–435 (2017).
91. Hao, N. J. *et al.* Acoustofluidics-Assisted Fluorescence-SERS Bimodal Biosensors. *Small* **16**, (2020).
92. Malhotra, B. D. & Ali, M. A. Nanomaterials in Biosensors. in *Nanomaterials for Biosensors* vol. 2507 1–74 (Elsevier, 2018).
93. Mei, G. S. *et al. Robust Design of Bimetallic ZnO Nanofilm SPR Sensor using Taguchi Method*. *2020 Ieee Electron Devices Technology and Manufacturing Conference* (2020).
94. Mudgal, N., Saharia, A., Agarwal, A. & Singh, G. ZnO and Bi-metallic (Ag–Au) Layers Based Surface Plasmon Resonance (SPR) Biosensor with BaTiO3 and Graphene for Biosensing Applications. *IETE J. Res.* (2020) doi:10.1080/03772063.2020.1844074.
95. Khansili, N., Rattu, G. & Krishna, P. M. Label-free optical biosensors for food and biological sensor applications. *Sensors and Actuators B-Chemical* **265**, 35–49 (2018).
96. Jing, C. J. *et al.* ZnO micron rods as single dielectric resonator for optical sensing. *Anal. Chim. Acta* **1109**, 107–113 (2020).

97. Soo, S. K. *et al.* Effect of metal/metal oxide coupling on the photoluminescence properties of ZnO microrods. *Appl. Phys. a-Materials Sci. Process.* **124**, (2018).
98. Zhang, Q. X. *et al.* Photoelectrochemical thrombin biosensor based on perylene-3,4,9,10-tetracarboxylic acid and Au co-functionalized ZnO nanorods with signal-off quenching effect of Ag@Ag2S. *Analyst* **146**, 855–863 (2021).
99. Kim, J., Campbell, A. S., de Ávila, B. E. F. & Wang, J. Wearable biosensors for healthcare monitoring. *Nat. Biotechnol.* **37**, 389–406 (2019).
100. Samson, R., Navale, G. R. & Dharne, M. S. Biosensors: frontiers in rapid detection of COVID-19. *3 Biotech* **10**, 1–9 (2020).
101. Muhsin, S. A. *et al.* A microfluidic biosensor for rapid simultaneous detection of waterborne pathogens. *Biosens. Bioelectron.* **203**, 113993 (2022).
102. Huang, F. *et al.* An Acid-Responsive Microfluidic Salmonella Biosensor Using Curcumin as Signal Reporter and ZnO-Capped Mesoporous Silica Nanoparticles for Signal Amplification. *Sensors Actuators, B Chem.* **312**, 127958 (2020).
103. Vasudevan, S., Srinivasan, P., Rayappan, J. B. B. & Solomon, A. P. A photoluminescence biosensor for the detection ofN-acyl homoserine lactone using cysteamine functionalized ZnO nanoparticles for the early diagnosis of urinary tract infections. *J. Mater. Chem. B* **8**, 4228–4236 (2020).
104. Molavi, S., Bozorg, A. & Abdi, Y. ZnO Nanorod-Based Solution-Gated Devices for Antibody-Free Rapid Detection of Bacteria. *ACS Appl. Nano Mater.* **4**, 13486–13494 (2021).
105. Li, G. *et al.* Early stage detection of Staphylococcus epidermidis biofilm formation using MgZnO dual-gate TFT biosensor. *Biosens. Bioelectron.* **151**, 111993 (2020).
106. Chakraborty, B., Mandal, N., Das, N., Samanta, N. & Roychaudhuri, C. Competitive Impedance Spectroscopy in a Schottky-Contacted ZnO Nanorod Structure for Ultrasensitive and Specific Biosensing in a Physiological Analyte. *ACS Sensors* **7**, 1634–1647 (2022).
107. Salinas Domínguez, R. A., Domínguez Jiménez, M. Á. & Orduña Díaz, A. Antibody immobilization in zinc oxide thin films as an easy-handle strategy for Escherichia coli detection. *ACS Omega* **5**, 20473–20480 (2020).
108. Makaraviciute, A. & Ramanaviciene, A. Site-directed antibody immobilization techniques for immunosensors. *Biosens. Bioelectron.* **50**, 460–471 (2013).
109. Han, J. H., Lee, D., Chew, C. H. C., Kim, T. & Pak, J. J. A multi-virus detectable microfluidic electrochemical immunosensor for simultaneous detection of H1N1, H5N1, and H7N9 virus using ZnO nanorods for sensitivity enhancement. *Sensors Actuators, B Chem.* **228**, 36–42 (2016).
110. Nguyen, T. H. P. *et al.* Stable Electrochemical Measurements of Platinum Screen-Printed Electrodes Modified with Vertical ZnO Nanorods for Bacterial Detection. *J. Nanomater.* **2019**, (2019).
111. Jakša, G., Štefane, B. & Kovač, J. Influence of different solvents on the morphology of APTMS-modified silicon surfaces. *Appl. Surf. Sci.* **315**, 516–522 (2014).
112. Vashist, S. K., Lam, E., Hrapovic, S., Male, K. B. & Luong, J. H. T. Immobilization of Antibodies and Enzymes on Platforms for Biosensors and Diagnostics. *Chem. Rev.* **114**, 11083–11130 (2014).
113. Zhang, Y. *et al.* 3-Aminopropyltriethoxysilane functionalized ZnO materials for improving the gas sensitivity to 2-butanone. *Sensors Actuators B Chem.* **363**, 131845 (2022).
114. Bauer, E. M. *et al.* Syntheses of APTMS-Coated ZnO: An Investigation towards Penconazole Detection. *Materials (Basel).* **15**, (2022).
115. Sprick, R. S. *et al.* Polymer photocatalysts with plasma-enhanced activity. *J. Mater. Chem. A* **8**, 7125–7129 (2020).
116. Salinas, R. A. *et al.* Interaction Study of Anti- E. coli Immobilization on 1DZnO at Nanoscale for Optical Biosensing Application. *Adv. Mater. Interfaces* (2023) doi:10.1002/admi.202300167.
117. Xiong, S. *et al.* Solution-phase synthesis and high photocatalytic activity of wurtzite ZnSe ultrathin nanobelts: A general route to ID semiconductor nanostructured materials. *Chem. - A Eur. J.* **13**, 7926–7932 (2007).
118. Ali, H. M., Ibrahim, S. M., Abo Zeid, E. F., Al-Hossainy, A. F. & El-Aal, M. A. A comparative

study of Cu-anchored 0D and 1D ZnO nanostructures for the reduction of organic pollutants in water. *RSC Adv.* **12**, 16496–16509 (2022).

119. Lefatshe, K., Dube, P., Sebuso, D., Madhuku, M. & Muiva, C. Optical dispersion analysis of template assisted 1D-ZnO nanorods for optoelectronic applications. *Ceram. Int.* **47**, 7407–7415 (2021).
120. Parra, M. R. & Haque, F. Z. Poly (Ethylene Glycol) (PEG)-assisted shape-controlled synthesis of one-dimensional ZnO nanorods. *Optik (Stuttg).* **126**, 1562–1566 (2015).
121. Galdámez-Martinez, A., Santana, G., Güell, F., Martínez-Alanis, P. R. & Dutt, A. Photoluminescence of zno nanowires: A review. *Nanomaterials* **10**, 857 (2020).
122. Kegel, J., Povey, I. M. & Pemble, M. E. Zinc oxide for solar water splitting: A brief review of the material's challenges and associated opportunities. *Nano Energy* **54**, 409–428 (2018).
123. Lee, H. B. *et al.* Controlled Defects of Fluorine-incorporated ZnO Nanorods for Photovoltaic Enhancement. *Sci. Rep.* **6**, 1–11 (2016).
124. Wang, J., Chen, R., Xiang, L. & Komarneni, S. Synthesis, properties and applications of ZnO nanomaterials with oxygen vacancies: A review. *Ceram. Int.* **44**, 7357–7377 (2018).
125. Lima, S. A. M., Sigoli, F. A., Jafelicci M., J. & Davolos, M. R. Luminescent properties and lattice defects correlation on zinc oxide. *Int. J. Inorg. Mater.* **3**, 749–754 (2001).
126. Lin, B., Fu, Z. & Jia, Y. Green luminescent center in undoped zinc oxide films deposited on silicon substrates. *Appl. Phys. Lett.* **79**, 943–945 (2001).
127. Van De Walle, C. G. Hydrogen as a cause of doping in zinc oxide. *Phys. Rev. Lett.* **85**, 1012–1015 (2000).
128. Cao, B., Cai, W. & Zeng, H. Temperature-dependent shifts of three emission bands for ZnO nanoneedle arrays. *Appl. Phys. Lett.* **88**, 1–4 (2006).
129. Ahn, C. H., Kim, Y. Y., Kim, D. C., Mohanta, S. K. & Cho, H. K. A comparative analysis of deep level emission in ZnO layers deposited by various methods. *J. Appl. Phys.* **105**, 1–6 (2009).
130. Li, C., Pu, C. & Guo, L. Highly monodispersed ZnO nanorods: preparation and optical properties. *J. Exp. Nanosci.* **10**, 682–689 (2015).
131. Xing, G. *et al.* Charge transfer dynamics in Cu-doped ZnO nanowires. *Appl. Phys. Lett.* **98**, 8–11 (2011).
132. Leung, Y. H., Kwok, W. M., Djurišić, A. B., Phillips, D. L. & Chan, W. K. Time-resolved study of stimulated emission in ZnO tetrapod nanowires. *Nanotechnology* **16**, 579–582 (2005).
133. Hong, S., Joo, T., Park, W., Jun, Y. H. & Yi, G. C. Time-resolved photoluminescence of the size-controlled ZnO nanorods. *Appl. Phys. Lett.* **83**, 4157–4159 (2003).
134. Kodama, K. & Uchino, T. Variations in decay rate of green photoluminescence in ZnO under above- and below-band-gap excitation. *J. Phys. Chem. C* **118**, 23977–23985 (2014).
135. Serrano, A. *et al.* Effect of the seed layer on the growth and orientation of the ZnO nanowires: Consequence on structural and optical properties. *Vacuum* **146**, 509–516 (2017).
136. Galdámez-Martínez, A., Bai, Y., Santana, G., Sprick, R. S. & Dutt, A. Photocatalytic hydrogen production performance of 1-D ZnO nanostructures: Role of structural properties. *Int. J. Hydrogen Energy* **45**, 1–10 (2020).
137. Khan, M. A. & Sakrani, S. Jurnal Teknologi Full paper Synthesis of Cu 2 O and ZnO Nanowires and their Heterojunction Nanowires by Thermal Evaporation : A Short Review. **5**, 83–88 (2014).
138. Ahn, C. H., Kim, Y. Y., Kim, D. C., Mohanta, S. K. & Cho, H. K. Erratum: A comparative analysis of deep level emission in ZnO layers deposited by various methods (Journal of Applied Physics (2009) 105 (013502)). *J. Appl. Phys.* **105**, (2009).
139. Zhang, N., Gao, C. & Xiong, Y. Defect engineering: A versatile tool for tuning the activation of key molecules in photocatalytic reactions. *J. Energy Chem.* **37**, 43–57 (2019).
140. González-Garnica, M. *et al.* One dimensional Au-ZnO hybrid nanostructures based CO2 detection: Growth mechanism and role of the seed layer on sensing performance. *Sensors Actuators B Chem.* **337**, 129765 (2021).

141. Ievtushenko, A. *et al.* Multilayered ZnO films of improved quality deposited by magnetron sputtering. *Acta Phys. Pol. A* **114**, 1131–1137 (2008).
142. Nath, S., Prakash, J., Xiong, J. & Myoung, J.-M. Synthesis of ZnO Nanowire by MOCVD Technique: Effect of Substrate and Growth Parameter. *Nanowires - Recent Adv.* (2012) doi:10.5772/54577.
143. Sburlan, S., Nakano, A. & Dapkus, P. D. Effect of substrate strain on critical dimensions of highly lattice mismatched defect-free nanorods. *J. Appl. Phys.* **111**, (2012).
144. Ye, H. & Yu, Z. Plastic relaxation of mixed dislocation in axial nanowire heterostructures using Peach-Koehler approach. *Phys. Status Solidi - Rapid Res. Lett.* **8**, 445–448 (2014).
145. Cirlin, G. E. *et al.* Critical diameters and temperature domains for MBE growth of III-V nanowires on lattice mismatched substrates. *Phys. Status Solidi - Rapid Res. Lett.* **3**, 112–114 (2009).
146. Glas, F. *Strain in nanowires and nanowire heterostructures*. *Semiconductors and Semimetals* vol. 93 (Elsevier Inc., 2015).
147. Hsu, H. C. *et al.* Orientation-enhanced growth and optical properties of ZnO nanowires grown on porous silicon substrates. *Nanotechnology* **16**, 297–301 (2005).
148. Prabhakar, R. R. *et al.* Efficient multispectral photodetection using Mn doped ZnO nanowires. *J. Mater. Chem.* **22**, 9678–9683 (2012).
149. Ilyas, U. *et al.* High temperature ferromagnetic ordering in c-axis oriented ZnO:Mn nanoparticle thin films by tailoring substrate temperature . *Int. J. Mod. Phys. Conf. Ser.* **32**, 1460341 (2014).
150. Kim, B. H. & Kwon, J. W. Metal Catalyst for Low-Temperature Growth of Controlled Zinc Oxide Nanowires on Arbitrary Substrates. *Sci. Rep.* **4**, (2014).
151. Kang, S. W., Deshmukh, P. R., Sohn, Y. & Shin, W. G. Plasmonic gold sensitization of ZnO nanowires for solar water splitting. *Mater. Today Commun.* **21**, 100675 (2019).
152. Kwoka, M., Kulis-Kapuscinska, A., Zappa, D., Comini, E. & Szuber, J. Novel insight on the local surface properties of ZnO nanowires. *Nanotechnology* **31**, 0–12 (2020).
153. Vallejos, S. *et al.* ZnO Rods with Exposed {100} Facets Grown via a Self-Catalyzed Vapor-Solid Mechanism and Their Photocatalytic and Gas Sensing Properties. *ACS Appl. Mater. Interfaces* **8**, 33335–33342 (2016).
154. Claros, M., Setka, M., Jimenez, Y. P. & Vallejos, S. Aacvd synthesis and characterization of iron and copper oxides modified zno structured films. *Nanomaterials* **10**, 1–16 (2020).
155. Wang, T. *et al.* Photo-directed growth of Au nanowires on ZnO arrays for enhancing photoelectrochemical performances. *J. Mater. Chem. A* **2**, 15553–15559 (2014).
156. Jeong, Y. J., Balamurugan, C. & Lee, D. W. Enhanced CO2 gas-sensing performance of ZnO nanopowder by la loaded during simple hydrothermal method. *Sensors Actuators, B Chem.* **229**, 288–296 (2016).
157. Hunge, Y. M., Yadav, A. A., Kulkarni, S. B. & Mathe, V. L. A multifunctional ZnO thin film based devises for photoelectrocatalytic degradation of terephthalic acid and CO2 gas sensing applications. *Sensors Actuators, B Chem.* **274**, 1–9 (2018).
158. Burghaus, U. Surface chemistry of CO2 - Adsorption of carbon dioxide on clean surfaces at ultrahigh vacuum. *Prog. Surf. Sci.* **89**, 161–217 (2014).
159. Surfaces, O. *Surface and Interface Science*. *Surface and Interface Science* (Wiley, 2013). doi:10.1002/9783527680535.
160. Galdámez-Martínez, A. *et al.* Decay emission study of ZnO nanostructures obtained by low-pressure vapor transport technique. *Appl. Surf. Sci. Adv.* **12**, 100334 (2022).
161. Gómez-Montaño, F. J. *et al.* Determination of Salmonella Typhimurium by Fourier Transform Infrared (FTIR) Spectroscopy Using a Hydrogenated Amorphous Silicon Carbide (a-SiC:H) Thin Film. *Anal. Lett.* **54**, 2655–2665 (2021).
162. Luechinger, M., Prins, R. & Pirngruber, G. D. Functionalization of silica surfaces with mixtures of 3-aminopropyl and methyl groups. *Microporous Mesoporous Mater.* **85**, 111–118 (2005).
163. Krimm, S. & Bandekar, J. Vibrational spectroscopy and conformation of peptides, polypeptides, and proteins. *Adv. Protein Chem.* **38**, 181–364 (1986).
164. Miller, L. M., Bourassa, M. W. & Smith, R. J. FTIR spectroscopic imaging of protein aggregation in living cells. *Biochim. Biophys. Acta - Biomembr.* **1828**, 2339–2346 (2013).